STARS

Electronic Theses and Dissertations, 2004-2019

2012

Surface Measurements And Predictions Of Full-coverage Film Cooling

Gregory Natsui
University of Central Florida

Part of the Aerodynamics and Fluid Mechanics Commons

Find similar works at: https://stars.library.ucf.edu/etd

University of Central Florida Libraries http://library.ucf.edu

STARS Citation

Natsui, Gregory, "Surface Measurements And Predictions Of Full-coverage Film Cooling" (2012). *Electronic Theses and Dissertations, 2004-2019*. 2410.
https://stars.library.ucf.edu/etd/2410

Showcase of Text, Archives, Research & Scholarship

Surface Measurements and Predictions of Full-Coverage Film Cooling

by

Greg Natsui
B.S. Aerospace Engineering, University of Central Florida, 2010

A thesis submitted in partial fulfillment of the requirements
for the degree of Master of Science
in the Department of Mechanical, Materials and Aerospace Engineering
in the College of Engineering and Computer Science
at the University of Central Florida
Orlando, Florida

Fall Term
2012

Major Professor: Jayanta Kapat

ABSTRACT

Full-coverage film cooling is investigated both experimentally and numerically. First, surface measurements local of adiabatic film cooling effectiveness and heat transfer augmentation for four different arrays are described. Reported next is a comparison between two very common turbulence models, *Realizable k-ε* and *SST k-ω*, and their ability to predict local film cooling effectiveness throughout a full-coverage array.

The objective of the experimental study is the quantification of local heat transfer augmentation and adiabatic film cooling effectiveness for four surfaces cooled by large, both in hole count and in non-dimensional spacing, arrays of film cooling holes. The four arrays are of two different hole-to-hole spacings ($P/D = X/D = 14.5, 19.8$) and two different hole inclination angles ($\alpha = 30°, 45°$), with cylindrical holes compounded relative to the flow ($\beta = 45°$) and arranged in a staggered configuration. Arrays of up to 30 rows are tested so that the superposition effect of the coolant film can be studied. In addition, shortened arrays of up to 20 rows of coolant holes are also tested so that the decay of the coolant film following injection can be studied.

Levels of laterally averaged effectiveness reach values as high as $\bar{\eta} = 0.5$, and are not yet at the asymptotic limit even after $20 - 30$ rows of injection for all cases studied. Levels of heat transfer augmentation asymptotically approach values of $h/h_0 \approx 1.35$ rather quickly,

only after 10 rows. It is conjectured that the heat transfer augmentation levels off very quickly due to the boundary layer reaching an equilibrium in which the perturbation from additional film rows has reached a balance with the damping effect resulting from viscosity. The levels of laterally averaged adiabatic film cooling effectiveness far exceeding $\bar{\eta} = 0.5$ are much higher than expected. The heat transfer augmentation levels off quickly as opposed to the film effectiveness which continues to rise (although asymptotically) at large row numbers. This ensures that an increased row count represents coolant well spent.

The numerical predictions are carried out in order to test the ability of the two most common turbulence models to properly predict full coverage film cooling. The two models chosen, $Realizable\ k - \varepsilon\ (RKE)$ and $Shear\ Stress\ Transport\ k - \omega\ (SSTKW)$, are both two-equation models coupled with Reynolds Averaged governing equations which make several gross physical assumptions and require several empirical values. Hence, the models are not expected to provide perfect results. However, very good average values are seen to be obtained through these simple models. Using RKE in order to model full-coverage film cooling will yield results with 30% less error than selecting $SSTKW$.

For Emily, the love of my life.

ACKNOWLEDGMENTS

Professor Jayanta Kapat, thank you for providing an environment that allows us to grow as people and as engineers.

Thanks to my committee; Dr. Seetha Raghavan and Dr. Subith Vasu.

An especially big thank you belongs to Dr. Michael Crawford. I have grown significantly as an engineer as a result of your knowledge and attention to detail. Also from Siemens, thank you Ken Landis, Glenn Brown and Reinhard Schilp for working with me all these years.

Finally, thanks to every person, past, present, and future, from the amazing CATER lab. Roberto, Allred, Torrance, Constantine Wolski III, Justin, Jahed, Matt, Josh, Mark, Lucky, Brian, Michelle, Tony, Perry, Sergio, Barkin, Sri, Harrington, Vaidy, Quan, Jared, Jason, Miller and Orlando!

TABLE OF CONTENTS

LIST OF FIGURES

xv

LIST OF TABLES

CHAPTER 1
SUCK, SQUEEZE, BANG, BLOW AND CONSEQUENCES THEREOF

Modern gas turbines represent the most state of the art commercial technology to date in the history of human engineering. The designs of the advanced turbines being produced utilize the most advanced research from structural, materials, probabilistic design, combustion, aerodynamics, heat transfer, sheer organizational schemes, manufacturing, environmental engineering, chemistry, sensor, experimental and computational disciplines. The design of a turbine is truly multi-faceted and challenging. Gas turbines (GT) operate on the Brayton Cycle which is characterized by four ideal steps:

The Ideal Brayton Cycle

- $1 - 2$: Isentropic Compression

- $2 - 3$: Isobaric Heat Addition

- $3 - 4$: Isentropic Expansion

- $4 - 1$: Isobaric Heat Extraction

These processes are plotted on $P-v$ and $T-s$ diagrams in Figure 1.1. The first patent incorporating the Brayton Cycle was a reciprocating style closed loop engine, patented by

John Barber in 1791. The intent was for this engine to power a "horseless carriage", however, due to limitations in technology at that time the engine was unable to produce successful work. A picture of his invention from his patent can be seen in Figure 1.2.
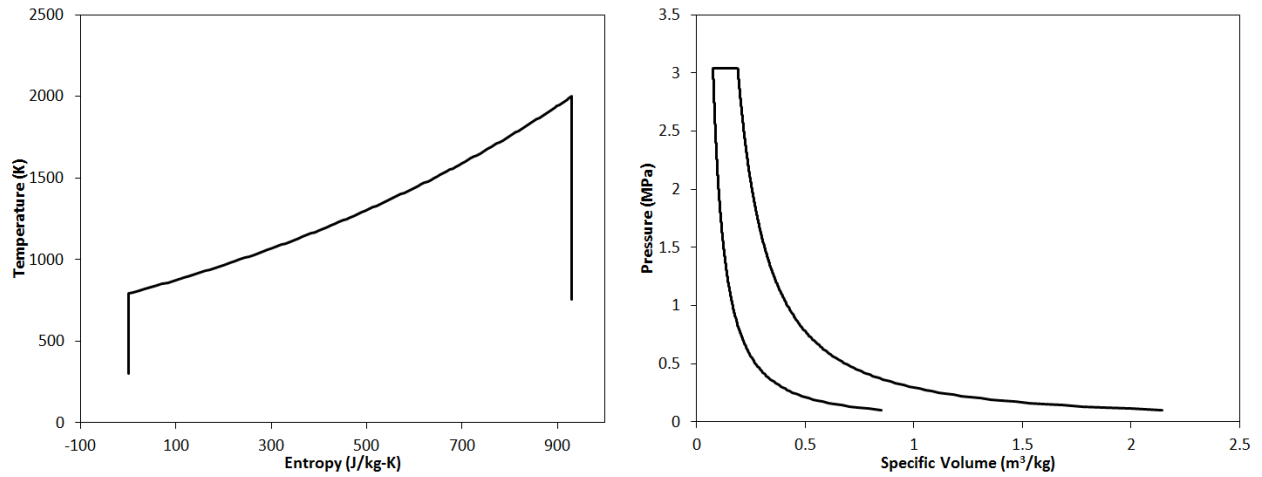
Figure 1.1: $P - v$ and $T - S$ diagrams of the Ideal Brayton Cycle.
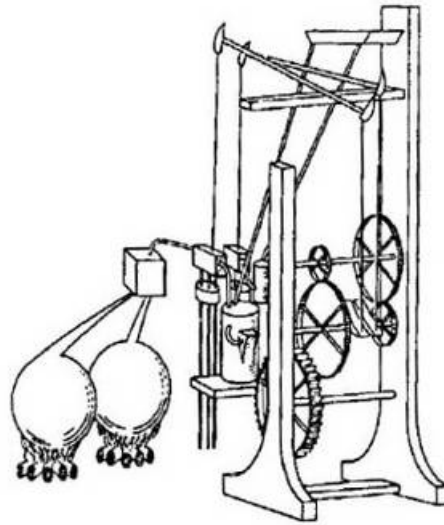
Figure 1.2: The picture of John Barber's original heat engine operating on the Brayton Cycle.

In a reciprocating engine, the different thermodynamic processes composing the cycle all take place in the same location but at different times. Today, GT engines operate continuously and these different processes take place in different regions of the engine, all at the same time.

1.1   Motivation to Study The Cycle

The Energy Crisis; Global warming, power bills and airplane tickets. Trillions of dollars are spent on these three items worldwide. Global warming is a result of increased levels of carbon in the atmosphere, a byproduct of combustion. Power bills are expensive. Airline tickets are expensive. If we possessed a completely free, completely renewable, infinite source of energy, the world would be a much simpler place. But we do not, hence, there is a large demand to increase the efficiency, decrease the cost, and eliminate the environmental impact of power generation.

The EIA reports a projection of energy production showing the contribution from many types of energy sources. Something to note is that even though our reliance on renewable energy is continually growing, our use of coal and natural gas still needs to increase to meet world demands, [1]. Furthermore when looking at the resources shown, liquids, hydroelectricity, nuclear, natural gas and coal, one must appreciate the fact that turbines are the predominant method for extracting power from these energy sources. In fact, turbines produce 98% of the power used in the world and Gas Turbines (GTs) are responsible for

100% of all commercial aviation propulsion. These two statements alone make a very strong case for our continued interest in advancing turbine technology as turbines will be just as integral to everyday life in the foreseeable future as they are today.

$$\eta_{Brayton} = 1 - \frac{T_1}{T_3} = 1 - \left(\frac{P_1}{P_3}\right)^{\frac{\gamma-1}{\gamma}} \tag{1.1}$$

After studying Equation 1.1, it can be seen that the thermal efficiency of the Brayton cycle increases as the firing temperature increases. This is the ultimate motivation for raising current firing temperatures which already cause heat fluxes on the order of $2MW/m^2$ and temperatures exceeding $1900K$ in the first stage of gas turbines, Polezhaev [2]. With temperatures far past the allowable metal temperature of engine components, GTs survive by advanced materials and coating along with several different advanced cooling schemes working in tandem to prevent engine failure. However, cooling does come at a cost. Coolant is extracted from mid to late stages in the compressor, meaning work is used to compress the coolant which would otherwise represent power generated.

The use of 20 to 30% of this compressed air to cool the high-pressure turbine presents a severe penalty on the thermodynamic efficiency unless the firing temperature is sufficiently high for the gains to outweigh the losses. — R. S. Bunker [3]

Modern cooling technologies require complete understanding in order to design a component with a high level of confidence which is cooled better and with less flow then previous generations.

1.2   Gas Turbine Heat Transfer

In the 1950s turbines were uncooled implying that the hot gas path was maintained at a level in which the components can survive. The desire to increase turbine efficiency forced engineers to find ways to increase the hot gas temperature. This was accomplished by passing compressor air through the blades, which is appreciably cooler then the hot gas path, effectively lowering the metal temperatures, this scheme is known as convection cooling. This technology advanced from simply passing cold air though the blade to utilizing serpentine internal passages, turbulators, and impingement-cooling. This was good yet left much to be desired and film-cooling was introduced. Film cooling allowed for a quantum leap in hot gas path temperatures as it very effectively cuts the source temperature to the blade by several hundreds of Kelvin. Modern turbines utilize a combination of film, impingement and sophisticated internal cooling schemes to realize temperatures of the working fluid exceedingly hotter than the allowable metal temperature of the components.

1.3   Film Cooling

Film cooling is the introduction of a secondary fluid (coolant or injected fluid) at one or more discrete locations along a surface exposed to a high temperature environment to protect that surface not only in the immediate region of injection but also in the downstream region." — R. J. Goldstein [4]

Due to the large rewards and even greater complexity related to film cooling, there has been a startling amount of research over several decades in the area focusing on every imaginable aspect of the technology. Studies have been conducted on the effects on cooling due to turbulence intensity of the main-flow, hole roughness, hole blockage, hole manufacturing technique, freestream boundary layer thickness, density ratio between the two stream, momentum flux ratio, mass flux ratio, hole inclination angle, hole compound angle, hole length, hole spacing, hole inlet conditions, adverse and favorable pressure gradients, downstream of a rotating wake, hole exit shaping, hole embedded in trenches, film jet Mach number, several Reynolds numbers based on different scales, the list goes on and on. There are literally thousands of academic and industry studies in the single area of film cooling hence not every paper can be summarized below and focus will be placed only upon studies of immediate importance to the present work.

1.3.1 Heat Transfer of a Film Cooled Boundary Layer

In general, a heat flux can be calculated from Newton's Law of Cooling, Equation 1.2,

$$q" = h(T_{hot} - T_{cold}) \tag{1.2}$$

Because h is a function of the coolant temperature T_c, it is necessary to define a datum temperature. In the hypothetical situation in which the wall is adiabatic, i.e. $q_{film}" = 0$, the wall would reach a certain temperature distribution. Let us define this temperature as T_{aw}, the adiabatic wall temperature. The heat flux into the wall can now be defined as

$$q_f" = h_f(T_w - T_{aw}) \tag{1.3}$$

This new temperature T_{aw} is still dependent upon the injection temperature of the coolant. In order to circumvent this dependency let us define yet another new parameter, adiabatic film cooling effectiveness, η;

$$\eta \equiv \frac{T_\infty - T_{aw}}{T_\infty - T_c} \neq f(T_\infty, T_c) \tag{1.4}$$

This new parameter η successfully removes the dependence of injection temperatures and is now only a function of the parameters influencing film cooling performance. Now, the film temperature, or adiabatic wall temperature T_{aw}, can be obtained from the definition for film cooling effectiveness, η. η, is zero when $T_{aw} = T_\infty$ and equal to unity when $T_{aw} = T_c$.

The same issue for T_{aw} arises when considering h_f, in that it is a function of some very specific parameters, specifically T_c and T_{aw}. In order to remove this dependency an

7

augmentation factor, h/h_0, is defined as;

$$\frac{h}{h_0} \equiv \frac{h_f}{h_0} \qquad (1.5)$$

where h_0 is the heat transfer coefficient in the absence of a coolant film.

Heat transfer augmentation, h/h_0, is the factor indicating the added mixing that film cooling promotes near the wall. Typically the augmentation is greater than unity, however, has been known to drop below unity in the recovery region. More times than not, however, the effect of injection is to increase the heat transfer conductance of the boundary layer.

All parameters have now been defined in order to investigate the main parameter of interest, the net heat flux reduction $(\Delta q")$, which is a measure of how much the film has reduced heat transfer into the wall. Equation 1.6 defines $\Delta q"$ as,

$$\Delta q" \equiv 1 - \frac{q_f"}{q_0"} \qquad (1.6)$$

which reduces to

$$\Delta q" = 1 - \frac{h}{h_0}\left(1 - \frac{\eta}{\phi}\right) \qquad where \qquad \phi = \frac{T_\infty - T_w}{T_\infty - T_c} \qquad (1.7)$$

Upon examination of Equation 1.7 it can be shown that it is of interest to minimize the heat transfer augmentation h/h_0 and to maximize film cooling effectiveness η. The parameter ϕ represents a goal dictated by design requirements, but is dependent upon the cooling performance.

In practice it is not straight forward to measure the heat transfer coefficient in the presence of film defined by rearranging Equation 1.3. It is easier to compute Equation 1.2

and convert to the desired heat transfer coefficient. This relation can be derived by equating Equations 1.2 and 1.3 then solving for $q_f^{"}$. The result is shown as Equation 1.8,

$$h_f = h_u \left(1 - \eta\theta\right)^{-1} \tag{1.8}$$

in which the uncorrected heat transfer coefficient h_u is the h from Equation 1.2 because it has yet to be "corrected" properly for film temperature.

1.3.2 Control Volume Analysis of a Film Cooled Boundary Layer

In order to gain some insight into the physics of a film cooled boundary layer, a very simplistic analysis is repeated here from Goldstein [4].

Assumption 1 Constant property ideal gases

Assumption 2 Flow over the wall is adiabatic

Assumption 3 $\bar{T}$ is equal to the adiabatic wall temperature T_{aw}

Assumption 4 A 1/7th power turbulent profile

Assumption 5 The boundary layer thickness grows as a typical turbulent profile over a flat plate with no injection

Assumption 6 Hydrodynamic boundary layer starts at the point of injection $(x' = x)$, noting at the injection location $x = 0$

Assumption 7 $C_{p_\infty} = C_{p_c}$

First, a mass and energy balance on the control volumes from Figure **??** is performed. From continuity,

$$\dot{m} = \dot{m}_c + \dot{m}_\infty = \int_0^\delta \rho u \, dy \tag{1.9}$$

Equation 1.9 will be used in conjunction with an assumed velocity profile once the energy equation is reduced. Let us define the average temperature in the boundary layer, $\bar{T}$, as,

$$\bar{T} - T_\infty = \frac{\int_0^\delta \rho u C_p (T - T_\infty) \, dy}{\int_0^\delta \rho u C_p \, dy} \tag{1.10}$$

Following Assumption 1, the average specific heat at constant pressure is then,

$$\bar{C}_p = \frac{\dot{m}_c C_{p_2} + \dot{m}_\infty C_{p_\infty}}{\dot{m}_c + \dot{m}_\infty} \tag{1.11}$$

Following Assumption 2, the energy balance can be written as,

$$\left(\dot{m}_c + \dot{m}_\infty \right) \bar{C}_p \bar{T} = \dot{m}_c C_{p_2} T_c + \dot{m}_\infty C_{p_\infty} T_\infty \tag{1.12}$$

After a significant amount of algebra, and using Assumption 3, this can be written in the form,

$$\frac{T_{aw} - T_\infty}{T_c - T_\infty} = \eta = \frac{1}{1 + \dfrac{\dot{m}_\infty C_{p_\infty}}{\dot{m}_c C_{p_2}}} \tag{1.13}$$

Now continuity, Equation 1.9 is used to determine $\dot{m}_\infty / \dot{m}_c$. Assumption 4 implies,

$$\frac{u}{U_\infty} = \left(\frac{y}{\delta} \right)^{1/7} \tag{1.14}$$

10

From Equations 1.9 and 1.14,

$$\dot{m}_\infty = \int_0^\delta \rho_\infty U_\infty \left(\frac{y}{\delta}\right)^{1/7} dy = \frac{7}{8}\rho_\infty U_\infty \delta \tag{1.15}$$

Assumption 5 implies,

$$\frac{\delta}{x'} \approx 0.376 Re_{x'}^{-1/5} \tag{1.16}$$

Combining Equations 1.15 and 1.16 and incorporating Assumption 6 leads to the following

expression for $\dot{m}_\infty$,

$$\dot{m}_\infty = 0.329 \rho_\infty U_\infty x Re_x^{-1/5} \tag{1.17}$$

Dividing by $\dot{m}_c = \rho_c u_c s$, where s is the length of the slot in the streamwise direction, yields

an expression for $\dot{m}_\infty / \dot{m}_c$,

$$\frac{\dot{m}_\infty}{\dot{m}_c} = \frac{0.329 \rho_\infty U_\infty x \left(\frac{U_\infty x \rho_\infty}{\mu_\infty}\right)^{-1/5}}{\rho_c u_c s} \tag{1.18}$$

This expression leads to the notion that the ratio between coolant mass flux and mainstream

mass flux is an important parameter. Defining the mass flux ratio, or blowing ratio, M as,

$$M \equiv \frac{\rho_c u_c}{\rho_\infty u_\infty} \tag{1.19}$$

and re-arranging, Equation 1.18 can be written as

$$\frac{\dot{m}_\infty}{\dot{m}_c} = 0.329 \left(\frac{x}{Ms}\right)^{4/5} \left[Re_c \left(\frac{\mu_c}{\mu_\infty}\right)\right]^{-1/5} \tag{1.20}$$

In order to simplify this equation, let us define the parameter ξ as,

$$\xi = \left(\frac{x}{Ms}\right) \left[Re_c \left(\frac{\mu_c}{\mu_\infty}\right)\right]^{-1/4} \tag{1.21}$$

Finally, using Assumption 7, Equation 1.13 can be written as,

$$\eta = \frac{1}{1 + 0.329\xi^{4/5}} \tag{1.22}$$

1.3.3   Film Cooling Parameters

1.3.3.1   Geometric Independent Parameters

Hole Diameter, D – The length-scale used for film cooling studies is generally the hole diameter, D.

Hole Length, L – measured from inlet breakout to exit breakout. The length of the hole, L, is typically fixed by the application, however, the hole length does have a significant impact on the dynamics of the exiting film jet. The non-dimensional hole length is L/D. A short hole ($L/D < 4$) will not allow the flow to develop from the vena-contracta generated as the flow enters the hole, this will increase the ability of the coolant flow to jet into the mainstream because of a locally high momentum flux. A long hole ($L/D > 6$) allows the entrance effects to diminish as well as more time for the wall to affect the velocity profile; the net effect is to reduce the jets ability to penetrate into the main flow.

Inclination Angle (Surface Angle), α – measured from surface to hole axis, in the plane of the hole axis. α is typically between $10-90°$ for film cooling applications. The effect

of α is to adjust the wall normal component of momentum of the coolant jet as it leaves the wall.

Compound Angle (Flow Angle), $\boldsymbol{\beta}$ – measured from axis projected onto wall relative to flow. β can vary anywhere between $\pm 90°$. Any deviation from 0 will cause an asymmetric vortex pair exiting the film hole. This is beneficial because it disrupts the induced wall normal velocity, and instead promotes spreading of the jet. Once $\beta = 90°$, the film jet is characterized by a single dominant vortex, with z-vorticity opposite the sign of β.

Lateral Pitch, $\boldsymbol{P}$ – the lateral distance between two adjacent holes, measured from hole exit breakout to adjacent hole exit breakout. The pitch is non-dimensionalized by the hole diameter to create a non-dimensional spacing, P/D.

Streamwise Pitch, $\boldsymbol{X}$ – the streamwise distance between two adjacent rows and is normalized to X/D. Both P/D and X/D impact the amount of interaction between the neighboring jets and overall affect the solidity of the film array.

These parameters are sketched in Figures 1.3 and 1.4.
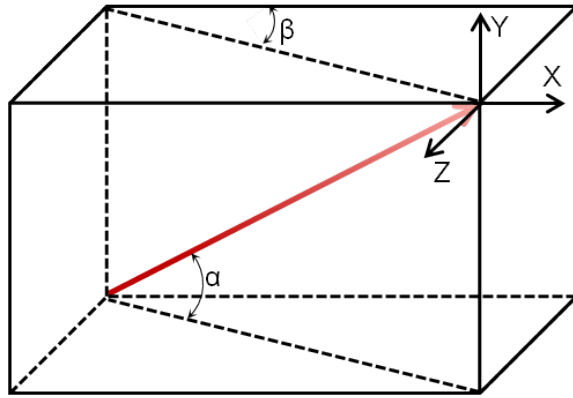
Figure 1.3: Diagram defining orientation angles α and β.
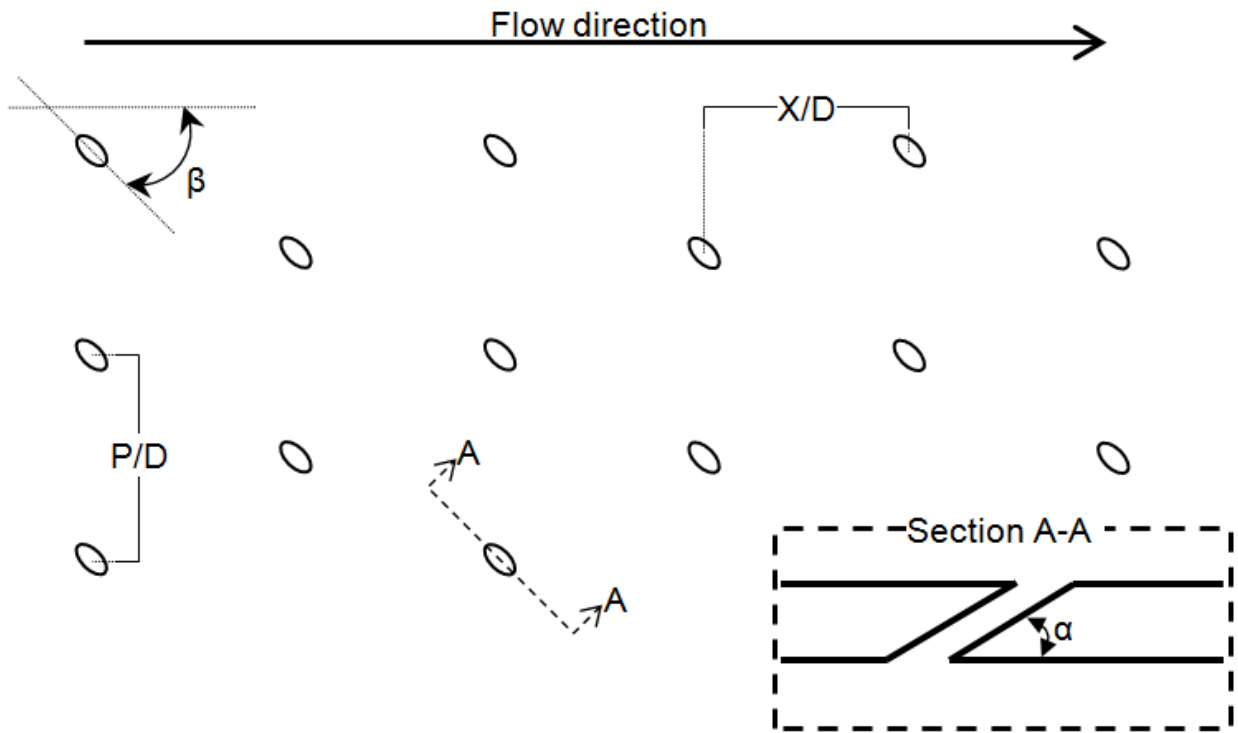
Figure 1.4: Diagram of geometric parameters.

1.3.3.2 Fluid Mechanics Independent Parameters

Other than the film source geometry, the fluid mechanic parameters of the flow are also hugely influential to the performance. Shown in Equation 1.23, the blowing ratio (M) describes the ratio of coolant mass flux to mainstream hot gas mass flux. This ratio indicates the amount of mass injected into the boundary layer. The mainstream and coolant density (ρ), average coolant velocity magnitude (U_c) and freestream velocity (U_∞) are used.

$$M = \frac{(\rho U)_c}{(\rho U)_\infty} \tag{1.23}$$

Other parameters often used to describe film cooling performance are the density ratio (DR) and the momentum flux ratio (I). These are calculated using Equation 1.24 and Equation 1.25 respectively. The density ratios effect is to influence the momentum flux ratio for a given blowing ratio. That is, once a blowing ratio is fixed, the momentum ratio is determined based on the density ratio. A density ratio less than unity is commonly used in laboratory testing, however, the density ratio of an engine is much greater than unity. A value of $DR < 1$ will raise the momentum flux ratio.

$$DR = \frac{\rho_c}{\rho_\infty} = \frac{T_\infty}{T_c} \tag{1.24}$$

$$I = \frac{(\rho U^2)_c}{(\rho U^2)_\infty} = \frac{M^2}{DR} \tag{1.25}$$

The influence of momentum flux ratio on the dynamics of the jet is shown in Figure 1.5. The limits are vague due to several other factors impacting the behavior, hence, only a qualitative explanation is possible without being more specific elsewhere.
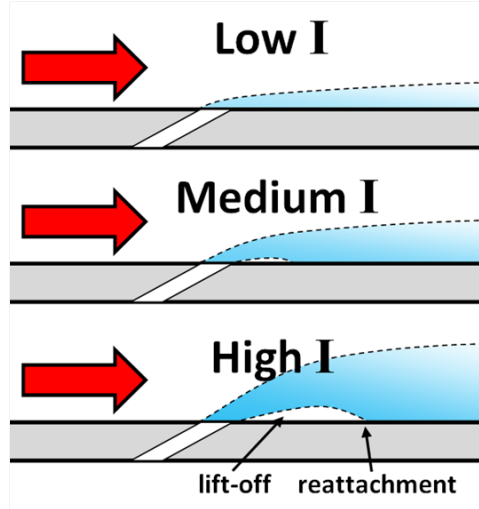
Figure 1.5: Effect of momentum flux ratio I.

These three momentum flux ratio regimes have been described previously, quoted from Goldstein [4]:

- *Mass addition regime* — Effectiveness increases with M due to increased thermal capacity of the coolant, but the effectiveness is independent of the density ratio and velocity ratio parameters.

- *Mixing regime* — Effectiveness distribution depends on M, DR due to opposing influence of increased thermal capacity and increased coolant/free-stream mixing and penetration.

- *Penetration Regime* — Effectiveness distribution is completely dominated by a complex interaction of excessive coolant penetration and augmented turbulent diffusivity and turbulent diffusion of the coolants thermal effect toward the surface.

Other important flow parameters include;

Velocity Ratio VR – Simply a rearrangement of M, DR and I. VR is a more common
parameter in fluid mechanics studies of a jet-in-crossflow in which the two streams are
typically the same temperature. Once two of these four parameters are specified, the
remaining two are fixed.

Reynolds Number Based on Hole Diameter and Freestream Velocity, $Re_{D,\infty}$ - A
Reynolds number which is similar to a cylinder in crossflow. Simply a convenient defi-
nition which gives some insight into the significance of the film jet interacting with the
mainflow.

Momentum Thickness to Hole Diameter Ratio δ_2/D – A measure of the relative thick-
ness of the incoming boundary layer. Typically a low value of this parameter, < 0.2 is
representative of engine conditions.

1.3.3.3 Dependent Parameters of Film Cooling

The main parameter of interest is the net heat flux reduction, $\Delta q^{"}$. The reduction
in heat flux is affected by each parameter described above as well as some parameters not
mentioned, e.g.,

$$\Delta q^{"} = f(x, z, D, L, \alpha, \beta, P, X, M, I, Re_{D,\infty}, \delta_2/D,$$

$$Surface\ Roughness, Hole\ Geometry, Surface\ Curvature,$$

$$Freestream\ Turbulence, Pressure\ Gradient, ...) \quad (1.26)$$

1.3.4 Slot Cooling

The most fundamental approach to film cooling is that of a film introduced through a 2-D slot.

1.3.4.1 Goldstein, Shavit and Chen (1965)

Goldstein et al. [5] study the coolant film generated by a strip of porous material embedded in a wall. The group experimentally investigates the effects of varying coolant temperature, blowing ratio and freestream velocity. The temperature and velocity boundary layers due to the presence of film are measured and indicate that normal injection through a porous strip is akin to tangential injection through a slot. This is also confirmed in the similarity between downstream effectiveness and the authors further go on to show that for the same the mass injection per unit width of the strip (Mh), the two geometries provide the same coverage. The adiabatic film-cooling effectiveness downstream of the injection point

can be correlated against (X/Mh), very similar to other film cooling correlations. It was also shown that existing correlations for slot cooling can be readily applied to strip transpiration scenarios.

1.3.4.2   Hartnett, Birkebak and Eckert (1961)

Hartnett et al. [6] fully characterize the external aerodynamics and heat transfer downstream of a tangential slot for one slot geometry and one blowing ratio. While this study does not address trends that designers would be interested in, it does lay the groundwork for a comprehensive understanding of the given film scenario. It is noted that for some cases of slot injection there is no heat transfer augmentation due to the presence of film; however, this is not the case for all films.

1.3.5   Discrete Film Cooling

In practice a film cannot readily be introduced through a slot due to the significant impact on part strength resulting from removing material. Hence, succesful designs incorporate discrete holes through which the coolant is introduced to the boundary layer.

1.3.5.1 Pedersen et al. (1977)

Pedersen et al. [7] experimentally investigate the effects of density ratio in film cooling. The injection sources investigated are a porous strip and and inclines holes with $\alpha = 35°$ and $P/D = 3$. Several different secondary gases are used (such as CO_2 and He)to yield density ratios ranging from 0.75-4.17. Measurements are taken by drawing a small amount of gas from the near-wall region into a device which measures concentration. From the results presented it can be seen that the density ratio augments the momentum flux ratio for a given blowing ratio, thereby influencing the dynamics of the jet

1.3.5.2 Sinha et al. (1991)

Sinha et al. [8] study an inclined row of holes ($\alpha = 25°$, $P/D = 3$, $L/D = 1.75$) to investigate the effect of density ratio in film cooling. Cryogenically cooled air allows the density ratio to vary from 1.2-2.0. The test surface is constructed out of expanded polystyrene foam with a thermal conductivity of $0.027 W/m-K$. This ribbon thermocouples are used to obtain temperatures which results in negligible thermocouple conduction error. It is concluded that film cooling performance cannot be predicted with either M or I alone. There are distinct ranges over which each parameter is of leading importance.

1.3.5.3 Aga (2009)

Particle image velocimetry data was provided for a single row of film cooling holes spaced four diameters apart with α and β being 20° and 45° respectively by Aga [9]. Blowing ratio, density ratio and, therefore, momentum flux ratios were varied. The results show a skewed vortex structure of the film jet as compared to the CVP found in its $\beta = 0°$ counterpart. Important to notice is that no liftoff off the coolant jet is seen even at the highest blowing ratio ($M = 3.0, I = 9.0$). The jet entrains the boundary layer on the upstream side, while thinning it on the downstream side, leading to higher heat transfer coefficients which then decrease the overall effectiveness of the coolant. Other subtle variations in the jet are seen with changing density ratio and momentum flux ratio.

1.3.5.4 Goldstein, Eckert, Eriksen and Ramsey (1969)

In a fundamental study on discrete hole film cooling by Goldstein et al. [10] the film cooling effectiveness downstream of single holes and rows of holes is obtained experimentally. The main focus is to study the effect of inclination and compound angles for single holes and rows of holes. The authors take the temperature data from a single hole and tried to superpose the temperature distribution to replicate that which one would expect from a row of holes. This approach is most applicable to a row in which the adjacent holes do not interact with one another. For low blowing ratio cases this method is very good for centerline

values however in the area between holes this superposition approach tends to over-predict. This is most likely due to the interaction of the jets enhancing mixing and thereby lowering cooling effectiveness. However, the authors do manage to show that by superposing data from a single hole, one can get an idea of the effectiveness they would expect from a row of similar holes.

1.3.5.5   Baldauf et al. (2002)

Baldauf et al. [11] use IR thermography to investigate a single row of film cooling holes. The holes are inclined and spaced at differing values. The effect of density ratio, inclination angle, hole spacing, and mainstream turbulence are investigated. A comparison to values obtained in literature is made; the current study matches very well with the values in literature. A correlation is made using the current data and data available in open literature. Two different flow patterns are seen in the laterally averaged downstream effectiveness. A single jet in crossflow mixing and adjacent jet interaction are recognized to affect downstream effectiveness with differing attenuations. Single jet mixing has a greater effect at short downstream distances at lower blowing ratios. Additionally single jet in crossflow mixing can govern whether the jet lifts off. At higher blowing ratios and further downstream, jet spreading allows for adjacent jet interaction to occur. The included correlation predicts downstream film cooling effectiveness in the presence of film cooling from a single, inclined row of holes.

1.3.5.6 Baldauf et al. (2002)

A companion paper to Baldauf et al. [11], Baldauf et al. [12] detail a correlation for heat transfer augmentation. This correlation is applicable to the entire downstream surface and various ejection parameters. This correlation can be combined with the effectiveness correlation presented in the companion paper to analyze wall temperatures. A net heat flux reduction model is given which does not depend on an arbitrarily chosen wall surface temperature. The actual heat flux reduction is found by combining heat transfer coefficients and adiabatic wall effectiveness values from the same flow conditions. Moderate blowing ratios and ejection angle show the best potential cooling. An optimal velocity ratio is found to be approximately 0.5 for the moderate hole spacing. Very high blowing rates are studied and shown to be useful only in certain circumstances, where a steep blowing angle and wide pitch are required.

1.4 Full-Coverage Film Cooling

In this study we will define full-coverage film cooling as sequential rows of film cooling holes installed on the same component, for the purpose of generating a film which builds upon previous rows coolant. This can be seen schematically in Figure 1.6.
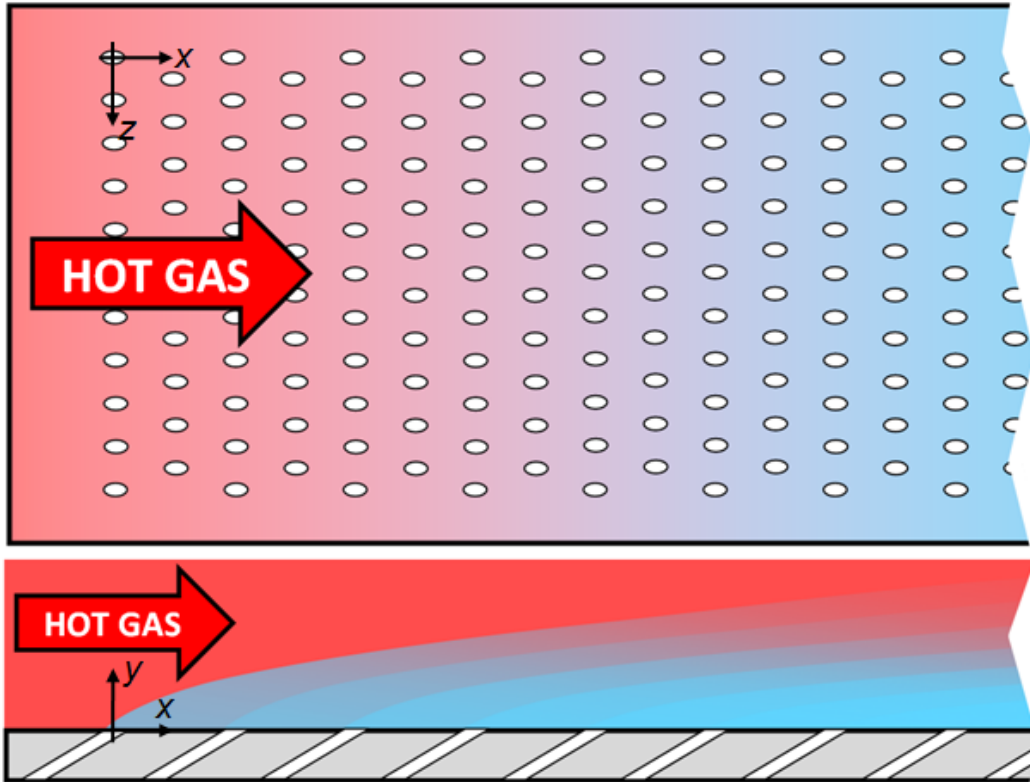
Figure 1.6: Diagram of full-coverage film cooling.

There is an extensive amount of literature on film cooling, yet there is a much less complete look at the field of full-coverage film cooling. Generally full-coverage film cooling is characterized by increasing values of effectiveness and a heat transfer augmentation factor which levels off in the streamwise direction. An airfoil with a full-coverage film cooling arrangement on the pressure side is shown in Figure 1.7.
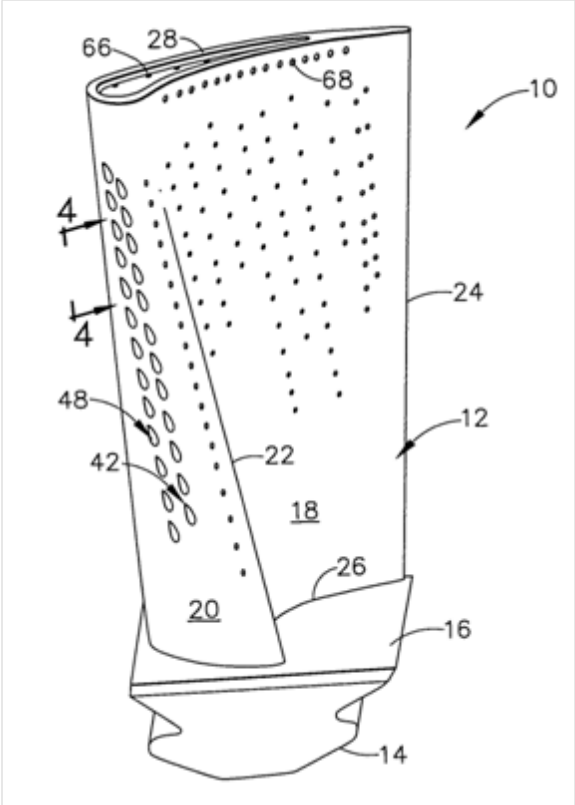
Figure 1.7: Figure from a patent which incorporates full-coverage film cooling on the surface of an airfoil.

Table 1.1: Full-Coverage Film Cooling Literature

Year	Data	Rows	α	β	P/D	X/D	Citation
1960	η	4	90°	-	?		Papell [13]
1973	η, h	10	90°	-	4.8	4.8	Metzger [14]
1975	η, h	15	30°	45°	8, 10, 14	6.9, 8.7, 12.1	Mayle [15]
1976	η, h	4	90°	-	4.8	4.8	Metzger [16]
1979	h	?	90°	-	8	8	Le Grives [17]
1979	η	?	45°	0°	3	5, 10	Sasaki [18]
1980	Flow	11	30°	0°	5	5	Yavuzkurt [19]
1980	Modeling	11	30°	0°	5	5	Yavuzkurt [20]
1980	h	6, 11	90°, 30°	0°, 45°	5	5, 10	Crawford [21]
1980	Modeling	6, 11	90°, 30°	0°, 45°	5	5, 10	Crawford [22]
1981	η, h	?	30°	0°	5, 10	5, 10	Kasagi [23]
1995	η, h	7	90°	-	3	3	Cho [24]
1995	η, Flow	7	17°	0°	4.48	7.46	Martiny [25]
2001	η	10	90°	-	7.14	7.14	Harrington [27]
2002	η, h	12, 18	20°	0°	10, 16	10, 16	Ling [28]
2003	h	10	90°	-	7.14	7.14	Kelly [29]
2009	Flow	9	30°	0°	?		Michel [30]

1.4.1 Literature

1.4.1.1 Mayle and Camarata (1975)

Mayle and Camarata [15] investigate the effect of hole pitch-to-diameter ratio and blowing ratio by determining adiabatic effectiveness and heat transfer augmentation. The arrays studied are composed of holes inclined at $\alpha = 30°$ and compounded at $\beta = 45°$. The focus of the study is to provide more information on the influence of hole and row spacing on film cooling array performance. Tests are run at a film-cooling Reynolds number of $Re_{D,\infty} = 3600$. Measurements are taken in a span-averaged manner. Heat transfer testing is conducted at steady state with instrumented copper blocks. The adiabatic film-cooling effectiveness measurements are taken on the adiabatic wall with a radiometer and traversing system. Discrete measurements are taken and averaged for each row of holes. The reported uncertainty in heat transfer coefficient is 8%.

A superposition technique is adopted from a previous report by Goldstein et al. [10] which uses effectiveness data following a single row to predict the downstream development of an array of film holes. The superposition technique is based off a point sink model, superimposed to predict the effect of more than a single jet/row. It is consistently noted, both by Mayle and Camarata [15] as well as Goldstein et al. [10], that this technique's main drawback is in areas where there is a large amount of interaction between coolant jets.

Mayle concludes that the integrity of each individual jet can be seen in the adiabatic film-cooling effectiveness. This is universally agreed upon in the current understanding of film literature. The interaction and coalescence of individual jets is found to have a detrimental impact upon downstream film-cooling effectiveness. Average heat transfer augmentations up to $h/h_0 = 2.5$ are measured, showing that heat transfer augmentation must be considered while designing a film-cooling array.

1.4.1.2   Sellers (1963)

Sellers [31] originates a superposition method that is used in many future works. Described is a method of linearly superimposing cooling features in order to predict effectiveness downstream of a single set of features. The goal is to predict how additional rows of film holes add to the effectiveness obtained experimentally from a single row. Data is presented from outside sources with an added correlation that fits well.

1.4.1.3   Metzger et al. (1973)

Metzger et al. [14] present effectiveness and heat transfer data for a full-coverage film cooling array with $P/D = X/D = 4.8$. The holes are normal, $\alpha = 90°$, with inline and staggered arrays. A calorimeter spanning multiple rows is used to measure heat transfer coefficients. Effectiveness values are calculated using the measured heat transfer coefficients,

resulting in a 25% uncertainty. A method of single row superposition from Goldstein [10] is used to compare results. This superposition method does not take into account jet interaction from downstream rows. Downstream contribution of each row is terminated at either 10 or 20 diameters, with 10 better fitting experimental data. Periodically fully developed film is established by the fourth row for the staggered array and the second row for the inline array. Blowing ratios have to be assumed from the given velocity ratios by using a density ratio of one; the resulting blowing ratios are 0.1 and 0.2. Measured heat transfer coefficients are $20 - 25\%$ higher than no coolant conditions. The resulting staggered array results show greater effectiveness values than the inline arrays as a result of reduced jet interaction.

1.4.1.4 Metzger et al. (1976)

Metzger et al. [16] use the same experimental setup used from the previous paper, Metzger et al. [14], to extend the blowing ratio range tested, $M = 0.1, 0.2, 0.3$ and 0.5. Superposition of single hole, normal injection data provides a reasonable fit for blowing ratios of 0.1 and 0.2 while greatly over-predicting at the higher blowing ratios. The results show that for this four row array, the optimal blowing ratio is between 0.2 and 0.3.

1.4.1.5 Crawford, Kays, and Moffat (1976, 1980)

Crawford et al. [21][22][32] experimentally obtains Stanton numbers for several full-coverage arrays composed of various hole orientations and spacings. Heat transfer experiments are run with $\alpha = 90°/\beta = 0°, \alpha = 30°/\beta = 0°$, and $\alpha = 30°/\beta = 45°$. Zero degree inclination angle produces the greatest heat transfer augmentation. Increasing the number of rows increases the downstream recovery region affected area. A compound angled, inclined hole at a mass flux ratio of 0.4 to 0.5 provides the lowest heat transfer augmentation. The highest increase in heat transfer augmentation is seen by normal injection of coolant. An increase in heat transfer augmentation for all geometries is seen at mass flux ratios greater than 0.4. Increasing the number of downstream rows keeps an elevated heat transfer coefficient while increasing the area being protected.

1.4.1.6 Sasaki et al. (1979)

Sasaki et al. [18] uses an IR camera to study compound angle holes, $\beta = 45°$, with a small lateral spacing, $P/D = 3$, and compares to a point source model. A superposition method proposed first by Sellers [31] is used to compare to the experimental data. Superposition predicts the low blowing ratio cases well for all seven streamwise rows ($X/D = 5$). Single row testing compares favorably with the point source model. The superposition method becomes less accurate at blowing rates greater than 0.15. The number of accurate

row predictions decreases from 7 to 3 as the blowing ratio increases, especially for the cases

with larger spaces between rows. Row spacing and blowing ratio affect the superposition

method's accuracy in an inverse manner, i.e., increasing row spacing and blowing ratio equate

a lower accuracy superposition prediction.

1.4.1.7 Kasagi et al. (1981)

Heat transfer data on two inclined, staggered, full-coverage arrays of $P/D = 5$ and

10 with $X/D = P/D$ is presented by Kasagi et al. [23]. An analysis of the heat transfer

mechanisms inside of the adiabatic wall is conducted by utilizing a low thermal conductivity

acrylic plate and a high thermal conductivity brass plate. Blowing ratio is varied such that

the large spacing plate has the same amount of total mass injected as the smaller spacing

plate; the values being $M = 0.3$ to 0.7 for the small spacing and $M = 1.1$ to 2.6 for the

large spacing. The mainstream is varied between $U_\infty = 10$ and $20m/s$. Local temperature

measurements are made possible with cholestelic liquid crystal and verified by thermocouple.

The brass plate eliminates any spanwise variation in surface temperature. The headloss as

a function of Reynolds number is given, the large spacing has a 10 times larger headloss

than the small spacing at the same total secondary flow rate. The larger spacing does,

however, have a lower magnitude head loss coefficient. For both the small and large spacing

geometries, the effectiveness decreases as blowing ratio is increased, with a greater effect

for the large spacing. The large spacing shows strips of very low effectiveness in between

the coolant hole exits. It is conjectured that the coolant jet penetrates completely into the mainstream. The brass plate shows considerably higher effectiveness values than the acrylic plate without the noticeable peaks from the coolant holes.

1.4.1.8 Harrington et al. (2001)

Harrington et al. [27] investigate $L/D = 1$ holes, staggered at $P/D = X/D = 7.14$ in a full-coverage array. The novelty of this experiment is utilizing small and large turbulence intensities, $TI = 0.5\%$ and 18% respectively, with a large density ratio of 1.7. A method of reducing error from not having a true adiabatic surface by correcting by using a one-dimensional conduction correction is tested and implemented. The two cases are also simulated computationally using the $RNG\ k - \varepsilon$ model. At these experimental conditions, the intermediate blowing ratio of $M = 0.65$ performs essentially the same as the high blowing $M = 1.0$ case at low turbulence intensities. The high turbulence laterally averaged effectiveness drops by 12% compared to the low turbulence test at the blowing ratio of $M = 0.65$, the lowest difference between the three blowing ratios tested. Comparisons are made with Seller's superposition method [31] and a linear superposition using CFD. The superposition method either over-predicts or under-predicts based on the blowing ratio and streamwise location. The low blowing, low turbulence case shows a fully developed film by the fourth row of holes; the superposition prediction over-predicts after the fully developed section after the fourth row.

1.4.1.9 Kelly and Bogard (2003)

Kelly and Bogard [29] experimentally determine heat transfer augmentation in a full-coverage array for a heated and unheated starting length with varying levels of turbulence intensity. Heat transfer augmentation is affected by turbulence levels; however, this is due to the large increase in turbulence only affecting the uncooled heat transfer coefficient, leaving the heat transfer conductance in the presence of film cooling the unaffected. Net heat flux reduction is calculated using experimentally obtained heat transfer coefficients and adiabatic effectiveness values. No significant difference is seen between the low and high turbulence intensity cases. Single row data is taken to evaluate the predictability of the full-coverage array through the superposition method. Simple superposition fails to accurately predict cooling for the full-coverage arrays. A method using the heat transfer coefficient from the measured row is developed which agrees well with the experimental data.

1.5 Scope of Current Study

A majority of works in full-coverage film cooling are plotted with their case parameters, Figure 1.8. It is clear that the available literature focuses on relatively small hole spacings, $< 15D$. Also, many studies focus on very simple hole orientations, $\alpha = 90°, \beta = 0°$. The current study focuses on larger spacings, $P/D = X/D = 14.5, 19.8$, and angled holes, $\alpha = 30°, 45°, \beta = 45°$, and 20-30 rows of coolant injection. Furthermore, much of the data

sets from the studies below are incomplete; many provide only discrete measurements (i.e. not local) and they do not present both adiabatic film cooling effectiveness and heat transfer augmentation.

The focus of the current project twofold;

- Evaluation of effect of hole orientation and array spacing through the quantification of local heat transfer augmentation and adiabatic film-cooling effectiveness for four full-coverage film cooling surfaces. (Chapters 2, 3 and 4)

- Assess common turbulence models' ability to accurately predict relevant parameters of full-coverage film cooling for a simple geometry from literature. (Chapter 5)

1.5.1   Measurements

In order to asses the effect of array spacing and hole orientation, four different geometries are tested for both heat transfer augmentation and film cooling effectiveness. Each of which are tested with and without a recovery region. All full-coverage surfaces are composed of staggered cylindrical holes. All holes in this study are compounded at $\beta = 45°$. Two spacings are tested, $P/D = 14.5$ and 19.8 along with two inclination angles, $\alpha = 30°$ and $45°$.

It is of interest to determine the performance in the recovery region of the surfaces. This is achieved by shortening the film cooled surfaces by removing a portion of the array

and inserting a flat plate downstream. This effectively reduces the number of coolant rows in the streamwise direction. This recovery region testing is performed for both heat transfer augmentation and effectiveness testing.
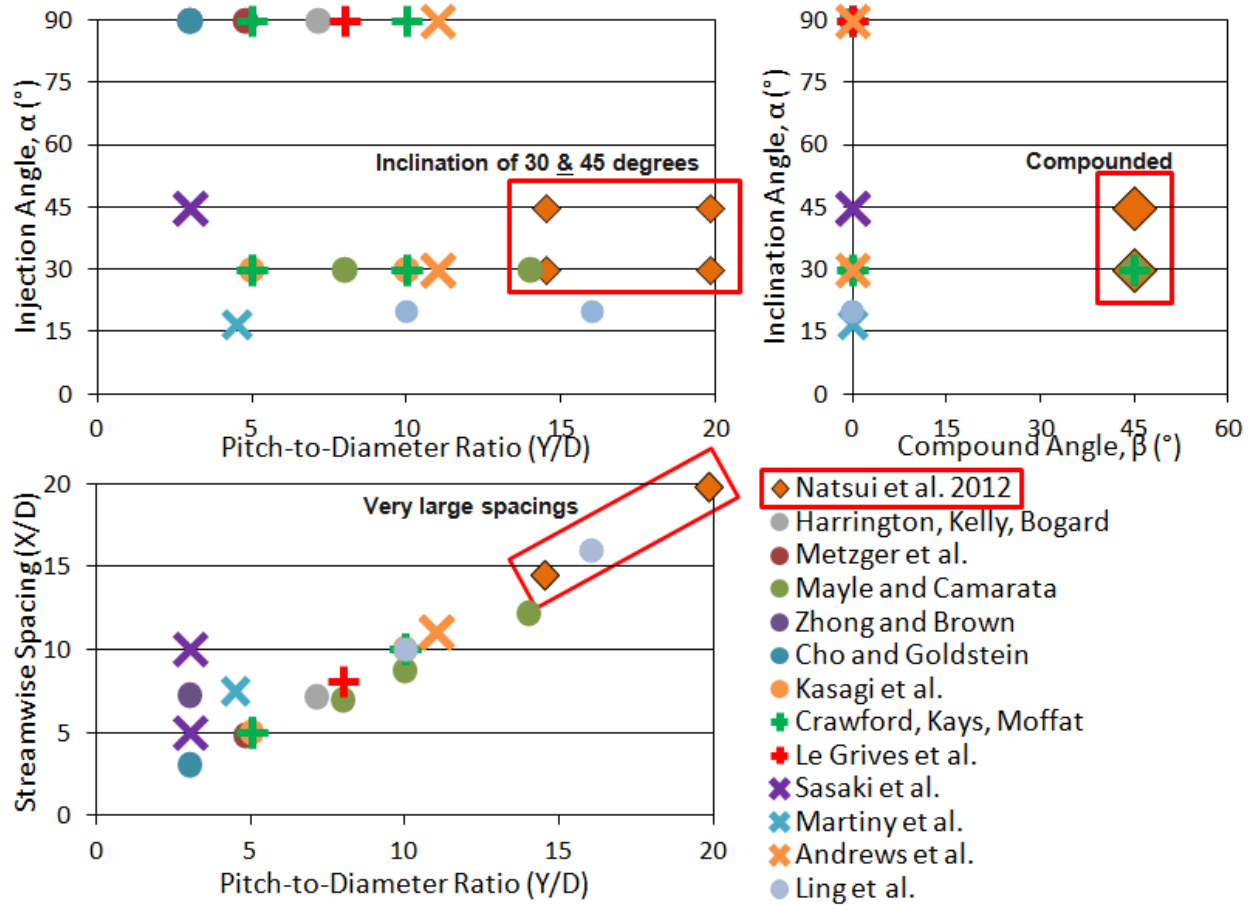
Figure 1.8: Parameters of full-coverage film cooling studies along with current study.

1.5.2 Predictions

The steady RANS equations will be solved with RKE and $SSTKW$ turbulence models in order to predict adiabatic film cooling effectiveness throughout a case from Mayle [15]. This case is also tested experimentally in order to provide local data for a more in depth comparison. In the end this will result in a preferable turbulence model for quick, accurate predictions of full-coverage film cooling in the future.

CHAPTER 2
EXPERIMENTAL SETUP

This chapter describes the physical setup of the experiment. This includes; test surfaces §2.1, wind tunnel §2.2, an explanation of *TSP* §2.3, testing methodology for effectiveness §2.4, and heat transfer §2.5. Experimental uncertainty is explained in §2.6.

2.1   Test Surfaces

All nominal parameters describing the experimental test surfaces for the current study are tabulated in Table 2.1.

Table 2.1: Test matrix describing nominal geometric features of study

Surface	α (°)	β (°)	X/D	P/D	L/D	N_x	N_z	M
FC.A	30	45	14.5	14.5	10.2	20/30	10/10	0.5, 1.0, 2.0
FC.B	30	45	19.8	19.8	10.2	15/22	7/8	0.5, 1.0, 2.0
FC.C	45	45	14.5	14.5	7.2	20/30	10/10	0.5, 1.0, 2.0
FC.D	45	45	19.8	19.8	7.2	15/22	7/8	0.5, 1.0, 2.0

A diagram of each geometry can be found in Figure 2.1.
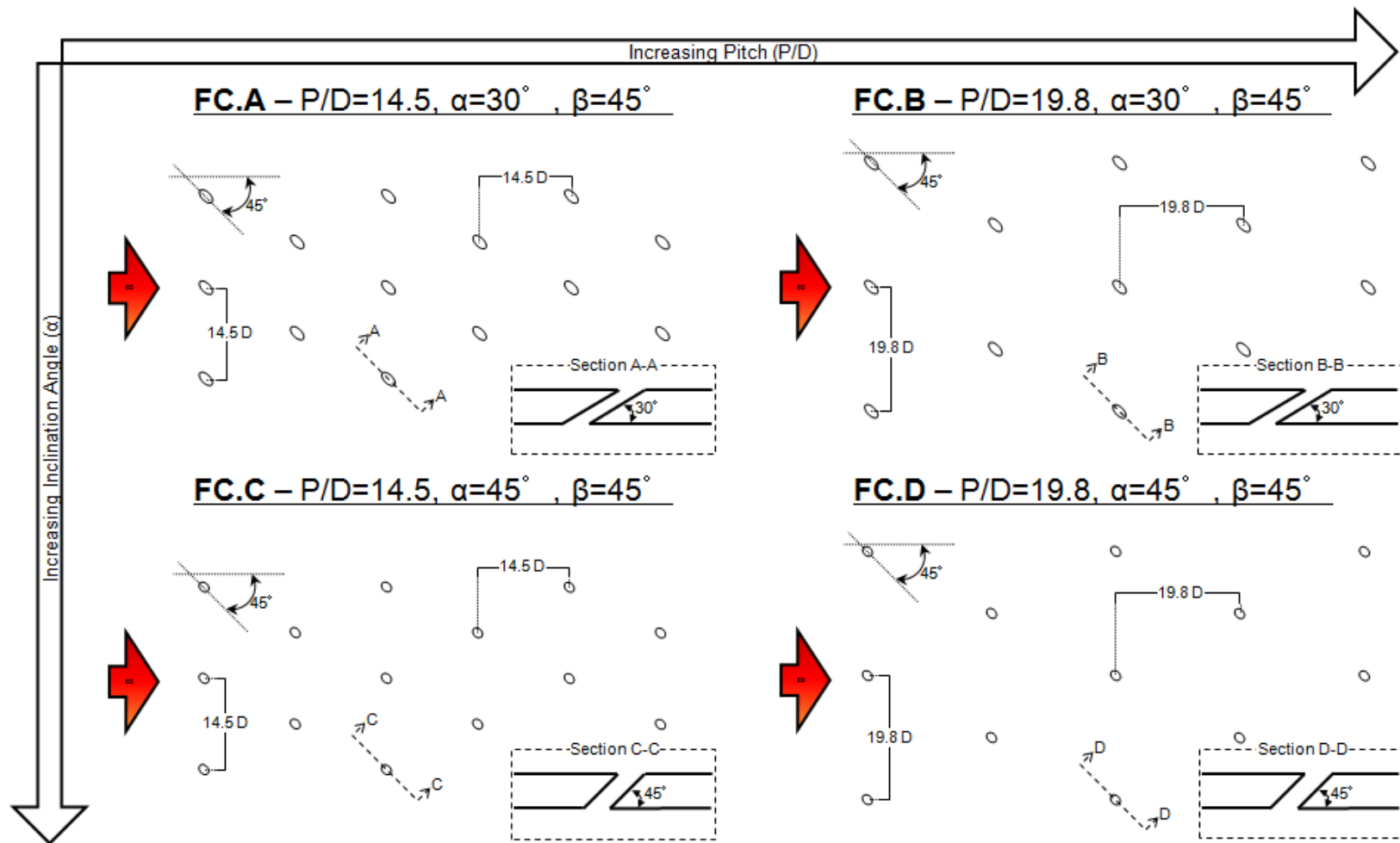
Figure 2.1: Diagrams of all test surfaces.

The test sections are large, $1.2m$ in the flow direction; hence for practical purposes require a segmented design of the whole test surface. Below, in Figure 2.2 is an example of the test surface and how it is broken up into segments.
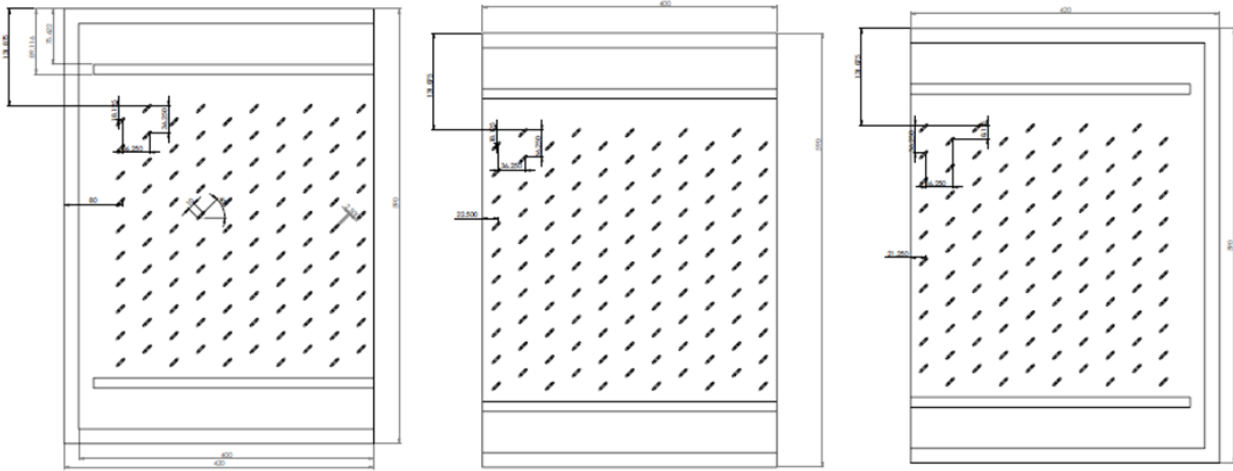
Figure 2.2: Diagram of actual test section composition, separated into three sections.

2.2 Wind Tunnel

A wind tunnel is designed for the study to accommodate the large ($1.2m$ x $0.55m$) test section. This allows for a tunnel tailored for studying large arrays of film holes.

The cross-section of the cross flow duct at the test section is 6" x 42". This corresponds to a height of $60D$ for the test matrix of film holes of $D = 2.5mm$. This ensures the dynamics of the jets leaving the film holes are not affected by the duct. The cross section of the tunnel is sized so that the added mass due to injection is insignificant compared to the main flow;

hence, the study is conducted in a nominally zero pressure gradient boundary layer. The area of the cross flow is 200 times larger than the total area of film holes. At a blowing ratio of $M = 2$, this area ratio would cause a 1% increase in cross flow velocity at the last row of film holes. For a main flow of $U_\infty = 26.5 m/s$ this would be a $0.3 m/s$ increase by the end of the array.
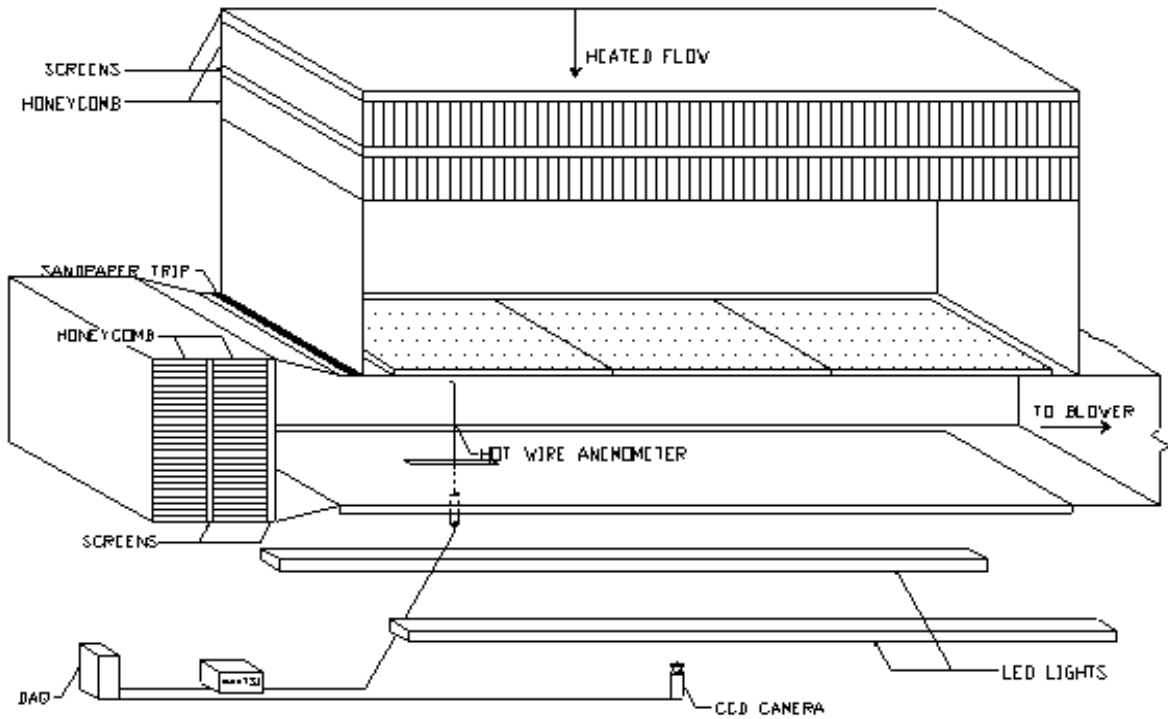
Figure 2.3: Schematic of wind tunnel.

A model of the tunnel is shown in Figure 2.3. There is a $45cm$ conditioning section upstream of the test section. There are 2 honeycombs of $1.3cm$ cell size and $L/D_H = 6$. There are also 3 screens. These were installed to reduce the turbulence intensity of the main

flow. After the conditioning section there is a slight 1-D nozzle with an area ratio of 2 leading up to the test section.

2.2.1 Blowers

The coolant flow is supplied by an $11kW$ Spencer Vortex blower capable of $35kPa$ and $0.3m^3/s$. The main flow is induced by a $5kW$ Ziehl-Abegg fan capable of $-1.5kPa$ and $6.6m^3/s$.

2.2.2 Tunnel Flow Measurements

Several static pressure readings are taken along the test section to verify there is not a significant pressure gradient imposed on the flow as the coolant is injected and as the boundary layer develops. Over the length of the $1.2m$ test section there is a $15Pa$ pressure drop corresponding to a $-12.5Pa/m$ favorable pressure gradient. With a pressure drop across the film hole on the order of $2kPa$, this is a negligible pressure gradient for the tests.

The freestream velocity and turbulence intensity are quantified with a constant temperature anemometer *(CTA)*. The *CTA* records samples at a rate of $10kHz$ over $10s$. This data set averaged with other in the center of the duct show a freestream velocity of $U_\infty = 26.5m/s$ for the tests. This measurement is verified with a pitot-static measure-

ment. The root mean square of the turbulent fluctuations is obtained from this data and the turbulence intensity (TI) of the mainstream is quantified at 0.7%.

The momentum boundary layer thickness at the first row of film holes is quantified and should be on the order of $1/4$ the diameter of the film holes for realistic scaling. The CTA is used to measure the boundary layer. In the boundary layer, samples are taken at a rate of $10kHz$ for 3 seconds per point. Measurements are taken starting from $0.13mm$ away from the wall. This allows the measurements to be resolved as close to the wall as $y^+ = 10$.

From Figure 2.4, the velocity profile normalized by the freestream velocity of $26.5m/s$, one can see the boundary layer thickness. Based on a boundary layer thickness of 99% the freestream the boundary layer thickness at leading edge of the test section is $8.8mm$. Figure 2.4 also shows the turbulence intensity as a function of distance normal from the wall. This shows the turbulent fluctuations die down to $TI < 1\%$ in the mainstream.

This data is then scaled by wall coordinates provide a curve which can be integrated for momentum thickness, δ_2. Friction velocity $u_\tau = \sqrt{\tau_w/\rho}$ and the vertical shift to correct for wall normal coordinate are determined by matching the law of the wall $(C = 5.2, \kappa = 0.41)$. A modified wake function from Guo et al. [33] is then added to the van Driest profile. $10,000$ points from $y^+ = 10^{-2}$ to $y^+ = 10^3$, spaced logarithmically, are integrated from $y/\delta = 0$ to 1 with rectangular rule to calculate the integral thicknesses.

$$u^+ = y^+ \tag{2.1}$$

$$u^+ = \frac{1}{\kappa} \ln y^+ + C \tag{2.2}$$

$$u^+ = \int_0^{y^+} \frac{2 dy^+}{1 + \sqrt{1 + 4\kappa^2 y^{+2} \left[1 - \exp\left(\frac{-y^+}{A^+} \right) \right]^2}} \tag{2.3}$$

$$u^+ = \int_0^{y^+} \frac{2 dy^+}{1 + \sqrt{1 + 4\kappa^2 y^{+2} \left[1 - \exp\left(\frac{-y^+}{A^+} \right) \right]^2}} + \frac{2\Pi}{\kappa} \sin^2\left(\frac{\pi y^+}{2\delta^+} \right) - \left(\frac{y^+}{\delta^+} \right)^3 \frac{1}{3\kappa} \tag{2.4}$$

Figure 2.5 shows the linear region, Equation 2.1, the Law of the Wall , Equation 2.2, and a modified van Driest function, Equation 2.4, along with the measured velocity profile.
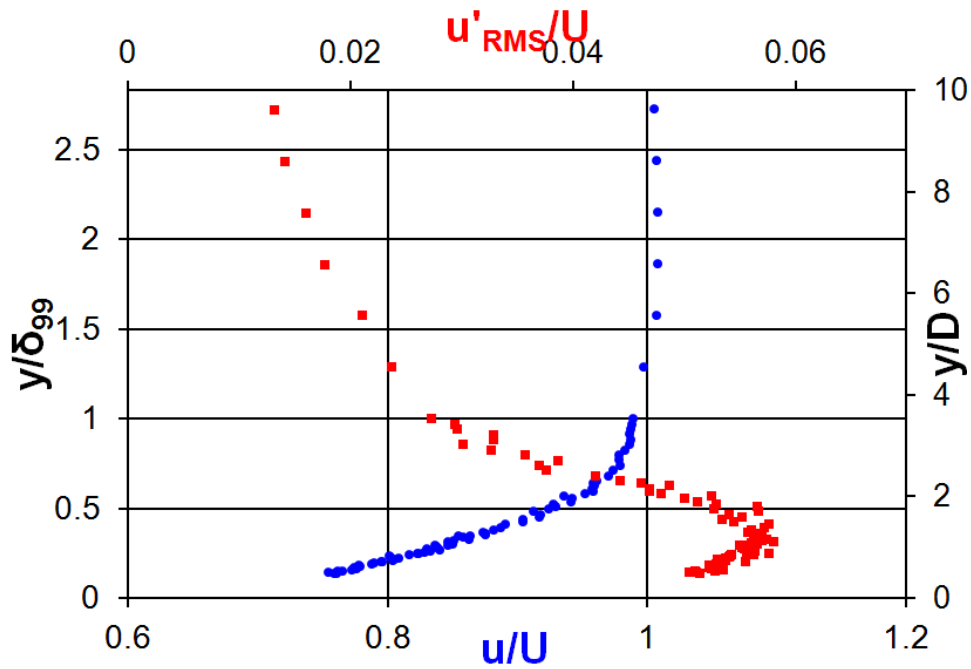
Figure 2.4: Measurement of upstream hydrodynamic boundary layer scaled by outer coordinates.

Table 2.2 provides a summary of all parameters relevant to this analysis.

Table 2.2: Parameters describing the upstream hydrodynamic boundary layer

Freestream Velocity (m/s)	U_∞	27.2
99% Boundary Layer Thickness (mm)	$\delta_{.99}$	8.8
Displacement Thickness (mm)	δ_1	1.04
Momentum Thickness (mm)	δ_2	0.75
Shape Factor	$H = \delta_2/\delta_1$	1.39
Reynolds Number on δ_2	$Re_2 = U_\infty\delta_2/\nu$	1300
Reynolds Number on D	$Re_D = U_\infty/\nu$	4250
Freestream Turbulence Intensity	$TI = u_{RMS}/U_\infty$	< 0.01
99% Boundary Layer Thickness to Hole Diameter Ratio	$\delta_{.99}/D$	3.5
Discplacement Thickness to Hole Diameter Ratio	δ_1/D	0.42
Momentum Thickness to Hole Diameter Ratio	δ_2/D	0.30
Friction Velocity (m/s)	$U_\tau = \sqrt{\frac{\tau_w}{\rho}}$	1.25
Outer-Inner Length Scale Ratio	$\delta^+ = \delta_{.99}U_\tau/\nu$	694
Cole's Wake Strength	Π	0.27
Constant in van Driest's Damping Function	A^+	26
von Karman's constant	κ	0.41
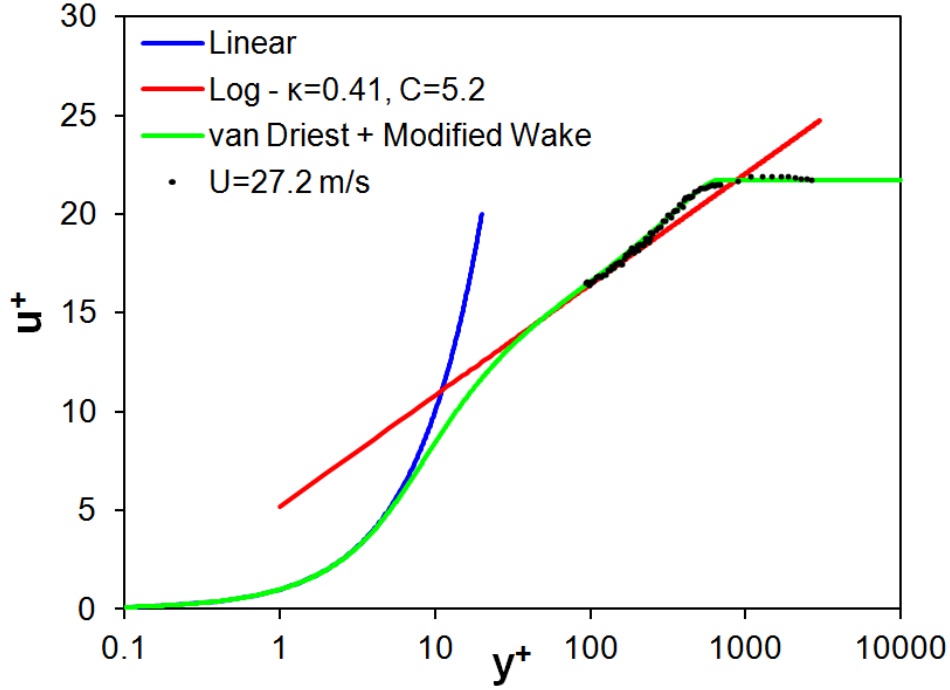
Figure 2.5: Inner scaled measurements of hydrodynamic upstream boundary layer.

2.3 Temperature Sensitive Paint (TSP)

Temperature sensitive paint is made by combining a luminescent molecule and polymer binder. Surfaces are coated with this paint and illuminated with light of $475nm$ in wavelength, exciting the luminescent molecule. This molecule returns to its original energy state through the competing effects of emission of the longer wavelength light and thermal quenching. The probability of thermal quenching increases with increased temperature; thus the intensity is inversely proportional to the temperature. A full explanation on the experimental use of TSP used in this experiment is outlined by Liu [34]. The intensity variation

can be captured by means of a CCD camera and long pass filter, and the camera takes images at a minimum rate of 200 to $350ms$ to capture the fluorescence at steady state.

The pictures gathered with the CCD camera are then processed using in house codes which take the raw image files and process them into temperature distributions. A $1200x1600$pixel resolution picture is taken with the camera. The calibration curve for TSP is based off of an intensity ratio as a function of a temperature difference. Two sets of pictures are needed to gather a temperature distribution, see Figure 2.7. One picture is needed as a reference, the cold picture, with a known temperature over the entire surface being measured, along with the hot picture of the unknown temperature profile. This method of taking intensity ratios leads to a technique which is rather insensitive to lighting and paint variations, a huge strength of TSP. Eight pictures are taken for both the hot and cold set and are averaged into one picture. This multiple sampling is used to reduce the noise of the pictures.

By means of in house Matlab codes developed specifically for processing TSP into usable heat transfer data, the intensity values of the cold pictures are read and averaged; the same procedure takes place for the hot images taken at steady state. Then through the use of calibration curves of the TSP, temperature values are obtained from the ratio of the intensity values of the hot to cold images.These calibration curves are obtained through experiment, some curves are shown in Figure 2.8.

Figure 2.6: Picture of the *TSP* experimental setup in use; excitation and *DAQ*, the *TSP* is out of view at the top of the picture.
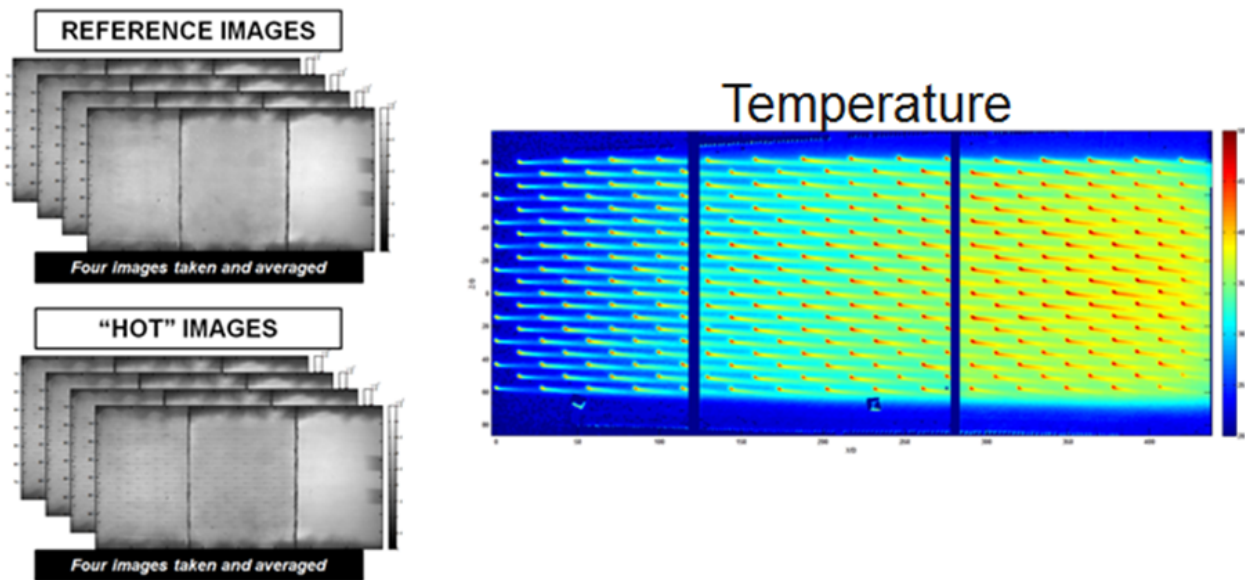
Figure 2.7: Method of converting intensity ratio to temperature matrix.

2.4 Effectiveness Experimental Setup

To obtain values of adiabatic film cooling effectiveness, a low thermal conductivity test surface is machined with the full-coverage geometry into the material. The flow side is coated with *TSP*, as shown in Figure 2.9. The temperatures are obtained from thermocouples in the freestream and in the holes, and adiabatic wall temperatures measured with *TSP*. These values are combined to yield local contours of effectiveness.

2.4.1 The Adiabatic Wall – Rohacell®RIMA

The material chosen for the test surface has a significant effect on the final adiabatic film cooling effectiveness results. Acrylic, a relatively low thermal conductivity material ($k = 0.25W/m - K$) provides very poor quality effectiveness data. Hence, the current study uses Rohacell®RIMA, low density closed cell foam as the adiabatic test surface. The roughness of the RIMA series is minimal; hence, it is especially suited for painting applications. The thermal conductivity of Rohacell®is $k = 0.029W/m - K$. Due to the low strength of the material, aluminum brackets are cold-welded to the backside; these brackets improve data quality by minimizing the deflection of the test section during testing. The aluminum brackets on the backside do not influence the temperature distribution on the flow side. The surface is sanded prior to painting to further increase the smoothness of the surface.
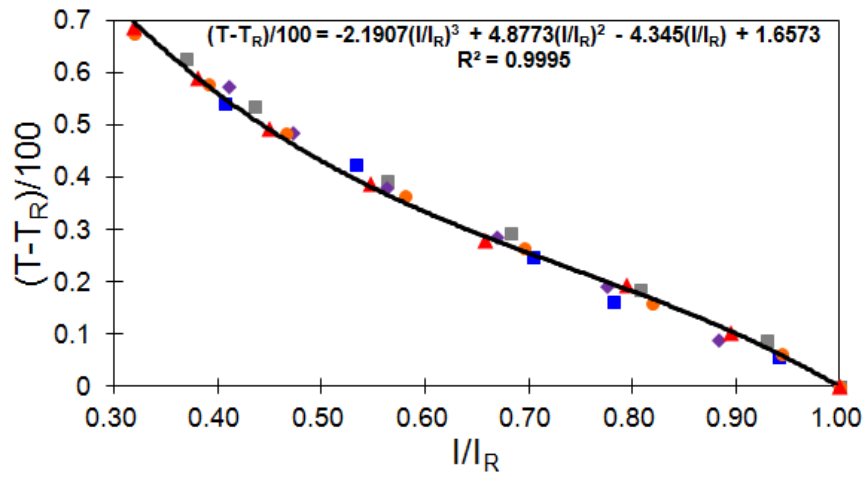
Figure 2.8: Sample TSP calibrations.
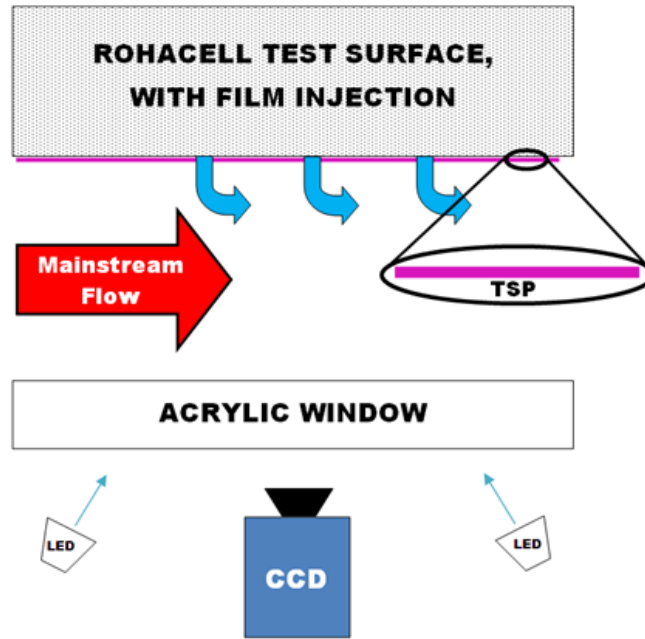
Figure 2.9: Diagram of adiabatic film cooling effectiveness (η) testing technique.

2.5   Heat Transfer Augmentation Experimental Setup

The measurement of heat transfer augmentation requires an experimental setup different from the effectiveness testing. In concept, it is a steady state method for obtaining the heat transfer coefficient. Constant heat flux heaters are mounted on an acrylic test surface and coated with *TSP*, as shown in Figure 2.10. From an energy balance it is clear that in order to obtain the heat transfer coefficient, quantification of all the heat flow in, out and across the convective surface is necessary. The heat rate information for a 1-D process is quantified including the heat generated by Joule heating, heat conducted through the acrylic, and heat radiated to the tunnel. With these heat rates quantified, the heat removed through convection can be determined. First, the heat transfer coefficient defined by the temperature different between the wall and the freestream, Equation 1.2, is determined from this convected heat rate. Then the film effectiveness distribution, previously obtained, is overlaid on the data and used to define a heat transfer coefficient in the presence of the film, Equation 1.3. Finally, this corrected heat transfer coefficient is scaled by the heat transfer coefficient distribution without blowing, Equation 1.5, resulting in local heat transfer augmentation values, h/h_0.

2.5.1 Heaters

A constant heat flux condition is desired from the surface of interest. Since the heated surface has features that cannot be covered by the heaters such as film cooling holes, the heaters are installed around them without disturbing the flow that each feature has. The area if interest is heated as much as possible in order to obtain an acceptable temperature difference between the wall and the fluid. These foil heaters are made out of $t = 0.51mm$ thick stainless steel type 321. This stainless steel has an electrical resistivity of $\rho_{el} = 79E^{-8}\Omega - m$ at $350K$. In order to account for ρ_{el} changing with temperature, data from Ho and Chu [35] is curve fit and ρ_{el} is allowed to vary with temperature over the test surface.

Heaters are cut from the steel sheet and double sided Kapton tape is applied on one side of the heater. The heaters with the Kapton are then placed on a sheet for painting on the side opposite to that with the Kapton tape. These painted heaters are then baked at a temperature close to $90°C$ (above their operating temperature) for half an hour. Kapton tape is used because it is electrically insulative, thin and its adhesive is intended for high temperatures. This helps ensure good heater performance. The heaters are then applied to the acrylic test surfaces in series.

2.5.2   Heat Flux Measurements

The series installation allows the heat rate to be determined by the current (i), providing a much more accurate method of calculation than installing them in parallel and measuring the voltage drops. The gain in accuracy is due to the very inconsistent nature of contact resistances, resulting in each leg of a parallel circuit receiving a slightly different voltage. A shunt resistor, $R = 1m\Omega$ and $i = 100A$ maximum, is installed inline with the heaters. A Keithley model 2000 multimeter is used to measure the voltage drop across the shunt resistor, and from this voltage and the resistance of the shunt, the current through the circuit is calculated. The Keithley multimeter features a $0.1\mu V$ resolution with bias of $\pm(0.06\%)$ the reading. The voltage drop across the shunt during testing is on the order of mV.

2.6   Experimental Uncertainty

Quantification of experimental uncertainty for the experiment has been conducted. The propagation of error effect on the absolute error of the resultant, Φ, is quantified through Equation 2.5, where there are $j = 1, 2, \ldots, n$ measurands, φ_j.

$$u_\Phi = \sqrt{\sum_{j=1}^{n} \left(\frac{\partial \Phi}{\partial \varphi_j} u_{\varphi_j} \right)^2} \tag{2.5}$$

In cases where the partial derivatives from Equation 2.5 are too challenging for a symbolic manipulator, the partials are approximated through a finite central difference as in Equation

2.6.

$$\frac{\partial \Phi}{\partial \varphi} \approx \frac{\Phi(\varphi + u_\varphi) - \Phi(\varphi - u_\varphi)}{2u_\varphi} \tag{2.6}$$

To evaluate the total uncertainty of each measurand the bias and precision uncertainty are both considered as in Equation 2.7.

$$u_\varphi = \sqrt{B_\varphi^2 + P_\varphi^2} \tag{2.7}$$

The bias, B_φ, is given by the measurement device specifications, or if not listed, half the resolution of the reading is used. The precision, P_φ, is computed by taking several samples of the measurand and computing the standard deviation. The standard deviation is then multiplied by the appropriate factor (Z-score or t-score) for a 95% confidence interval.

2.6.1 Geometric Uncertainty - Actual Values

After machining, the geometries are re-evaluated and the deviation from nominal is quantified, shown in Table 2.3. Using this data, the non-dimensional spacings are evaluated along with their uncertainty, Table 2.4.
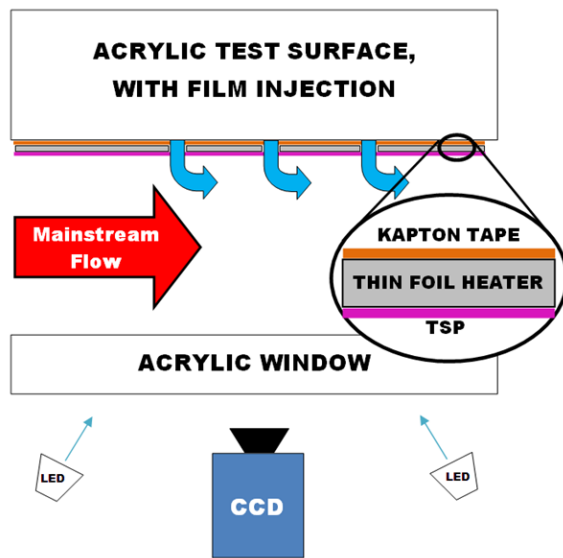
Figure 2.10: Diagram of heat transfer augmentation (h/h_0) testing technique.

Table 2.3: Geometric uncertainty for all test surfaces

Surface	Material	D (mm.)	u_D (mm.) 20:1	X (mm.)	u_X (mm.) 20:1	P (mm.)	u_P (mm.) 20:1
FC.A	Rohacell	2.714	0.041	36.18	0.38	36.42	0.65
FC.B	Rohacell	2.714	0.041	49.08	0.71	49.88	0.28
FC.C	Rohacell	3.028	0.072	36.14	0.13	36.14	0.38
FC.D	Rohacell	3.028	0.072	49.57	0.20	48.34	4.34
FC.A	Acrylic	2.353	0.037	36.25	0.43	36.31	0.63
FC.B	Acrylic	2.353	0.037	49.49	0.62	49.63	0.30
FC.C	Acrylic	2.353	0.037	36.11	0.53	36.16	0.30
FC.D	Acrylic	2.353	0.037	49.17	0.33	49.18	0.38

The Rohacell cases tend to deviate more from nominal due to the softness of the Rohacell allowing the runout of the endmills to more heavily affect the resulting hole. Also, the surfaces inclines at $\alpha = 30°$ have a larger hole diameter than the $\alpha = 45°$ due to more runout and walking of the endmills. These large uncertainties have led our group to pursue in-house machining which has resulted in far better quality control of the test surfaces.

Table 2.4: Actual values of resulting non-dimensional spacings

Surface	Test	Nominal	X/D	P/D
FC.A	η	14.5	13.33 ± 0.24	13.42 ± 0.31
FC.B	η	19.8	18.08 ± 0.38	18.38 ± 0.30
FC.C	η	14.5	11.94 ± 0.29	11.97 ± 0.31
FC.D	η	19.8	16.37 ± 0.39	15.96 ± 1.48
FC.A	h/h_0	14.5	15.40 ± 0.30	15.43 ± 0.36
FC.B	h/h_0	19.8	21.03 ± 0.42	21.09 ± 0.36
FC.C	h/h_0	14.5	15.35 ± 0.33	15.37 ± 0.27
FC.D	h/h_0	19.8	20.89 ± 0.36	20.90 ± 0.37

2.6.2 Uncertainty of Dependent Variables

The uncertainty tree for heat transfer coefficient is shown in Figure 2.11. The calculated values are broken down into each measurand and the last values seen are the uncer-

tainties in each measured value. This tree allows a view at each parameter contributing to the uncertainty of the final calculated value. From Figure 2.11 one can see the contributing factor to uncertainty in the numerator of heat transfer enhancement. There are several measurands contributing to the experimental uncertainty in heat transfer enhancement leaving the final uncertainty in heat transfer augmentation much larger than the uncertainty in adiabatic film-cooling effectiveness. Similar trees exist for film cooling effectiveness, blowing ratio, and indeed every resultant parameter.
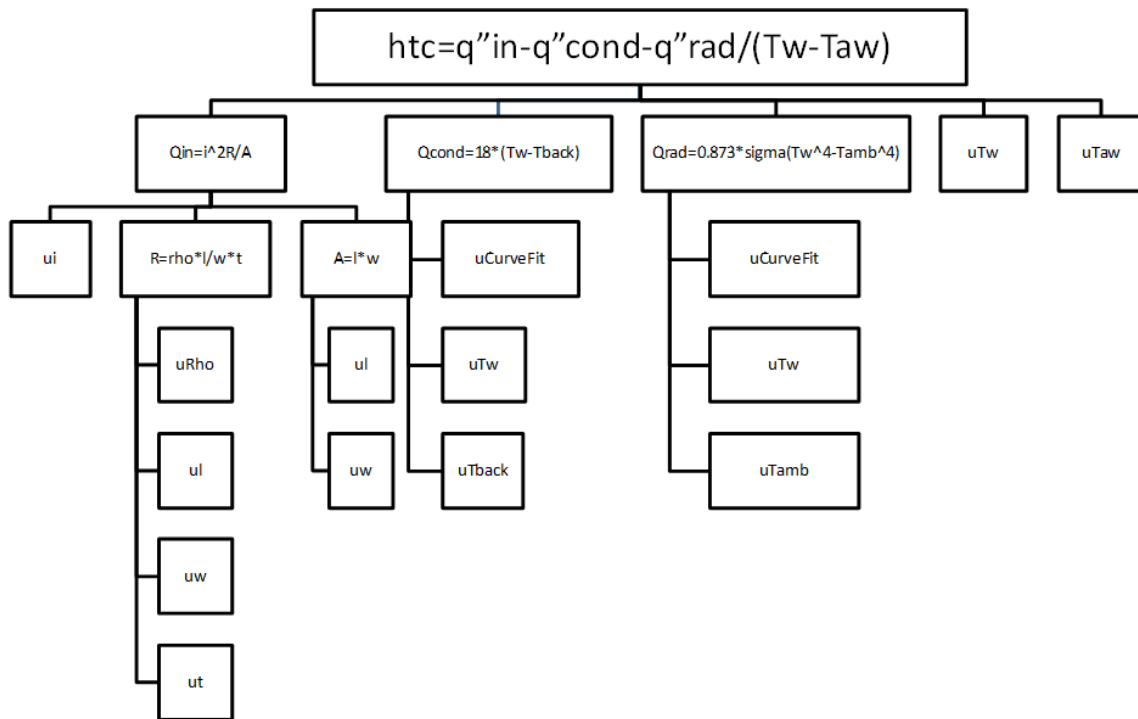

Figure 2.11: Measurands contributing to the calculation of heat transfer coefficient.

The uncertainty trees represent the j measurands, φ_j which contribute to the calculation of Φ. In the case of adiabatic film cooling effectiveness and blowing ratio, the partials of the resultant with respect to each measurand are calculated analytically based off of the

appropriate relationships. In the case of calculating the partials for the heat transfer coefficient, a singular perturbation method is used due to the complexity of the relationships, Equation 2.6.

Film cooling effectiveness and blowing ratio as well as intermediate parameters necessary for the calculation of η and M are shown with their typical value and associated experimental uncertainty in Table 2.5. At a value of $\eta = 0.2$, $u_\eta = 0.02$, also for $\eta = 1.0$, $u_\eta = 0.08$. At a low blowing ratio of $M = 0.63$, $u_M = 0.063$, 10% of the value.

Table 2.5: Selected measurands and resultant uncertainties

Parameter	Symbol	Units	Typical Value	u (20:1)	% Uncertainty
Coolant Temp	T_c	°C	58	2.8	-
Mainstream Temp	T_∞	°C	23	0.4	-
Adiabatic Wall Temp	T_{aw}	°C	30	0.5	-
Coolant Mass Flow	$\dot{m}_c$	kg/s	0.022	0.00032	1.5%
Coolant Metering Area	A_c	cm^2	18	0.87	4.8%
Mainstream Mass Flux	ρU_∞	kg/s/m^2	23.85	1.86	7.8%
Effectiveness	η	-	0.2	0.02	10%
Blowing Ratio	M	-	0.63	0.063	10%
HTC Augmentation	h/h_0	-	1.2	0.16	14%

A repeatability investigation is conducted for the adiabatic film cooling effectiveness tests. Measurements of the same test are taken over several different days to ensure ex-

perimental repeatability and consistency. Laterally averaged film cooling effectiveness from

four tests on four different days are averaged together at each value of x/D shown in Figure

2.12. With this mean, the RMS of the deviation of each run is calculated and scaled by

the mean. The data indicates the experiment is repeatable in laterally averaged film cooling

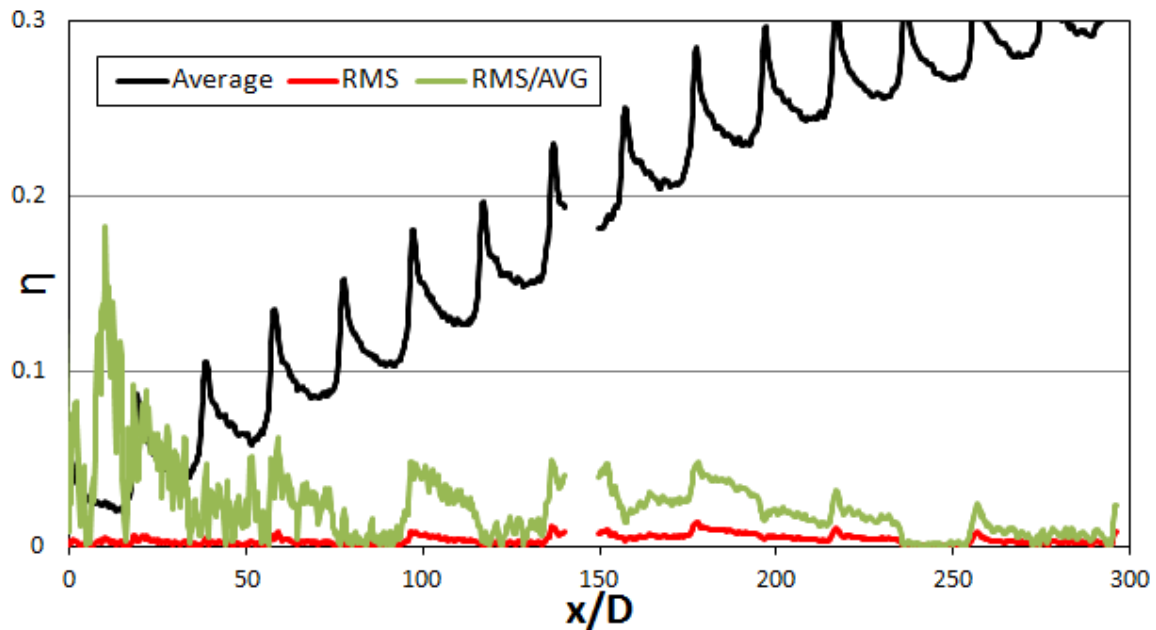effectiveness to within 3% at values of effectiveness larger than $\eta = 0.1$.

Figure 2.12: Repeatability testing of FC.B, M=0.5.

CHAPTER 3
ADIABATIC FILM COOLING EFFECTIVENESS

3.1   Data Reduction

The temperature matrix is processed as described in the *TSP* section, §2.3, and is assumed equal to the adiabatic wall temperatures of interest. From here, the coolant and mainstream temperatures are used to non-dimensionalize the measured adiabatic wall temperatures into an effectiveness matrix.

$$\eta_{i,j} = \frac{T_\infty - T_{aw_{i,j}}}{T_\infty - T_c} \tag{3.1}$$

This local profile is then averaged laterally to obtain the laterally averaged effectiveness profile, $\bar{\eta}$.

$$\bar{\eta}_j = \frac{\sum\limits_{i=1}^{N} \eta_{i,j}}{N} \tag{3.2}$$

3.2   Results – Adiabatic Film Cooling Effectiveness

3.2.1   Experimental Validation of Film Cooling Effectiveness

The current experimental film cooling effectiveness data is compared with literature in order to assure the current experimental procedure is valid. Here, the comparison with Mayle and Camarata [15] is shown for four different blowing ratios in Figures 3.1-3.4.
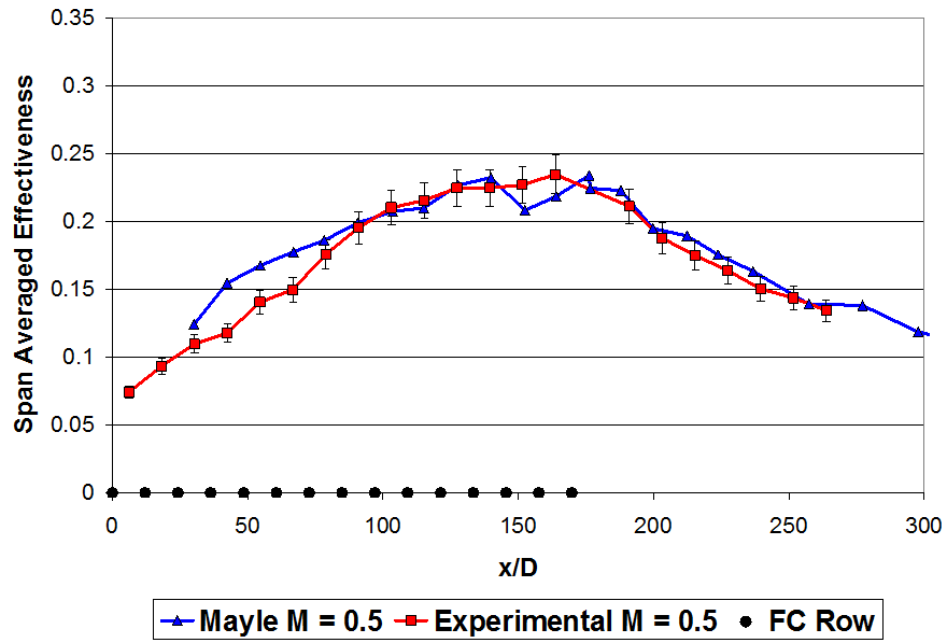

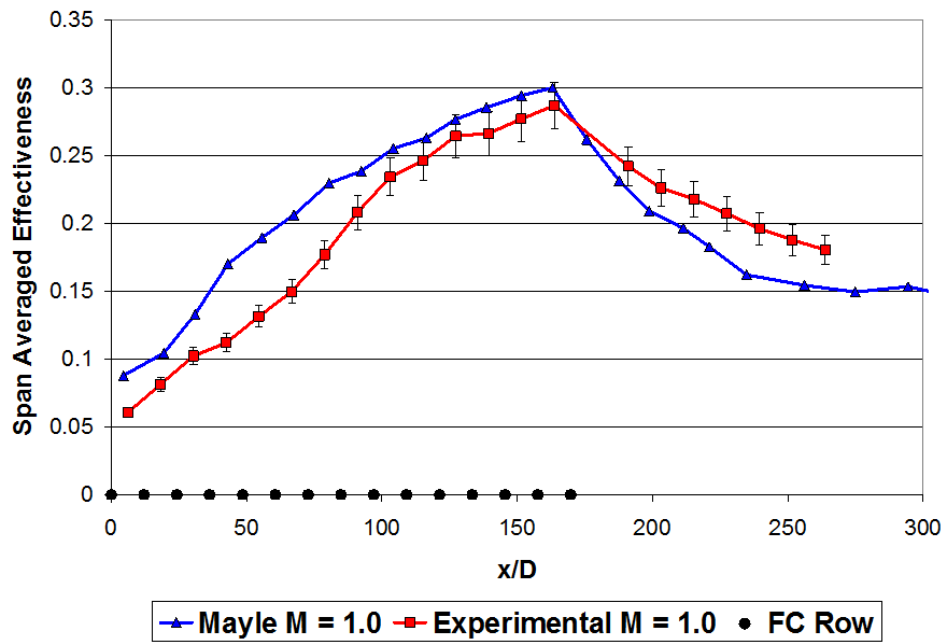Figure 3.1: Comparison with Mayle et al. at blowing ratio $M = 0.50$.

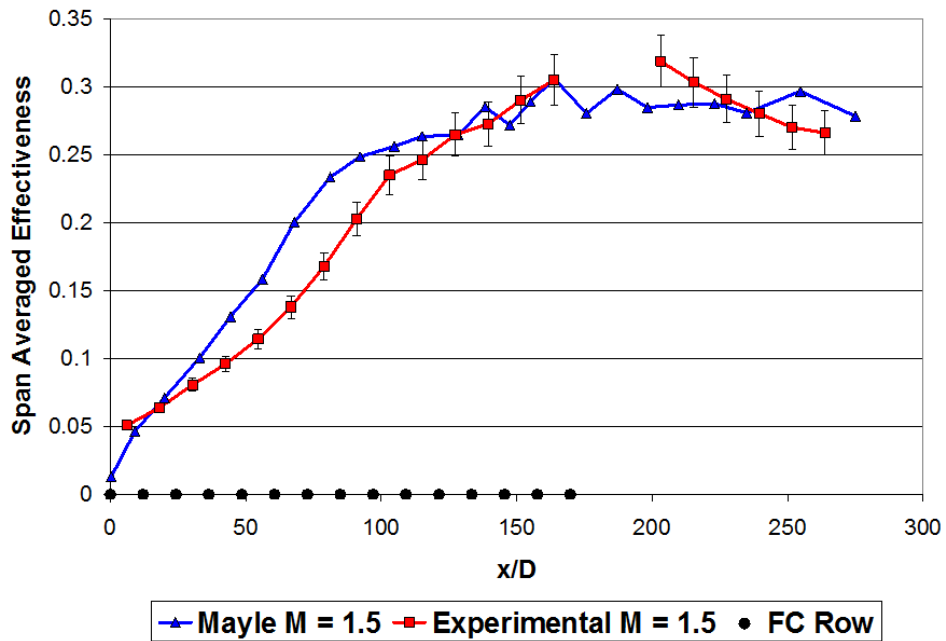Figure 3.2: Comparison with Mayle et al. at blowing ratio $M = 1.00$.

Figure 3.3: Comparison with Mayle et al. at blowing ratio $M = 1.50$.

3.2.2   Local Physics

Representative local distributions of adiabatic film cooling effectiveness, η, are taken from FC.C ($P/D = 14.5, \alpha = 30°$), Figure 3.5. At the low blowing rate, $M = 0.5$, the jets are very well attached. The individual jets are clearly well attached with high local values of effectiveness immediately following injection. Throughout the array at this low blowing rate, the effectiveness continuously builds downstream. The effectiveness profile has several distinct local maxima and minima, the individual jets are clearly seen throughout the array. At the moderate blowing rate, $M = 1.0$, the jets are already lifting. This is due to the low density ratio in the experiments, $DR \approx 0.85$, which increases the momentum flux ratio for a given blowing rate. Due to this effect, the jets are not as well attached as can be seen through the much narrower effectiveness profile of much lower magnitude. After several rows, the magnitude picks back up and by the end of the array, surpasses the low blowing rate. The profile is much more uniform at this moderate M as compared with the low M.

At the high blowing ratio tested, $M = 2.0$, the jets are clearly lifted; however, they return to the surface to provide the highest magnitude of cooling which is also the most uniform. An interesting local feature of the film can be seen at this high blowing ratio. Due to the compound injection, the film generates a lateral momentum. This lateral momentum is overwhelmed by the mainstream at low blowing ratios, but at this larger M the film clearly migrates laterally. This had to be accounted for during data processing to ensure data is taken from a section representing an infinite array.
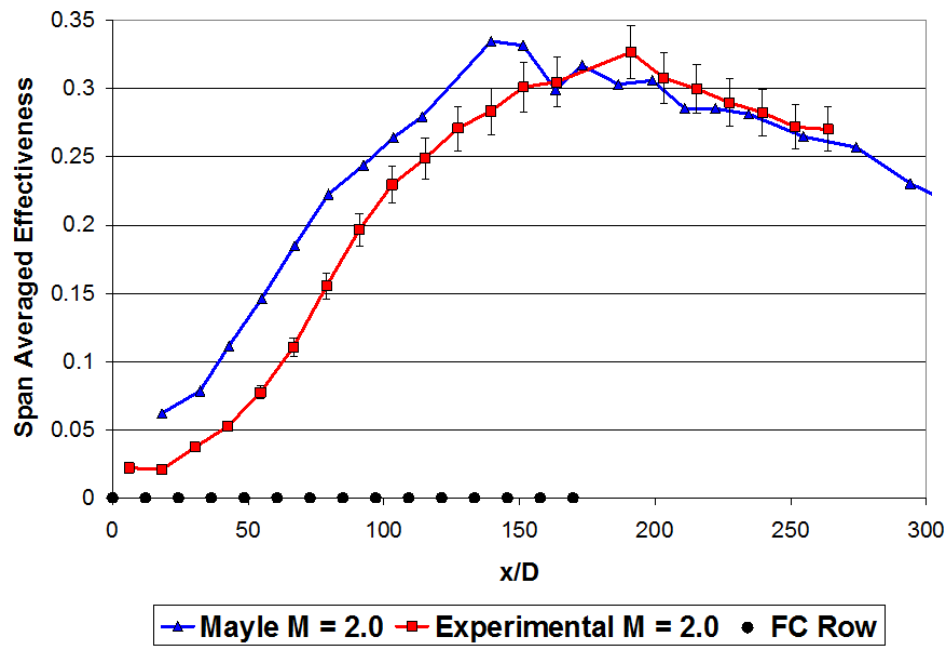
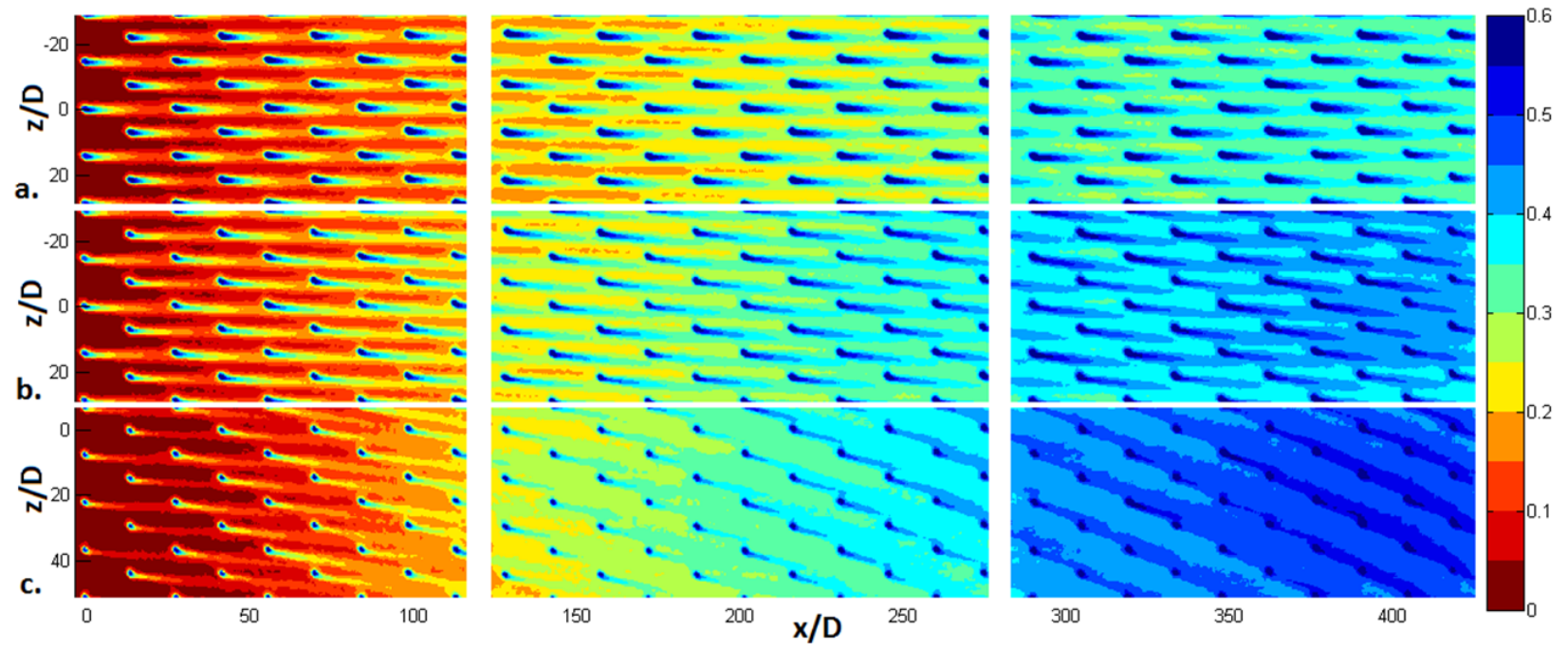Figure 3.4: Comparison with Mayle et al. at blowing ratio $M = 2.00$.

Figure 3.5: Local adiabatic film cooling effectiveness throughout FC.C; (a) M=0.5 (b) M=1.0 and (c) M=2.0.

Detailed local variations with blowing ratio at rows 7, 8 and 9 are shown for several nominal blowing ratios in Figure 3.6. At low blowing, the jets are well attached and provide a large footprint of high effectiveness. As the blowing rate is increased the effectiveness profile narrows laterally and the effectiveness remains at some moderate value and persists several diameters downstream.
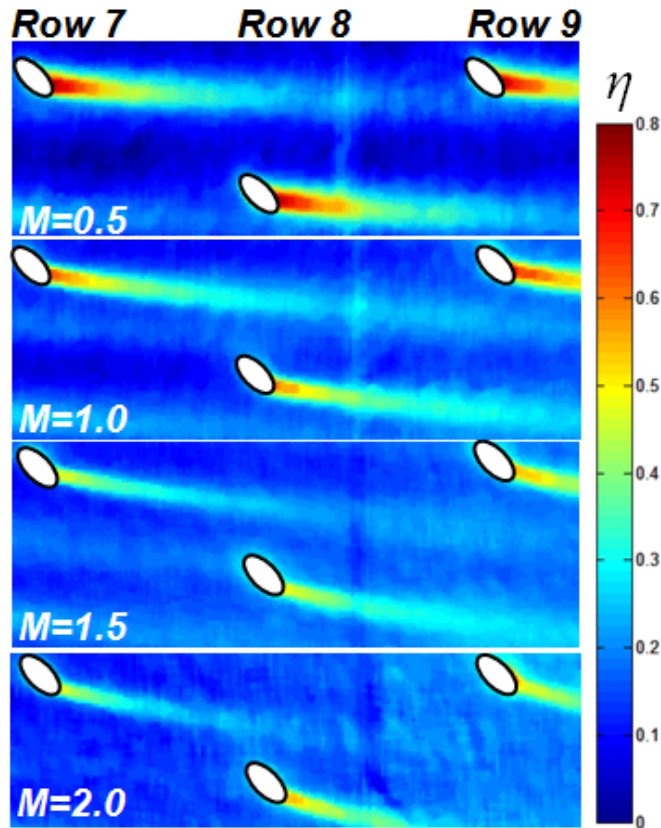

Figure 3.6: Zoomed in view of rows 7, 8 and 9 for FC.C at various blowing ratios.

Streamwise cuts which are local in z, seen in Figure 3.7, show the lateral variation of film cooling effectiveness at $x/D = 15$. At this streamwise location the low blowing cases far exceed the higher blowing rate due to jet liftoff. Even at this first row, the lateral

momentum of the high blowing case shifts the maxima laterally from the injection location.
Further downstream, the higher blowing rate is exceeding the lower blowing cases in film
cooling effectiveness as the jets which have lifted initially return to the surface and provide
cooling.
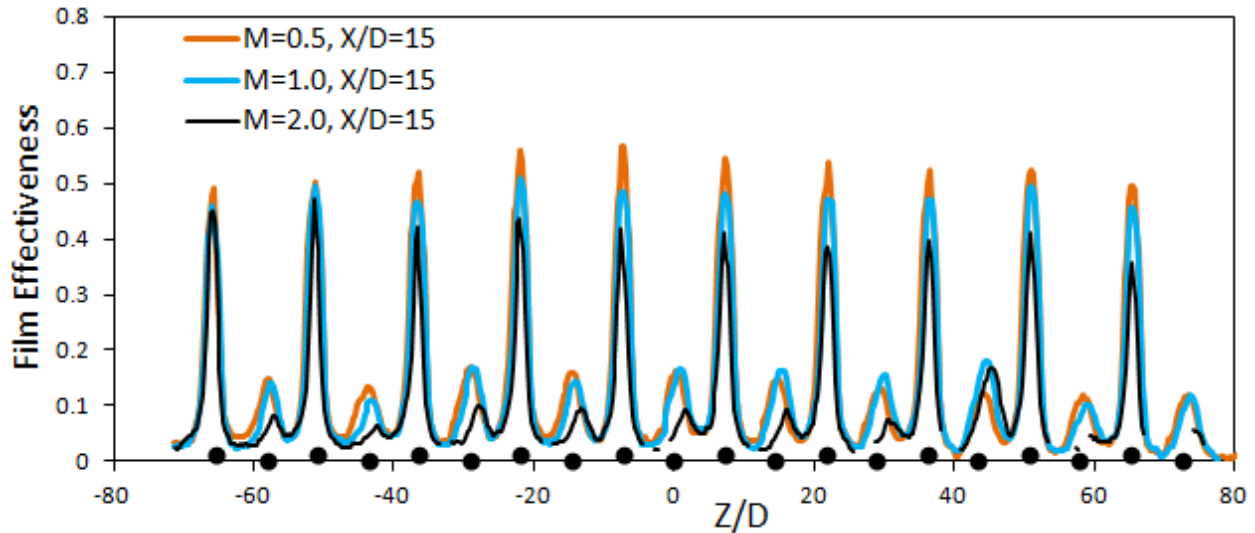
Figure 3.7: Lateral cuts of local film cooling effectiveness at $M = 0.5, 1.0$ and 2.0

3.2.3   Averaged Values

The local data is then laterally averaged, plotted in Figure 3.10. A trend due to
blowing ratio amongst all geometries is clear. At $M = 2.0$, the laterally averaged effectiveness
throughout the first several rows is noticeably lower than that of the lower blowing rates.
This is a clear indication of the jets lifting at this higher blowing rate. Further downstream,
however, the profile for the high blowing rate picks back up and by the end of the array

67

surpasses the low blowing ratio profiles. This coolant which has been ejected from the wall eventually returns to provide significant cooling.

A comparison between injection angles and row spacing may also be made from this laterally averaged data. Row spacing has a definite effect as can be seen by the approximately 35% higher effectiveness by the end of the array. The amount of coolant spent happens to be 35% higher as well, so the physics of the film is not affected at these large spacings. When looking between two different injection angles, the difference is hard to distinguish. The injection angle, although locally significant, has a second order impact on the laterally averaged effectiveness throughout several rows.
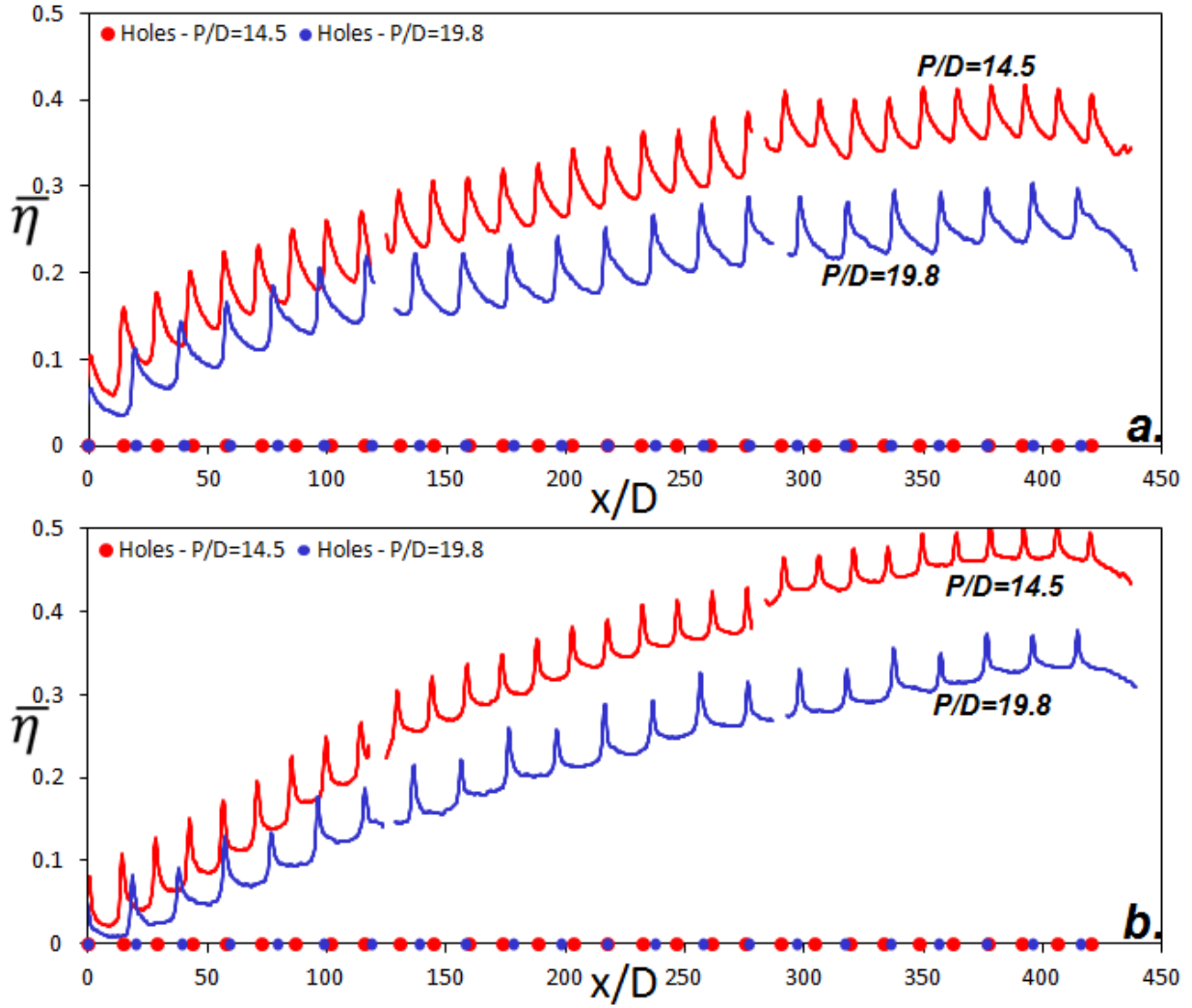
Figure 3.8: A comparison between two different hole spacings with identical hole geometries; $a.M = 0.5$ and $b.M = 2.0$.
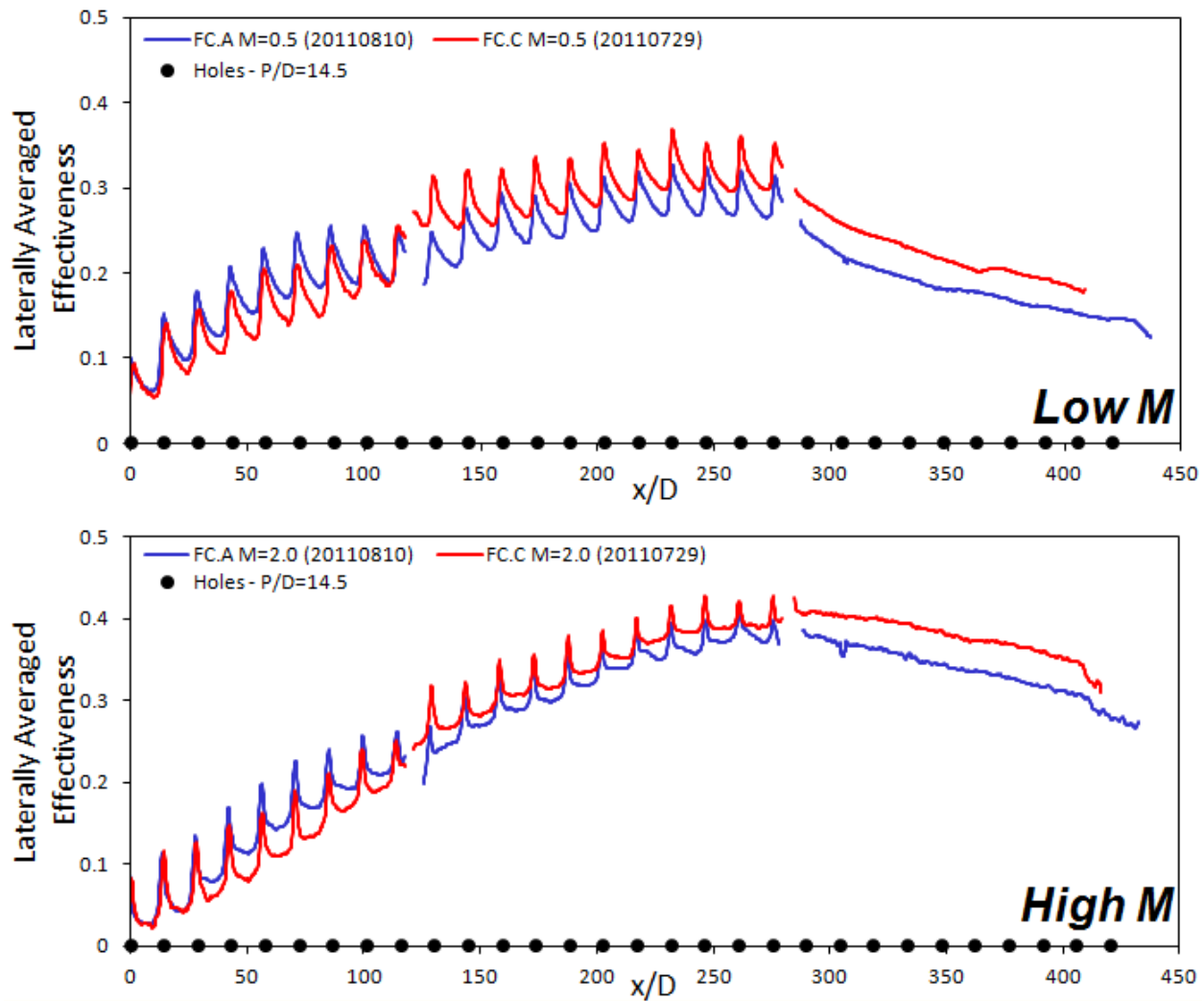
Figure 3.9: A comparison between two different hole orientations with identical hole-to-hole spacing.
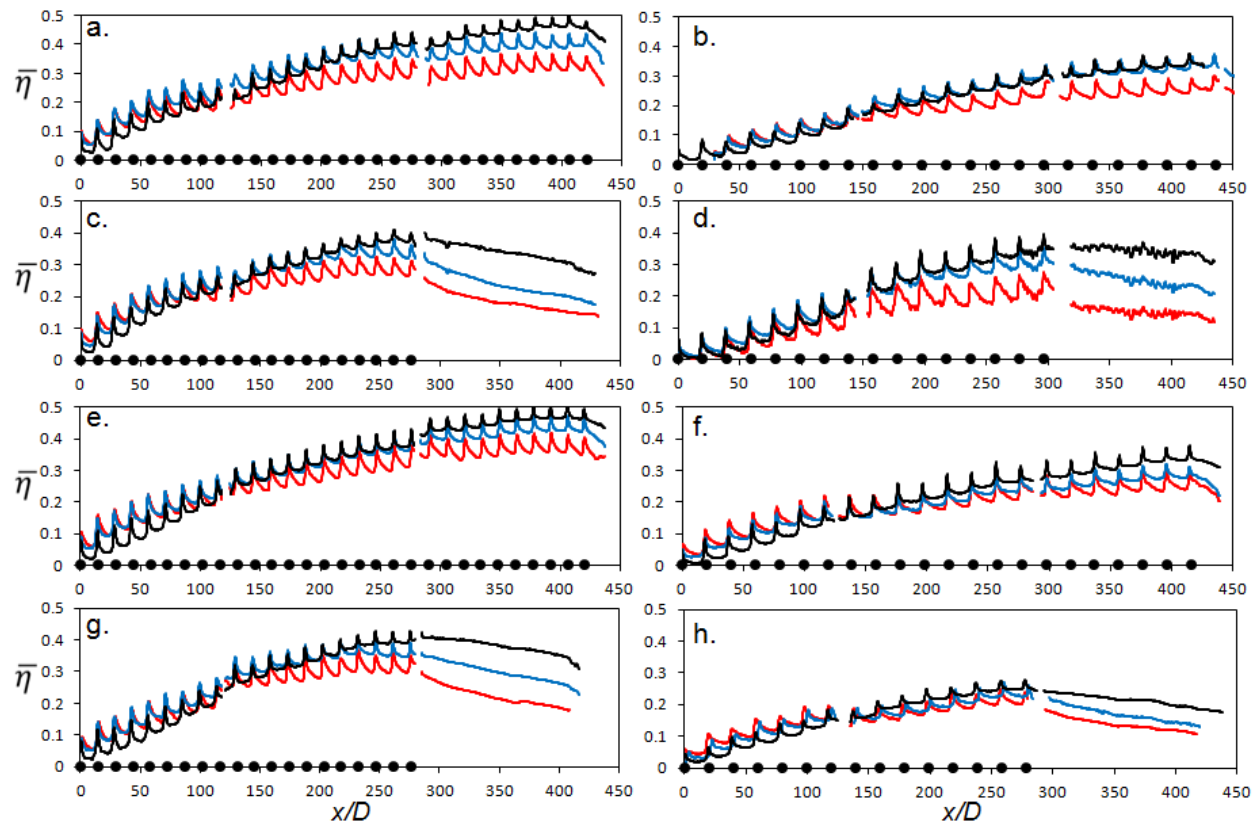
Figure 3.10: Laterally averaged adiabatic film cooling effectiveness, $\bar{\eta}$ for all geometries, all blowing ratio, full array and recovery region.

71

3.2.4 $X/N_x Ms$

Film cooling effectiveness resulting from is single row is known to scale with Ms, the blowing ratio multiplied by the equivalent slot width of the film row. In the case of multi-row film cooling, however, this simple scaling holds no meaning due to the several rows of film holes as seen in Figure 3.11. Due to the discontinuous injection it is necessary to do some sort of piecewise manipulation in order to make sense of the profile.

Figure 3.11: A failed attempt at scaling the full-coverage data. Note the first row scales nicely.

The streamwise, x-axis, is given several new origins at each row exit breakout. In this way the streamwise coordinate always is zero at a row center. This manipulation alone

does not make the data collapse. Next, the row number is included so that the buildup of coolant may be accounted for. To do this the $x - coordinate$ is scaled by $N_x M s$, with M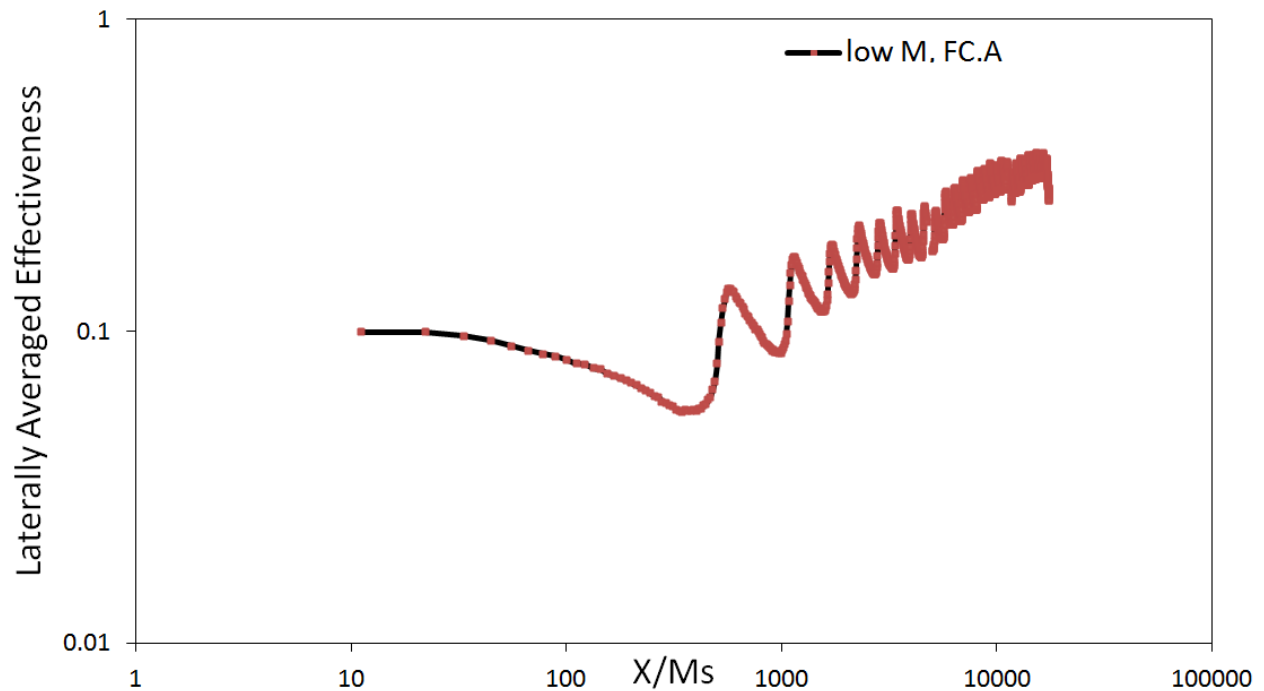 and s being the calculated values (as opposed to nominal). This alone shifts further rows to the left, however, the further profiles remain above the first row, indicating the downstream rows are more effective. To bring all the rows to collapse with the first row, the laterally averaged effectiveness is scaled to be $\bar{\eta}/N_x^{\frac{n}{2}}$. This scaling reduces takes into account the effect of upstream injection on downstream effectiveness. This entire scaling procedure applied to FC.A, $M = 0.4$ (nominal $M = 0.5$), $\eta = 0.65$ is shown below in Figure 3.12.
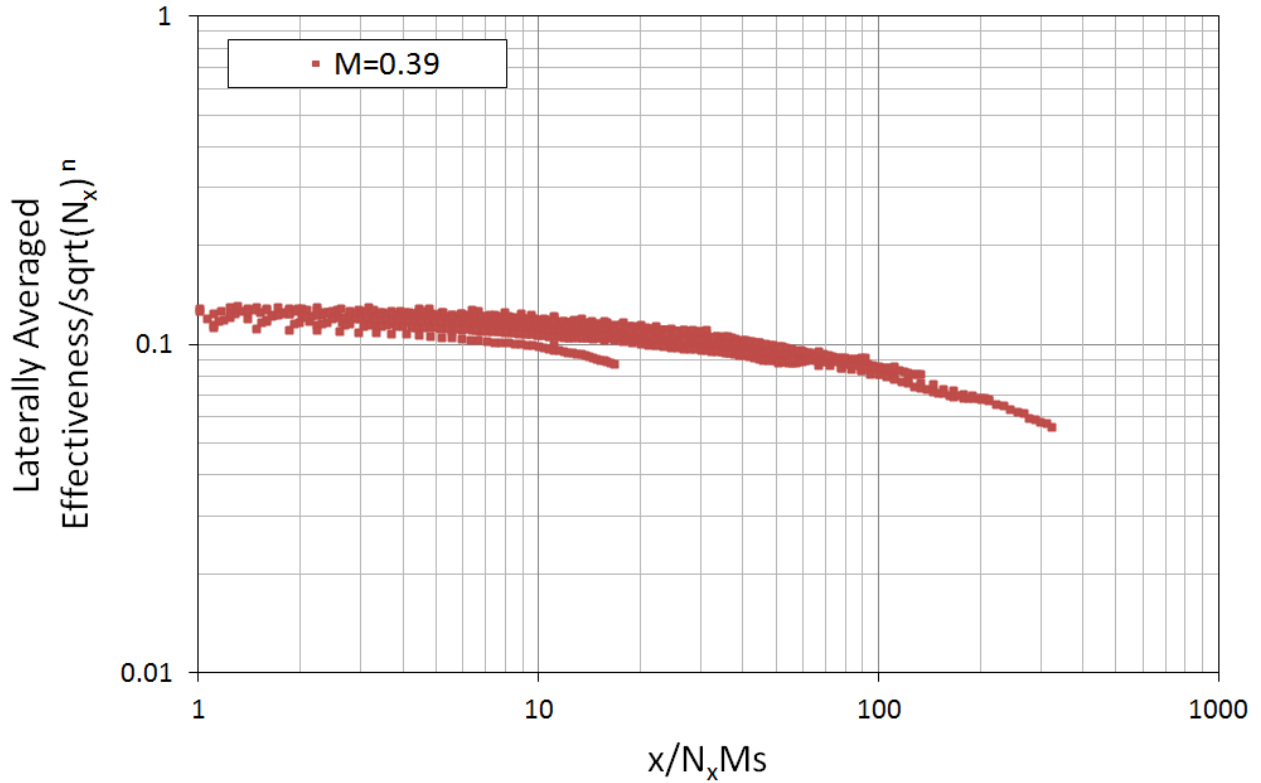
Figure 3.12: A successful attempt at scaling the full-coverage data. Includes row number to account for the apparent added efficiency of downstream rows.

It would appear from the $M = 0.5$ case that scaling of full-coverage film cooling effectiveness works very well. When applying this procedure to the remaining blowing ratios, the scaling process does not consistently collapse the data. Figure 3.13 shows all blowing ratios from FC.A with values of n being $0.65, 0.58, 0.85, 0.96, 1.3$ from low blowing to high blowing. This scaling procedure does not collapse all blowing ratios and individual blowing ratios are separate from one another. This scaling approach may be applicable to low blowing cases which are well attached.

Figure 3.13: All different blowing ratios scaled; $\frac{\bar{\eta}}{N_x^{\frac{n}{2}}}$ vs. $\frac{x}{N_x Ms}$. $n = 0.65, 0.58, 0.85, 0.96, 1.3$ from low to high M.

3.3 Observations

Local adiabatic film cooling effectiveness has been quantified throughout four compound angle, cylindrical hole, multi-row film cooling arrays. The effect of blowing ratio is investigated throughout the four arrays of different hole spacings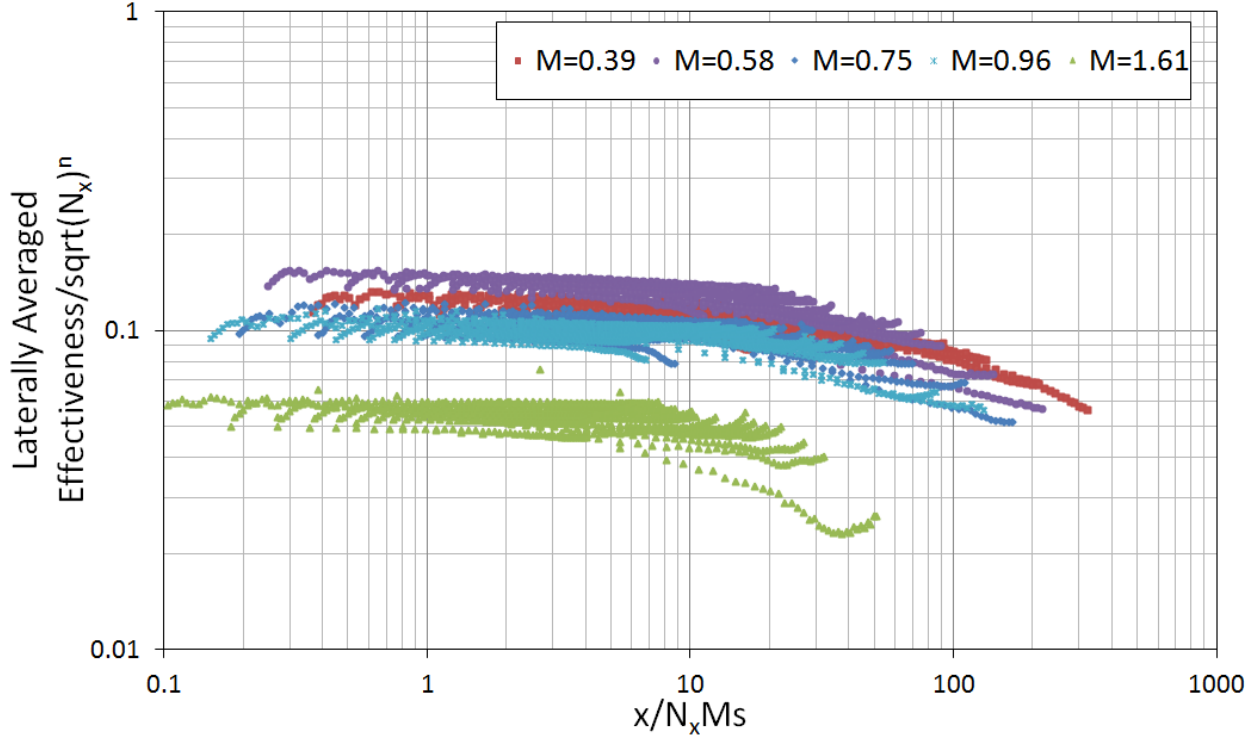 and inclination angles. It is seen that blowing ratio and hole spacing are of first order effect on adiabatic film cooling effectiveness while the inclination angle is of second order impact.

The physics of the film is unaffected by a change in hole spacing at these, already large, spacings; i.e. the coolant is not spent more or less efficiently due to a change in spacing. While the inclination angle has local effects, once laterally averaged over several rows, these effects wash out and are indistinguishable while considering experimental uncertainty.

The recovery region of the film behaves differently for different blowing ratios. In a fully attached film, the recovery region decays exponentially. In a lifted film, the decay has a concave down profile, indicating competing effects of dissipation and reattachment. This is characteristic of the entire array, not just the recovery region. Overall, compound angle arrays are capable of providing significant levels of laterally averaged effectiveness after several rows, even at the large spacing of $P/D = X/D = 19.8$.

An interesting feature of the runs with a recovery region is the behavior of the decay in the recovery region. Looking at all of the recovery regions, there are consistent trends with blowing ratio. At low blowing, $M = 0.5$, the decay of the film is exponential. At moderate blowing, the decay is almost linear. At high blowing, the decay rate is slightly concave down.

This behavior gives insight into the dynamics of the film in this region. The low blowing case is well attached and this is made apparent while looking at the recovery region as the behavior is that of a pure decay. At the high blowing rate, the film is competing between decay and reattachment. This recovery region profile is further indication that the jets which lifted upstream are returning to the cooled wall, even several pitches downstream.

Contrary to previous reports, Kasagi et al. [23] and Metzger et al. [16], the film cooling effectiveness is seen to increase with increasing blowing ratio and no optimum in the range studied is found. This is likely do to the extent (20-30 rows) of the array. In the first section of the array (comparable to the previous studies' entire array) the high blowing cases indeed provide less cooling than the lower blowing cases. However, by the end of the current studies array, these lifted jets return to the surface and provide greater cooling levels than the low blowing cases.

3.4 Suggestion for Future Work

The surface data can only provide a small glimpse into the physics throughout this full-coverage array. To confirm the mechanism behind the surface data, flow measurements throughout these very large spaced geometries is of interest. Specifically in the recovery region to confirm the reason for the seemingly very different dynamics as blowing ratio is varied.

CHAPTER 4
HEAT TRANSFER AUGMENTATION

4.1   Energy Balance

A 1-D control volume is placed over the heaters for analysis of the heat transfer data as seen in Figure 4.1. Each term from this energy balance is discussed in detail throughout the following sections.
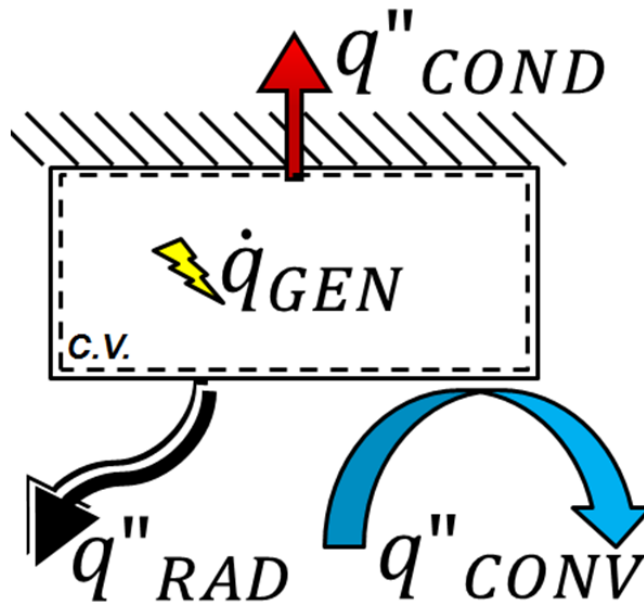

Figure 4.1: 1-D Energy Balance Diagram.

4.1.1 Joule Heating

The input heat flux, $(q_{gen}^{"})$, is calculated from the electrical current (i) and heater resistance (R) using Equation4.1, where A_s represents the surface area of the heater exposed to the mainstream flow.

$$q_{gen}^{"} = \frac{i^2 R}{A_S} = \frac{i^2 R}{lw} \tag{4.1}$$

The heater resistance is calculated using the resistivity (ρ_{el}) of stainless steel and the dimensions of the heater, as seen in Equation 4.2. The length (l) is measured in the span direction while the width (w) is measured in the stream direction. The thickness (t) is the thickness of the stainless steel foil, measured in the wall normal direction.

$$R = \frac{\rho_{el} l}{tw} \tag{4.2}$$

Thus Equation 4.1 reduces to

$$q_{gen}^{"} = \frac{i^2 \rho_{el}}{tw^2} \tag{4.3}$$

4.1.2 Heat Loss

Necessary for determining the heat transfer coefficient are the other modes of heat transfer from the surface. Heat loss is correlated experimentally to determine what portion of $q_{gen}^{"}$ is lost to conduction and radiation, the remaining heat is taken to be convected away by the flow.

4.1.2.1 Conduction Heat Loss

Conduction loss (q''_{cond}) is quantified as a function of the temperature difference between the wall temperature (T_w) and the average backside acrylic temperature (T_b). This also accounts for the heat radiated through the back surface. A schematic of this test setup is shown in Figure 4.2.
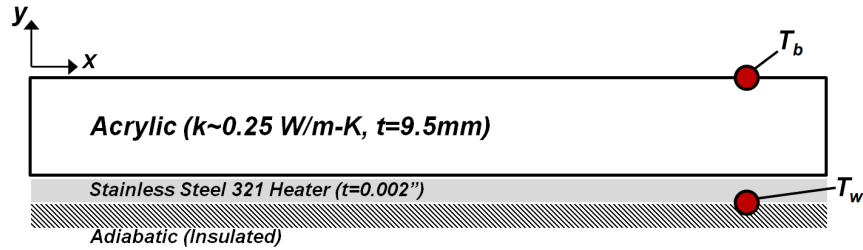
Figure 4.2: Experimental setup for conduction heat loss testing.

Figure 4.4 shows the result of the conduction heat loss test. The resulting relationship between T_w and q''_{cond} is described by Equation 4.4. Note that this loss is applied locally, as described in the 1-D heat loss correction section. The measured T_w profile and average T_b are easily combined to determine the q''_{cond} at each pixel of captured data.

$$q''_{cond} = 18(T_w(x, z) - T_b) \tag{4.4}$$

4.1.2.2 Radiation Heat Loss

Heat lost by radiation to the environment (q''_{rad}) is also quantified through a separate experiment. This is achieved by insulating the backside of an acrylic plate and sealing the mainstream flow tunnel to reduce natural convection. A foil heater, coated with *TSP*, is attached to the acrylic plate to reproduce the conditions of a heat transfer experiment.

The results of this test, seen in Figure 4.4, show that the heater surface can be approximated as a grey body with emissivity of $\epsilon = 0.873$. The results of this experiment are in agreement with estimates of radiation loss based on the emissivity of white paint. The radiation heat loss is therefore evaluated by Equation 4.5, where σ is the Stephan-Boltzmann constant.

$$q''_{rad} = 0.873\sigma(T_w^4 - T_\infty^4) \qquad (4.5)$$

4.1.2.3 1-D Heat Loss Correction

These loss corrections are applied to the energy balance in a 1-D manner. This energy balance assumes adiabatic planes are separating each pixel. In other words, heat flows entirely in the y-direction from the heater through the double-sided Kapton tape and acrylic. See Figure 4.5 for a diagram detailing the difference between isothermal and adiabatic planes. Figure 4.6 shows that this assumption is more accurate at predicting the local conductive heat flux than an assumption of isothermal planes.
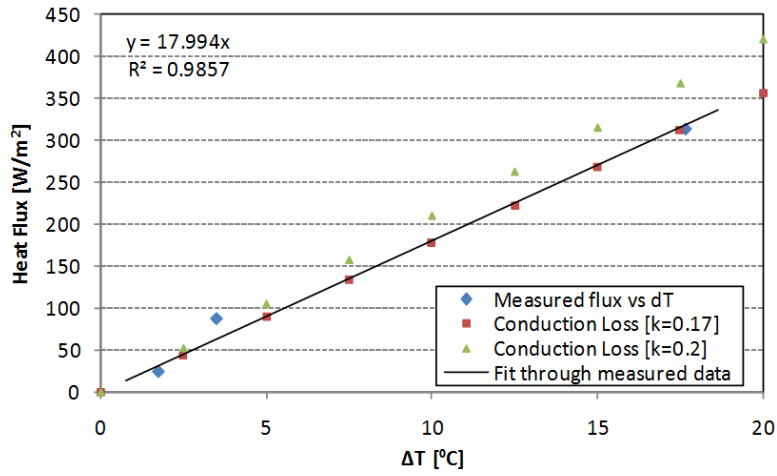
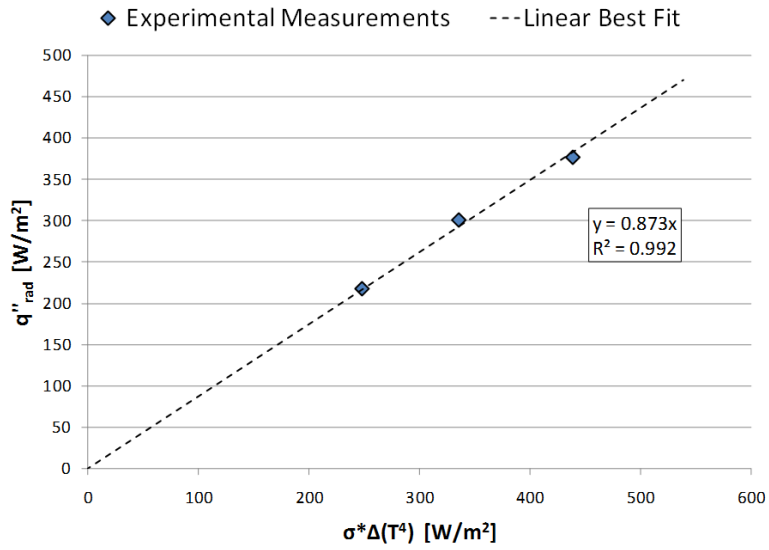Figure 4.3: Conduction heat loss data.

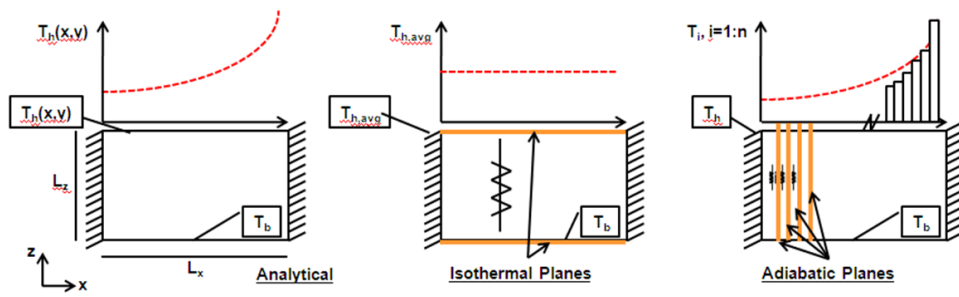Figure 4.4: Radiation heat loss data.

Figure 4.5: Diagram of the three different scenarios for heat loss; Exact, Isothermal planes, Adiabatic planes.
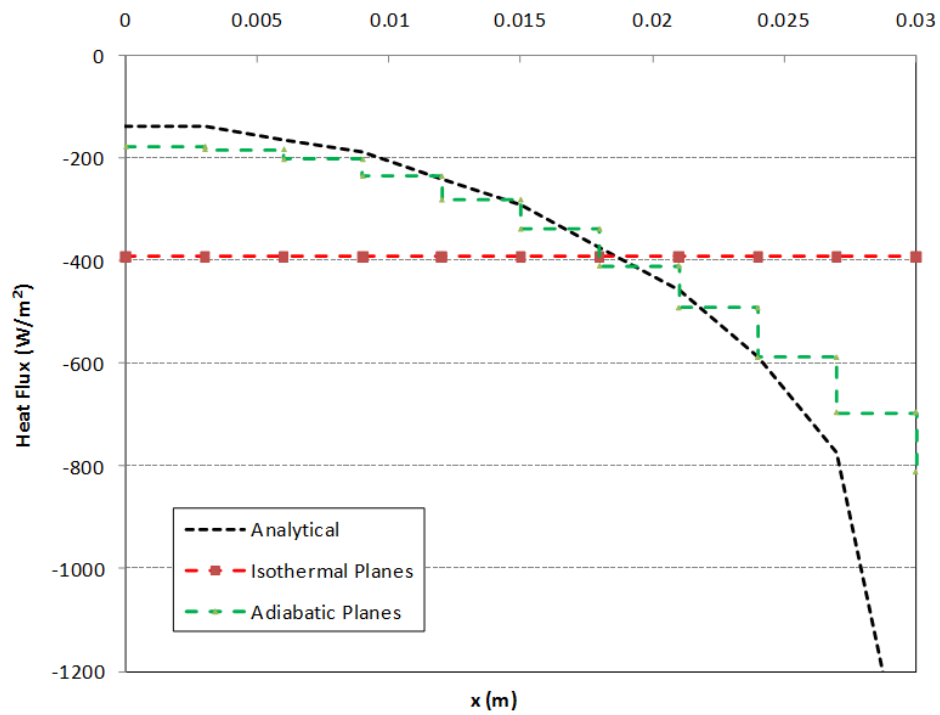

Figure 4.6: Comparison of different 1D data reduction methods (Isothermal planes, Adiabatic planes) with exact 2D solution.

4.1.3 Heat Transfer Coefficient Corrected for Film Temperature

Using this information, the local uncorrected heat transfer coefficient is calculated by Equation 4.6, where $q_{conv}^{''}$ is determined by Equation 4.7.

$$h_u = \frac{q_{conv}^{''}(x, z)}{T_w(x, z) - T_\infty} \tag{4.6}$$

$$q_{conv}^{''} = q_{gen}^{''} - q_{cond}^{''} - q_{rad}^{''} \tag{4.7}$$

Note that this heat transfer coefficient is uncorrected because it is determined using the mainstream flow temperature, which differs from the coolant temperature by $2 - 10°C$. Once evaluated, the local effectiveness data is used with Equation 4.8 to account for this difference.

$$h_f = h_u(1 - \eta\theta)^{-1}, \qquad where \quad \theta = (T_\infty - T_c)/(T_\infty - T_w) \tag{4.8}$$

4.2 Predicting Baseline Heat Transfer Coefficient

Additionally, the heat transfer data is more useful when presented as heat transfer enhancement, h/h_0, where h_0 is the flat plate heat transfer coefficient in the absence of film cooling. h_0 is determined analytically so that numerous heater geometries may be accounted for with a single equation. This analytical result is validated with a flat plate with various heated and unheated portions. A comparison between experiment and prediction is shown in §4.3.1 .

Equation 4.10, the unheated starting length equation for turbulent flow over a flat plate, is used to superimpose the effect of multiple constant heat flux surfaces and adiabatic surfaces to simulate the alternating thermal boundary conditions on the test surface. The series representing the superposition is shown in Equation 4.12. Figure 4.7 describes the heated and unheated surface conditions.

The following equations are used to evaluate h_0:

Nusselt number correlation for turbulent flow over a flat plate with a thermal boundary condition of constant heat flux;

$$Nu_{x'} = 0.0308 Re_{x'}^{(4/5)} Pr^{(1/3)} \tag{4.9}$$

Unheated starting length formula for a turbulent flow;

$$Nu_{x'} = \frac{Nu_{x'}\big|_{\xi=0}}{\left[1 - (\xi/x')^{9/10}\right]^{1/9}} \tag{4.10}$$

A shift relating the FCFC coordinate system to the boundary layer coordinate system;

$$x = x' - x_0 \tag{4.11}$$

Superposition of unheated starting lengths to account for the segmented heaters;

$$Nu_{x'} = \sum_{m=1}^{i} \frac{(-1)^{m-1} Nu_{x'}\big|_{\xi=0}}{\left[1 - (\xi_m/x')^{9/10}\right]^{1/9}}, \qquad for \quad \xi_{i-1} \leq x' < \xi_i \tag{4.12}$$

From the definition of Nusselt number, the correlations yields the following for h_0;

$$h_0 = \frac{Nu_x k_f}{x} \tag{4.13}$$

Finally the heat transfer data is represented as an augmentation factor.

$$h/h_0 = \frac{h_f}{h_0} \qquad (4.14)$$

4.3   Results Heat Transfer Augmentation

4.3.1   Film Cooling Heat Transfer Validation

The method of measuring heat transfer coefficient is validated in two ways: first, the method of determining h_0 is tested using a flat plate with alternating heated and adiabatic portions. The results of this, seen in Figure 4.8, show the measured heat transfer coefficients to be in good agreement to the h_0 prediction. This experiment also validates the method of calculating the heat transfer coefficient based on the electrical power input to the heaters.

Additionally, a film cooling geometry identical to the geometry used by Mayle [15], named FC1, is tested. The heat transfer enhancement results for FC1 are compared directly to this data and show good agreement, within the measurement uncertainty of the experiment. A comparison of Mayle's and current data for $M = 0.5, 1.0$ and 1.5 is shown in Figures 4.9-4.11.
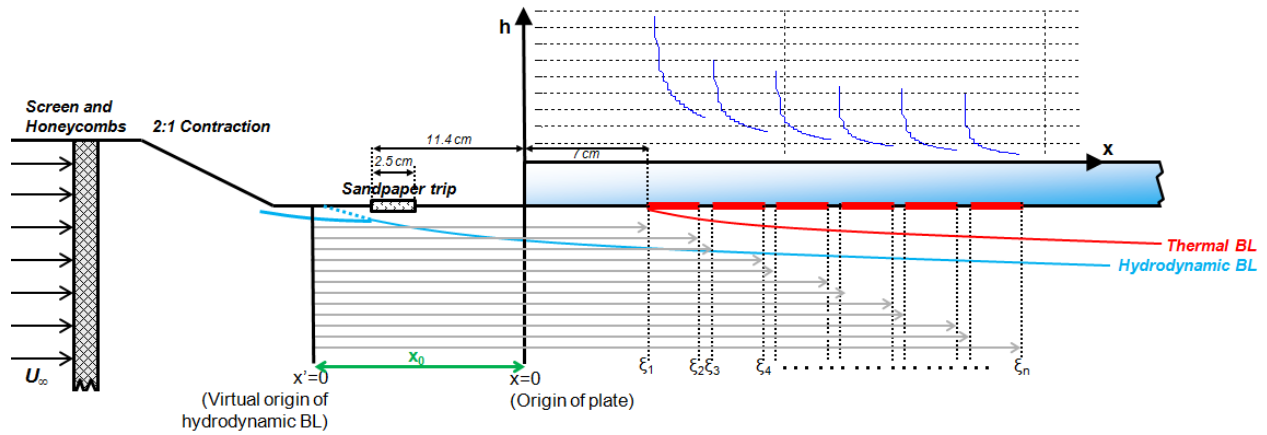
Figure 4.7: Diagram of the flat plate heat transfer scenario in current wind tunnel.
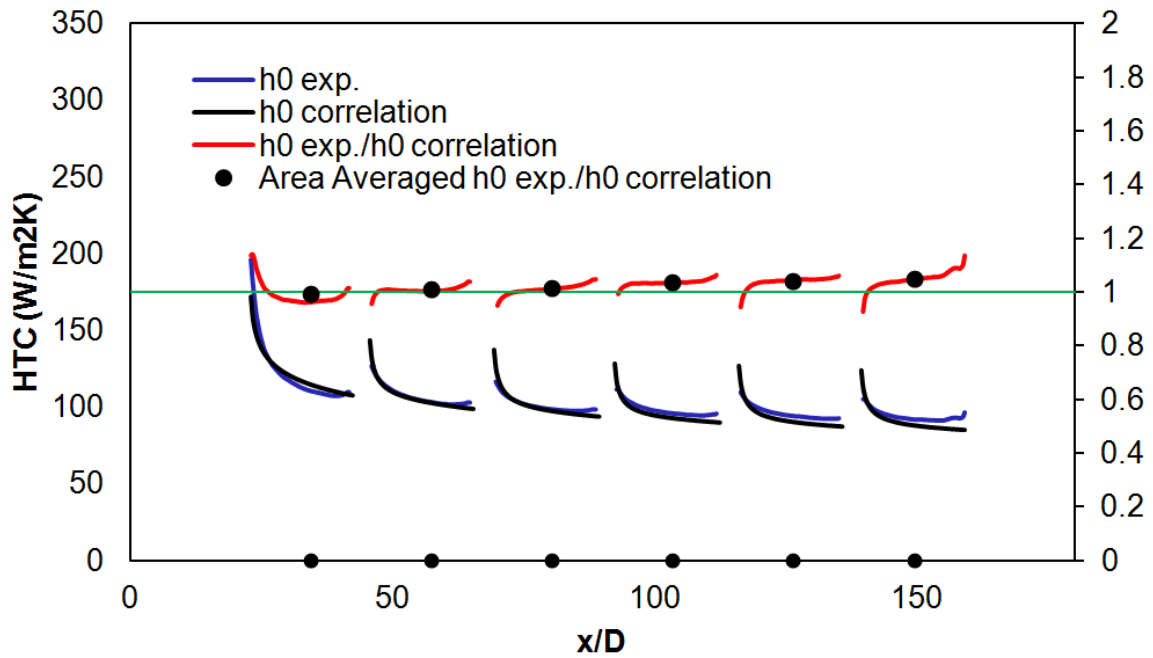

Figure 4.8: Comparison of experimental h_0 with correlation.
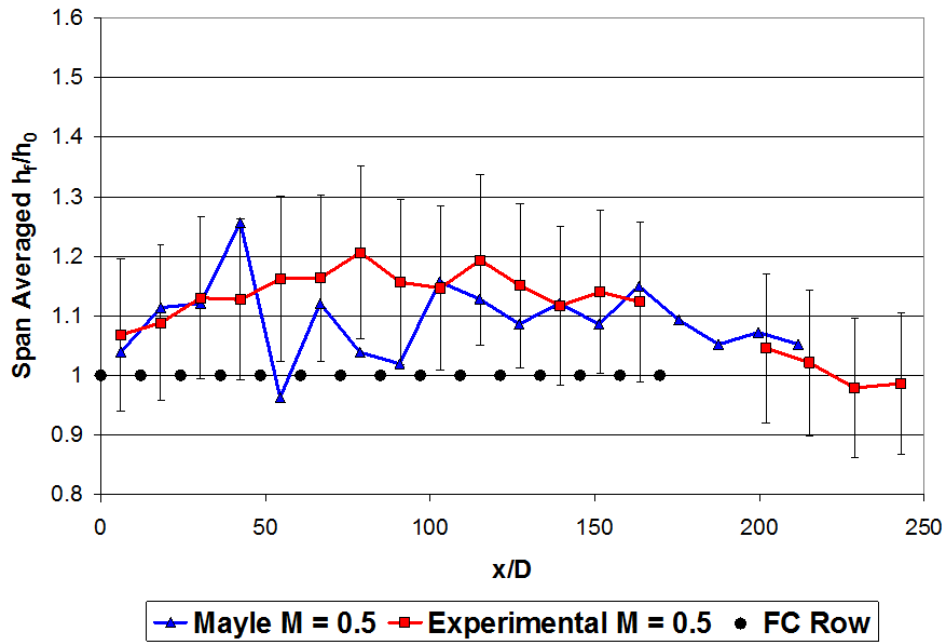
Figure 4.9: Comparison with Mayle and Camarata at blowing ratio $M = 0.50$.
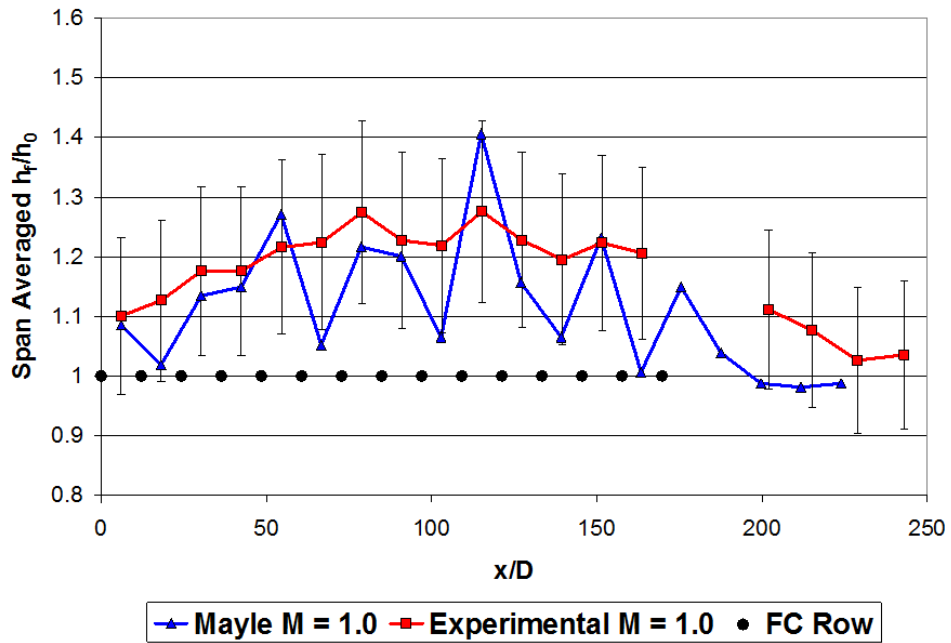
Figure 4.10: Comparison with Mayle and Camarata at blowing ratio $M = 1.00$.

4.3.2 Film Cooling Heat Transfer Augmentation

Local heat transfer enhancement distributions, seen in Figure 4.12, show augmentation levels near one at the leading edge region. Heat transfer enhancement levels on the first row are close to unity in the between hole regions with 20% augmentation directly downstream of the hole locations. On the low blowing rate case, the augmentation levels rise downstream of the holes with the between hole regions having augmentation levels of less than 10%. The jets bring in momentum to the boundary layer; on the first few rows, this momentum is enough to increase the heat transfer directly downstream of the jet; the augmentation levels increase laterally in the downstream direction due to spreading of the jet as it moves downstream. The high blowing case has noticeably lower heat transfer augmentation factors than its counterparts at low x/D due to the jets lifting off from the surface; this coolant will then reattach downstream creating higher augmentation levels.

Heat transfer enhancement distributions are area averaged over single pitches to yield pitch-averaged h/h_0; the results are shown in Figure 4.13 through Figure 4.16. FC.A has the highest heat transfer augmentation factors with values reaching 40%. FC.B, FC.C and FC.D follow with values reaching 30% augmentation. Heat transfer augmentation is higher for the higher blowing ratios at high x/D. Augmentation levels rise and level off within the first five rows for all arrays. Variations in heat transfer augmentation factors as a function of blowing ratio is higher for the $\alpha = 30°$ cases. This may be due to the exiting jets ability to stay close to the wall at low blowing ratio and possible liftoff at higher blowing rates. The liftoff of the jets at high blowing rates is evident for cases FC.C and FC.D. The difference in augmentation values at low x/D for two different blowing rates is small. The difference is increases as x/D increases due to the jets reattaching to the surface. The increase of pitch decreases the augmentation level for the $\alpha = 30°$ case (FC.A); however, the only difference it has on the $\alpha = 45°$ case (FC.C) is a slower increase in enhancement in the streamwise direction.

Recovery region data, Figure 4.17 through Figure 4.20, shows similar trends to those found in the full geometries with a decrease in heat transfer augmentation in the recovery region. The decay seen on the recovery region has a concave upward profile meaning the heat transfer augmentation rapidly decays after the last row of coolant injection and decays to a value of unity slowly thereafter. The rate of decrease in heat transfer augmentation does not seem to vary with changing blowing ratio, only their magnitudes are different.
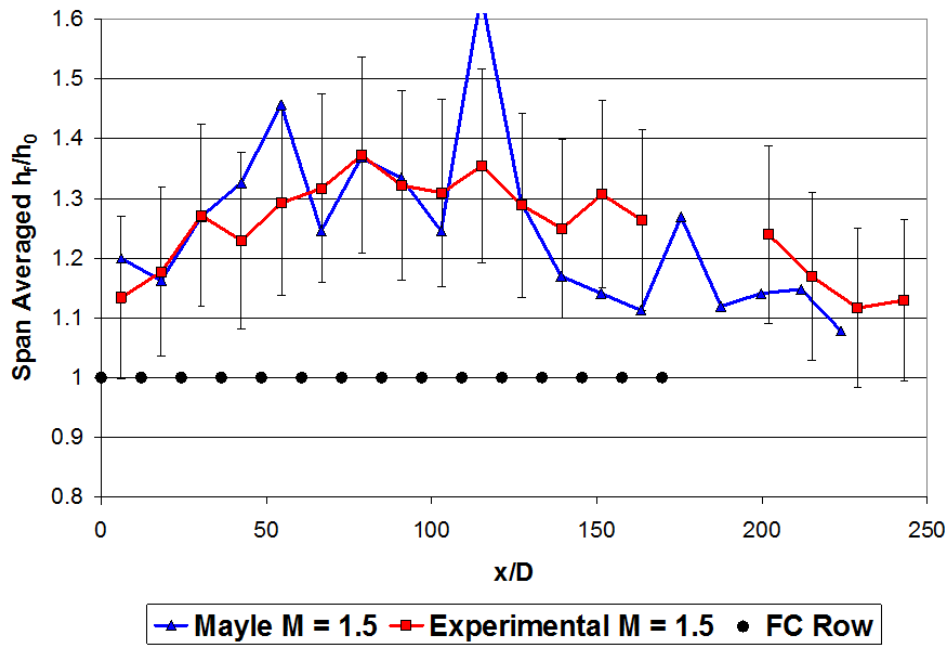
Figure 4.11: Comparison with Mayle and Camarata at blowing ratio $M = 1.50$.
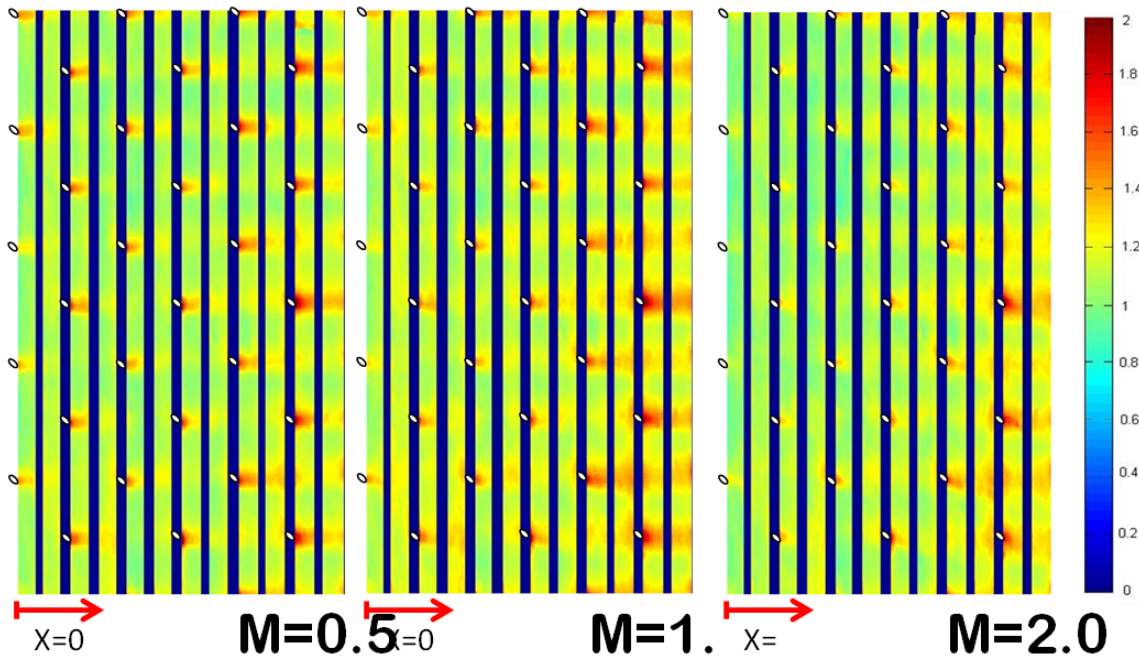
Figure 4.12: Local heat transfer augmentation.
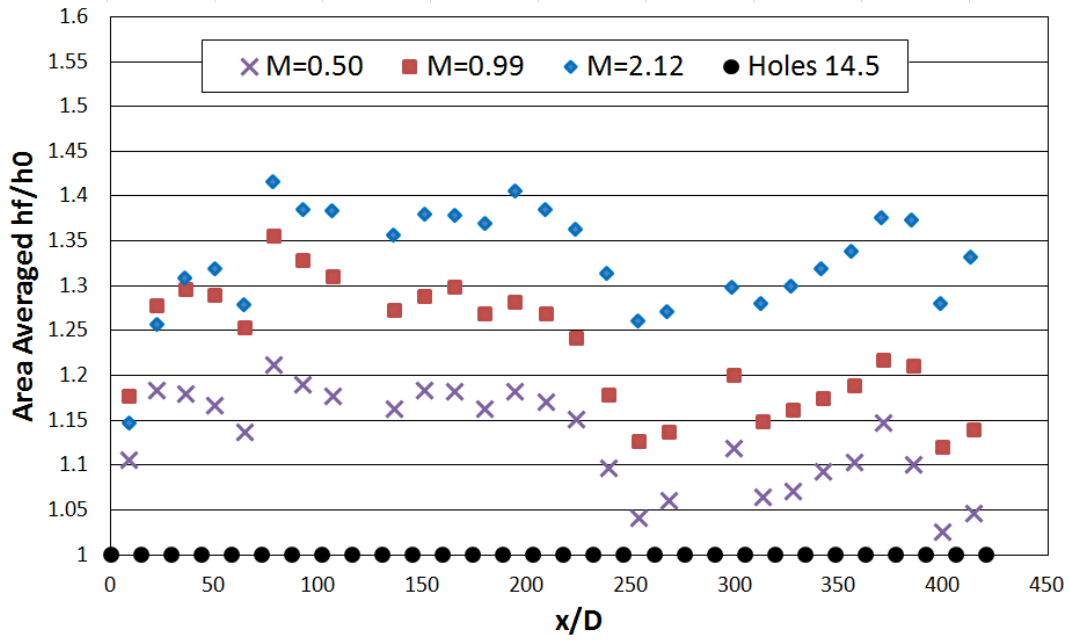
Figure 4.13: FC.A pitch averaged heat transfer augmentation.
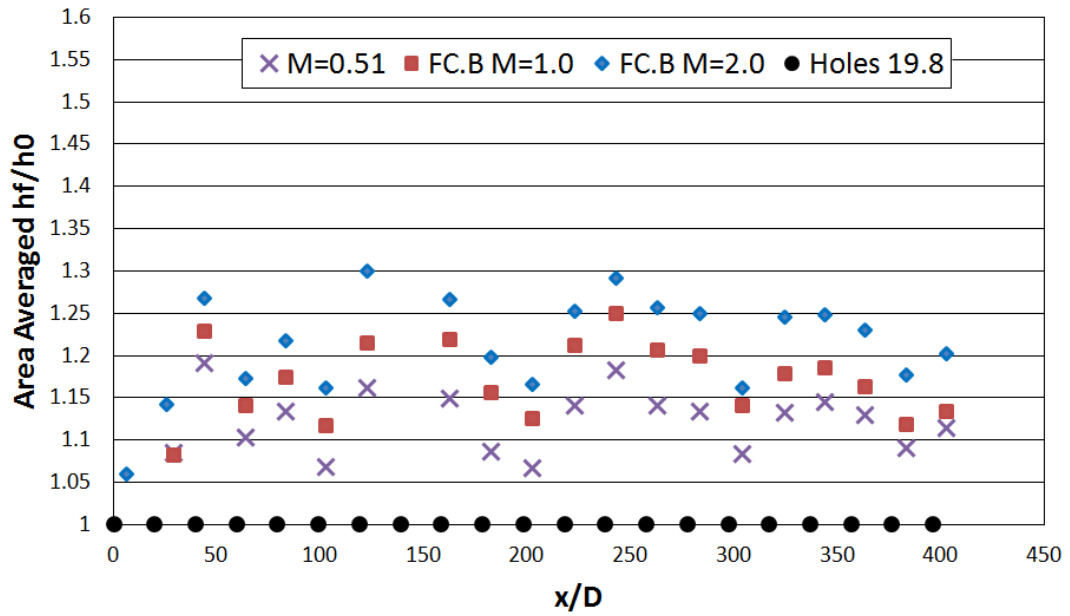
Figure 4.14: FC.B pitch averaged heat transfer augmentation.

91
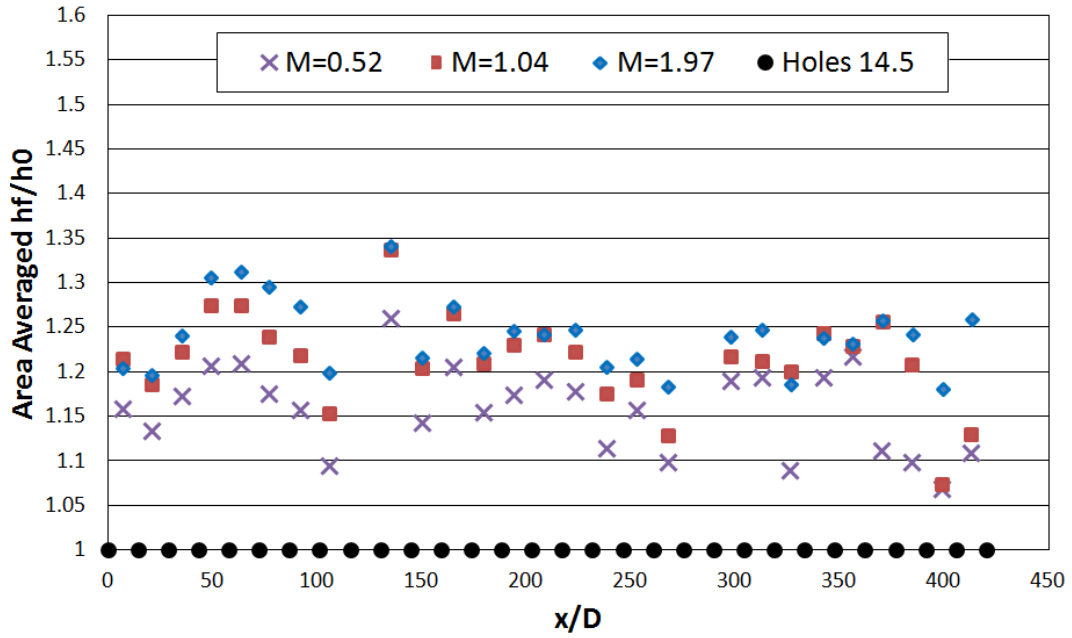
Figure 4.15: FC.C pitch averaged heat transfer augmentation.
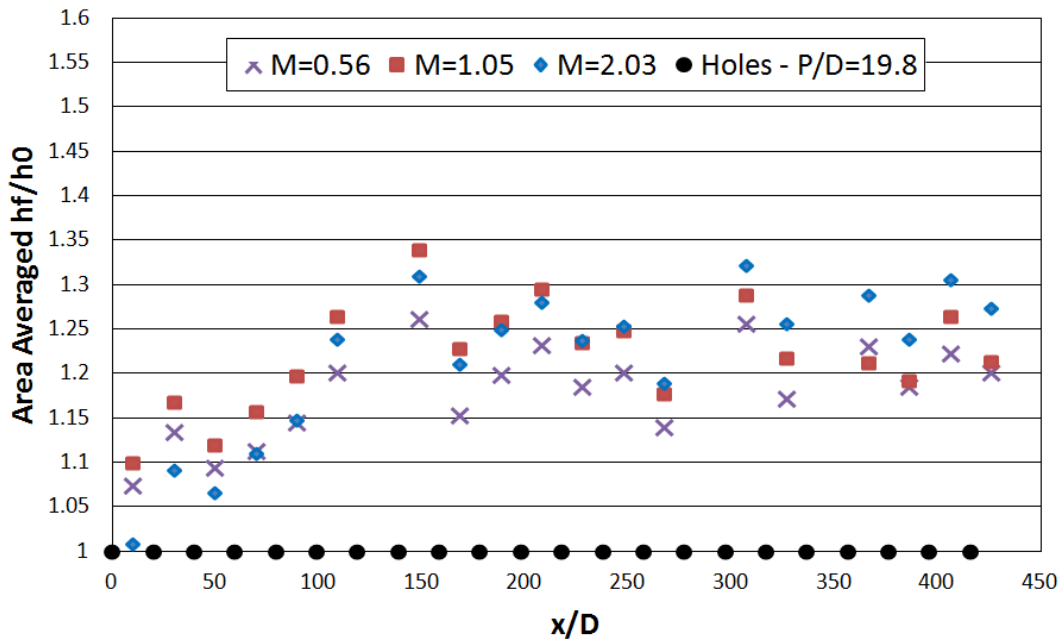
Figure 4.16: FC.D pitch averaged heat transfer augmentation.
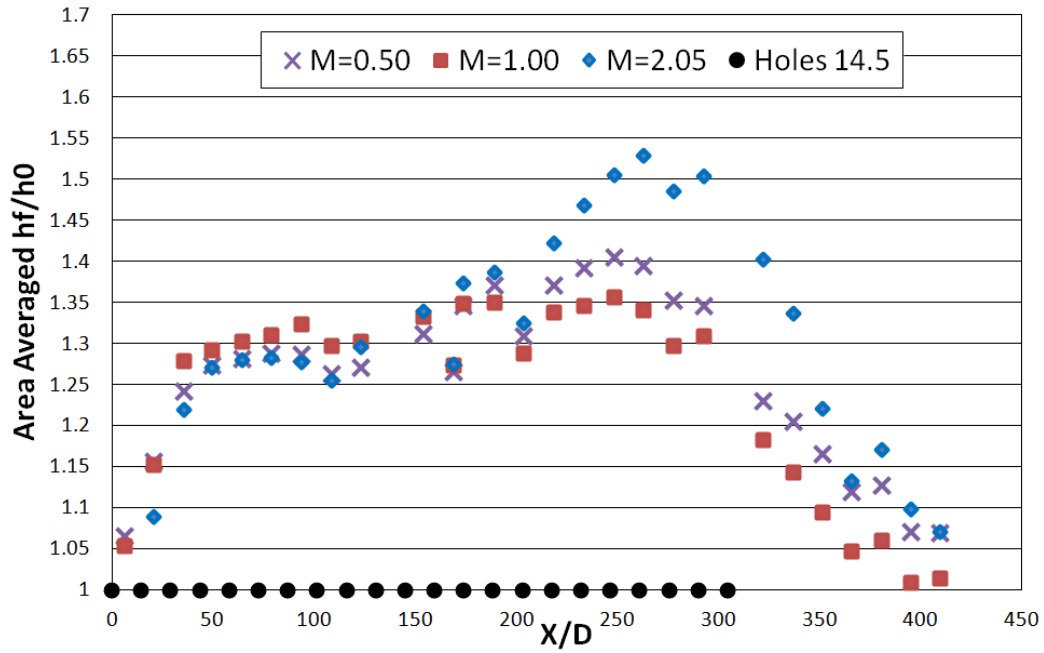
Figure 4.17: FC.A pitch averaged heat transfer augmentation with recovery region.
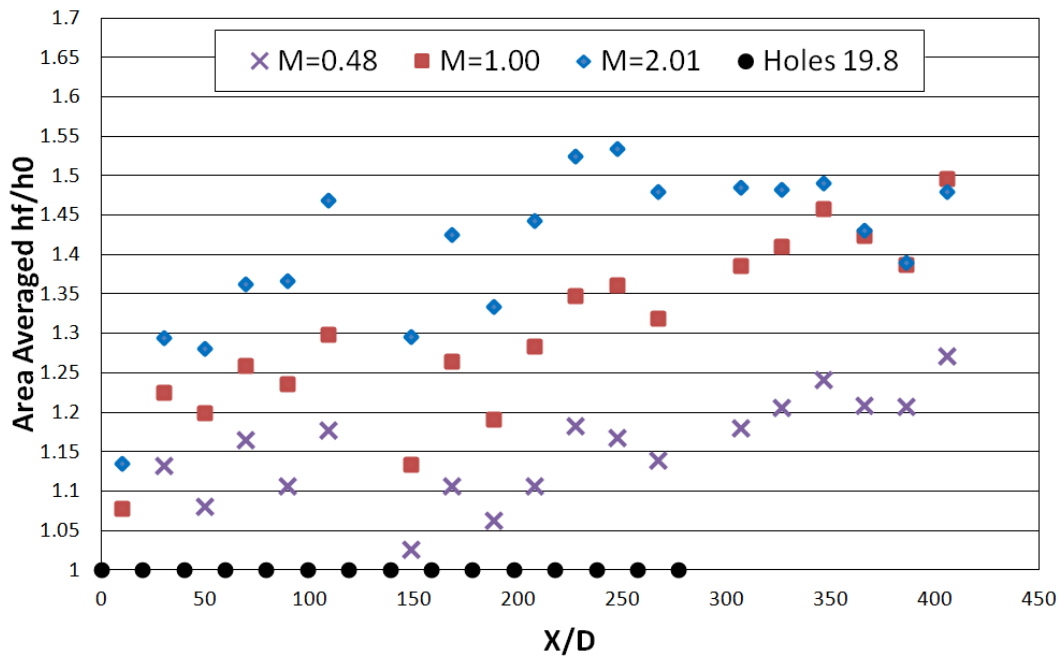
Figure 4.18: FC.B pitch averaged heat transfer augmentation with recovery region.
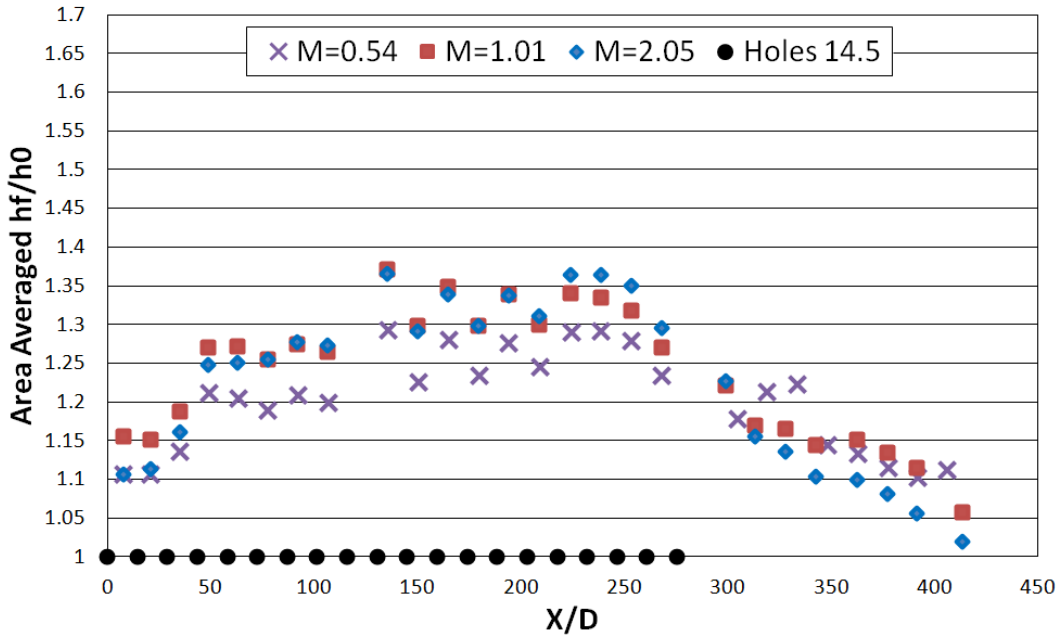
Figure 4.19: FC.C pitch averaged heat transfer augmentation with recovery region.
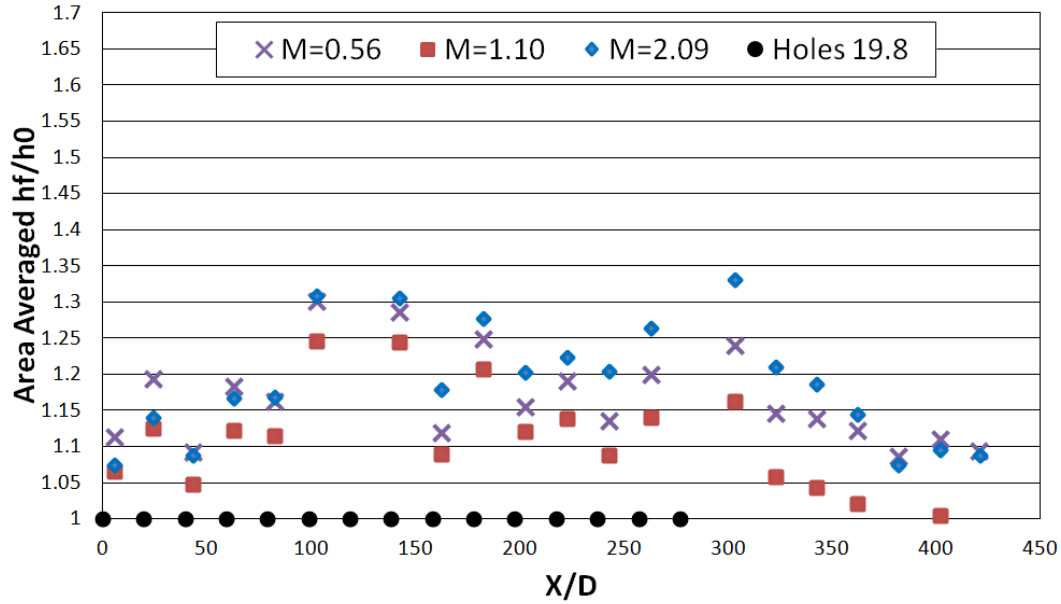
Figure 4.20: FC.D pitch averaged heat transfer augmentation with recovery region.

94

Figure 4.21 shows the same data seen in Figure 4.20 with the addition of error bars. Even though differences in enhancement values with varying blowing ratio are seen in different cases, with 14% error in heat transfer values, the differences in heat transfer augmentation between blowing ratios is statistically insignificant; i.e. h/h_0 is approximately invariant with respect to blowing ratio M. Although the error bars go in some cases to values less than one, the bulk of them lie above $h/h_0 = 1.0$ and range between $h/h_0 = 1.0$ and 1.5.
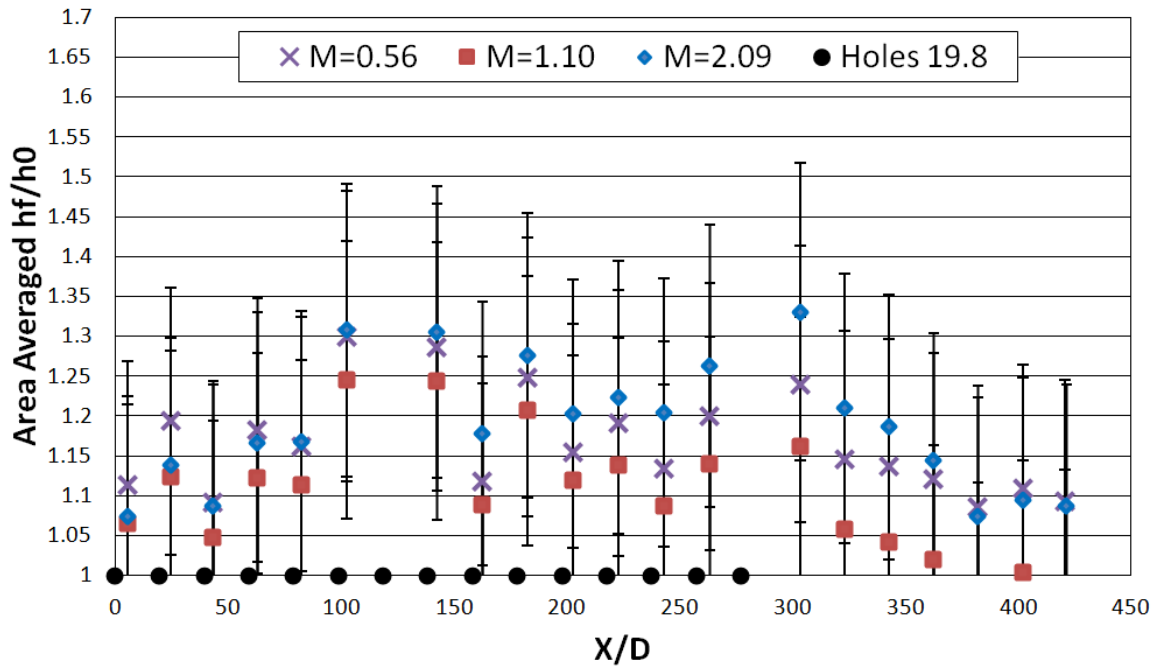
Figure 4.21: Error bars for FC.D pitch averaged h/h_0 with recovery region.

4.4   Observations

Heat transfer augmentation has been quantified for four different full-coverage film cooling arrays. The effect of blowing ratio, M, on the arrays is seen to be a second-order effect on the enhancement factors, h/h_0. The hole spacing is also a second-order effect while at these large spacings. While the inclination angle has local effects, once laterally averaged over several rows, these effects wash out and are indistinguishable while considering experimental uncertainty.

All the arrays enhancement factors are seen to level off to within uncertainty after 5 or 6 rows implying the fact that once certain number of rows are used, additional rows will not suffer from higher heat transfer augmentation values than previous ones. Overall, the higher spacing produced the lowest heat transfer augmentation factors while providing significant amount of coolant coverage throughout the surface. The effect of inclination angle is minimal at the large array spacing.

The experimental uncertainty must be driven down to resolve these small differences. If the range of hole spacings and hole orientations were larger, a difference would be clear.

NOTE: Recent studies of h/h_0 have been much more successful in obtaining high quality heat transfer augmentation data. The primary difference between the two sets of testing can be attributed to test section preparation.

CHAPTER 5
NUMERICAL SIMULATIONS

For engineering predictions of turbulent flows a fast, efficient, accurate solution is desirable. Hence the wide use of two equation closure models in current practice. Presently, two of these models are scrutinized in the context of predicting full-coverage film cooling. The models chosen for this comparison in particular solve a time averaged version of the governing equations and implement an eddy viscosity concept, thereby assuming isotropy in the turbulence.

5.1   Turbulence Modeling

5.1.1   Eddy Viscosity

The six Reynolds stresses arising for Reynolds Averaging the governing equations are assumed to be proportional to the local velocity gradient. The constant of proportionality is defined as the turbulent viscosity and is a property of the flow,, and hence, varies in space.

$$\nu_T(x_i, t) \equiv \frac{-\langle u_i u_j \rangle}{\dfrac{\partial u_i}{\partial x_j}} \tag{5.1}$$

5.1.2 Realizable $k - \varepsilon$

The realizable $k - \varepsilon$ (RKE) model is very well established method for modeling turbulent flows. The turbulent viscosity concept is introduced into the RANS equations and a relation between ν_T, k and ε is established. Transport equations for the turbulent kinetic energy $(k, m^2/s^2)$ and turbulence dissipation rate $(\varepsilon, m^2/s)$ are formulated which are solved along with the equations for mass, momentum and energy.

There are a total of five constants which must be specified before the equations for k and ε become tractable. The constant for the RKE model used in this study are the default coefficients available in the Fluent solver, [36].

$$\frac{\partial}{\partial t}(\rho k) + \frac{\partial}{\partial x_j}(\rho k u_j) = \frac{\partial}{\partial x_j}\left[\left(\mu + \frac{\mu_T}{\sigma_k}\right)\frac{\partial k}{\partial x_j}\right] + G_k + G_b - \rho \varepsilon - Y_M + S_k \qquad (5.2)$$

$$\frac{\partial}{\partial t}(\rho \varepsilon) + \frac{\partial}{\partial x_j}(\rho \varepsilon u_j) = \frac{\partial}{\partial x_j}\left[\left(\mu + \frac{\mu_T}{\sigma_\varepsilon}\right)\frac{\partial \varepsilon}{\partial x_j}\right] + \rho C_1 S \varepsilon - \rho C_2 \frac{\varepsilon^2}{k + \sqrt{\nu \varepsilon}} + C_{1\varepsilon}\frac{\varepsilon}{k}C_{3\varepsilon}G_b + S_\varepsilon \quad (5.3)$$

$$\nu_T = C_\mu \frac{k^2}{\varepsilon} \qquad (5.4)$$

The difference between RKE and other $k - \varepsilon$ models is that C_μ is no longer constant, it is computed from

$$C_\mu = \frac{1}{A_0 + A_S \dfrac{kU_*}{\varepsilon}} \qquad (5.5)$$

5.1.3 $k - \omega$ **Shear Stress Transport**

The $k - \omega$ model is another two-equation model which formulates the eddy viscosity as a function of k and specific dissipation rate ($\omega = \varepsilon/k$). The $k - \omega$ model is superior to any other RANS model near the wall due to the model integrating all the way to the wall, through the viscous sub-layer. However, the original $k - \omega$ model has drawbacks. In free shear flows it is very sensitive to inlet boundary conditions. The shear stress transport formulation ($SSTKW$) has benefits over the traditional $k - \omega$ model in that it switches to a $k - \varepsilon$ behaviour away from the wall. Near the wall, it still has the benefits of a traditional $k - \omega$ model yet does not have such a strong sensitivity to turbulent boundary conditions.

$$\frac{\partial k}{\partial t} + u_j \frac{\partial k}{\partial x_j} = P_k - \beta^* k\omega + \frac{\partial}{\partial x_j}\left[(\nu + \sigma_k \nu_T)\frac{\partial k}{\partial x_j}\right] \tag{5.6}$$

$$\frac{\partial \omega}{\partial t} + u_j \frac{\partial \omega}{\partial x_j} = \alpha S^2 - \beta\omega^2 + \frac{\partial}{\partial x_j}\left[(\nu + \sigma_\omega \nu_T)\frac{\partial \omega}{\partial x_j}\right] + 2(1 - F_1)\sigma_{\omega 2}\frac{1}{\omega}\frac{\partial k}{\partial x_j}\frac{\partial \omega}{\partial x_j} \tag{5.7}$$

$$\nu_T = \frac{a_1 k}{max(a_1\omega, SF_2)} \tag{5.8}$$

There are several additional relations for closure relating various coefficients which can be found in [36].

5.1.4 El-Gabry et al.

El-Gabry et al. [37]study film cooling at high blowing rates numerically. The code used solves the Reynolds Averaged Navier-Stokes equations for compressible flow using finite volume discretization that is second-order accurate in time and space. It uses the low Reynolds number $k - \omega$ model of Wilcox which integrates to the wall and therefore no wall functions are used to model the viscous sublayer. Comparisons are made with experimental measurements and the models ability to predict the behaviour of the jets is assessed. Two conclusions relevant to the current investigation are quoted below;

It may be that RANS models and steady state simulations methods are simply insufficient in capturing the physics of separated flows and the mixing that occurs between jets and in the wake of a jet.

At moderate blowing ratios, the CFD predictions are in good agreement with experimental results.

From this it can be expected that the current study will have more success in the prediction of low blowing rates and have poorer results at higher blowing.

5.1.5 Focus

The current numerical study assesses two different turbulence models, both eddy viscosity based formulations, in their ability to predict behaviour of multi-row film cooling geometries, gauged by how well the results match the present experimental data.

The test matrix is summarized in Table 5.1. One geometry is tested at two blowing ratios; FC2 (a variation of Mayle and Camarata's geometry in which the compound angle is set to $\beta = 0°$) at $M = 0.5, 2.0$. Both cases are predicted with the two models of interest, RKE and $SSTKW$. A prediction of FC2, $M = 0.5$ following 15 rows of injection into a recovery region is also predicted with the RKE model.

Table 5.1: Numerical Test Matrix - Mayle Variation

Run	Blowing Rate - M	Turbulence Model	Domain
1	0.5	RKE	30 rows
2	2.0	RKE	30 rows
3	0.5	$SSTKW$	30 rows
4	2.0	$SSTKW$	30 rows
5	0.5	RKE	15 rows + RR

5.2 Numerical Methodology

5.2.1 Assumptions

The RANS equations are solved. The fluids involved are two streams of air with constant properties (μ, C_P, thermal conductivity). The flow is assumed incompressible, (dp/p is small). In this way density varies only with the inverse of temperature by the ideal gas law and a reference pressure. For turbulence modeling/closure, a two-equation eddy viscosity model is used.

5.2.2 Turbulence Models

The focus is to assess relevant turbulence models' accuracy in the prediction of full-coverage film cooling effectiveness; hence the RKE and $SSTKW$ models are used to predict the performance of a film array, and results from both predictions are compared to assess the quality of predictions.

5.2.3 *RKE*

A two-layer enhanced wall treatment is used to resolve the viscous sub-layer. Coefficients used in the governing equations are unchanged from Fluent defaults, [36], shown in Table 5.2.

Table 5.2: Coefficients for *RKE* model default in Fluent and used in current study

$C_{2\varepsilon}$	1.9
σ_k	1.0
σ_ε	1.2
σ_E	0.85
σ_W	0.85

5.2.4 *SSTKW*

The coefficients used for the model are unchanged from Fluent defaults as shown in Table 5.3.

5.2.5   Domain and Grid

There is a cylindrical hole diameter with diameter of $D = 2.5mm$. It is parallel to the flow, inclined at 30°. The problem domain is one streamwise period $(24.2D)$, half a spanwise period $(7D)$ and a height matching the height of the experimental facility $(60D)$. Lastly, the domain includes the length of the film holes $(8D)$. The holes are centered in the streamwise direction.

The first cell height is held near $y^+ = 1$ over the heat transfer surface. The grid used is highly structured and composed of hexahedral cells, constructed in Gambit, [38]. The meshing methodology is to mesh edges with proper expansion ratios, focusing resolution towards regions of large gradients in velocity and temperature, specifically the near wake region. The edge meshes were then mapped to faces which were extruded through the volumes. The final cell count is $\approx 900,000$ cells. $300,000$ compose the lower $10Y/D$ of the domain. The remainder are simply placeholders for continuity in order to prevent acceleration of the mainstream.

5.2.6   Boundary Conditions

A succinct description of all boundary conditions is shown in Table 5.4. The bottom wall is the surface being cooled; it is specified as adiabatic, no-slip and impermeable. The face composing the hole length is specified as an adiabatic, no-slip impermeable wall as well.

Table 5.3: Coefficients for $SSTKW$ model default in Fluent and used in current study

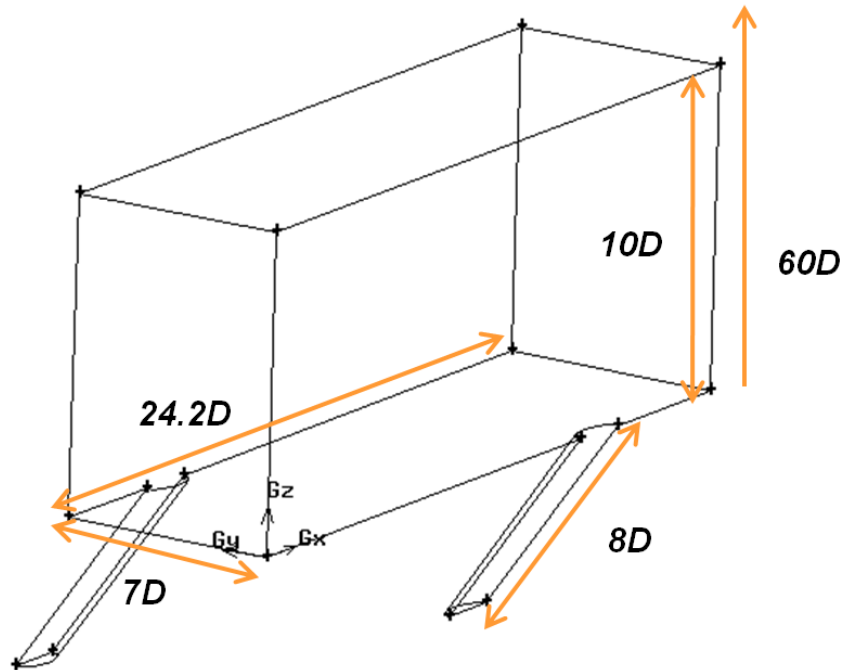|			
α_∞^*	1.0	$\beta_i(outer)$	0.0828
α_∞	0.52	$\sigma_k(inner)$	1.176
β_∞^*	0.09	$\sigma_k(outer)$	1.0
R_β	8.0	$\sigma_\omega(inner)$	2.0
ζ^*	1.5	$\sigma_\omega(outer)$	1.168
M_{t0}	0.25	σ_E	0.85
A_1	0.31	σ_W	0.85
$\beta_i(inner)$	0.075		

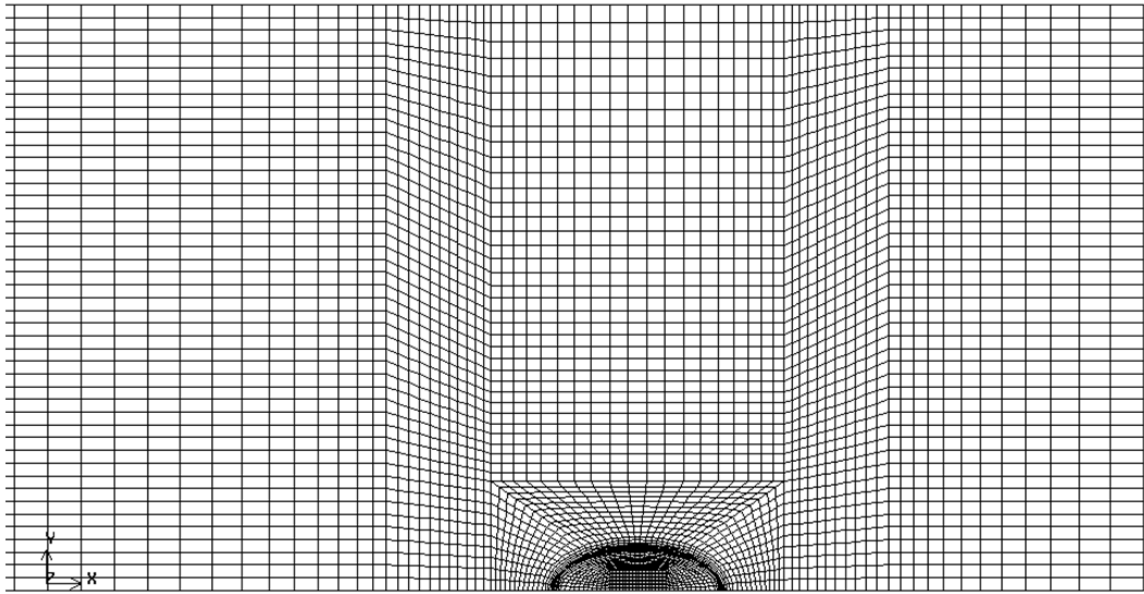Figure 5.1: Domain of numerical predictions.
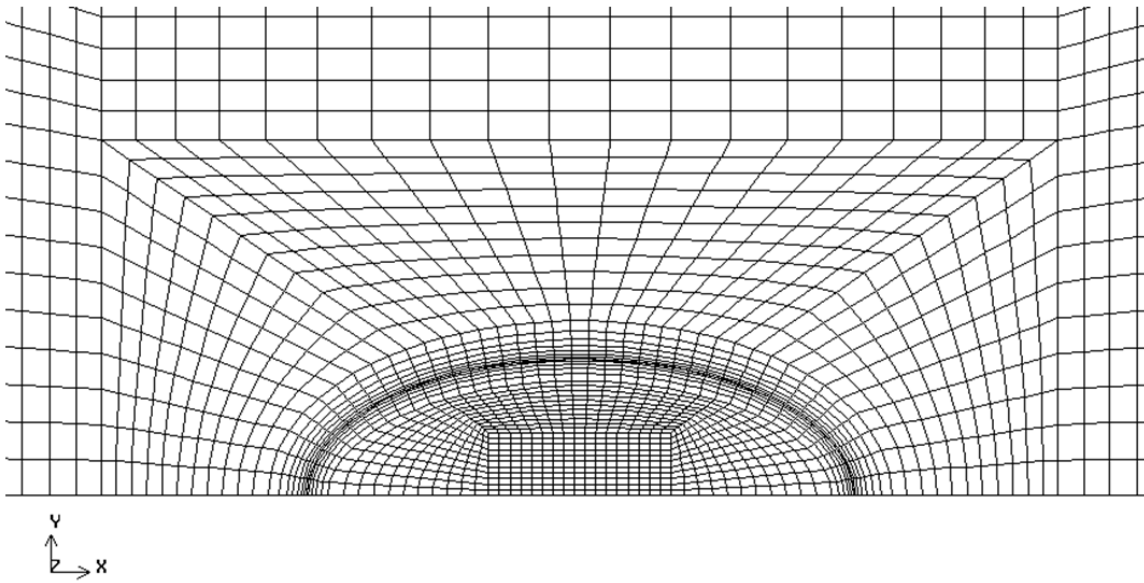
Figure 5.2: View of surface mesh.

Figure 5.3: Zoomed in view of surface mesh, transition from mesh within hole to mainstream
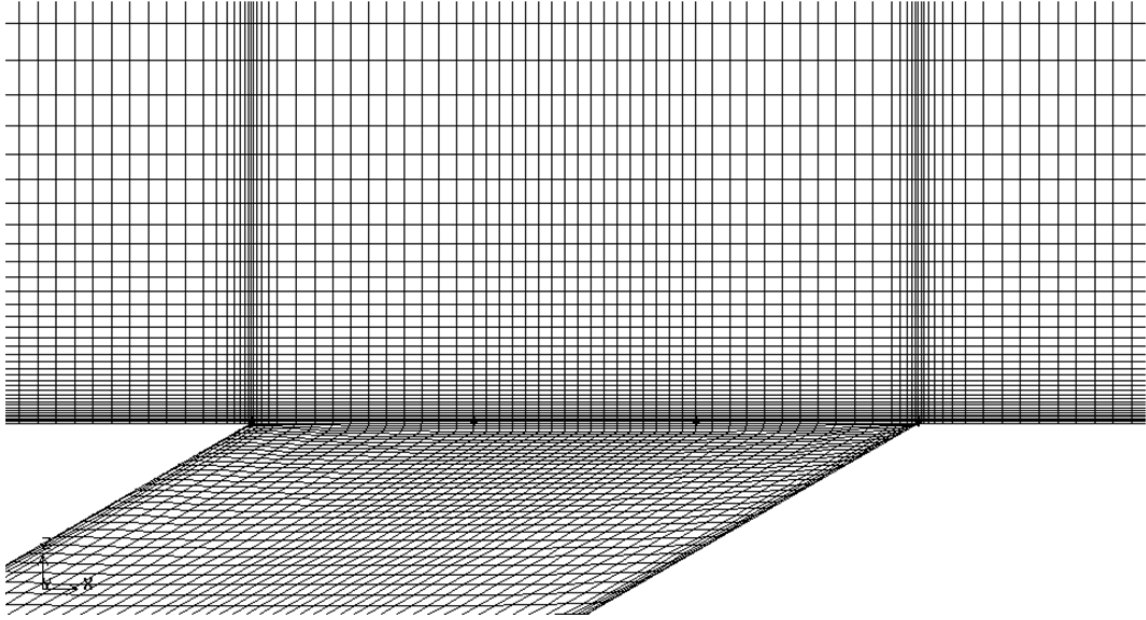
surface.

Figure 5.4: View of symmetry plane mesh, through hole centerline.
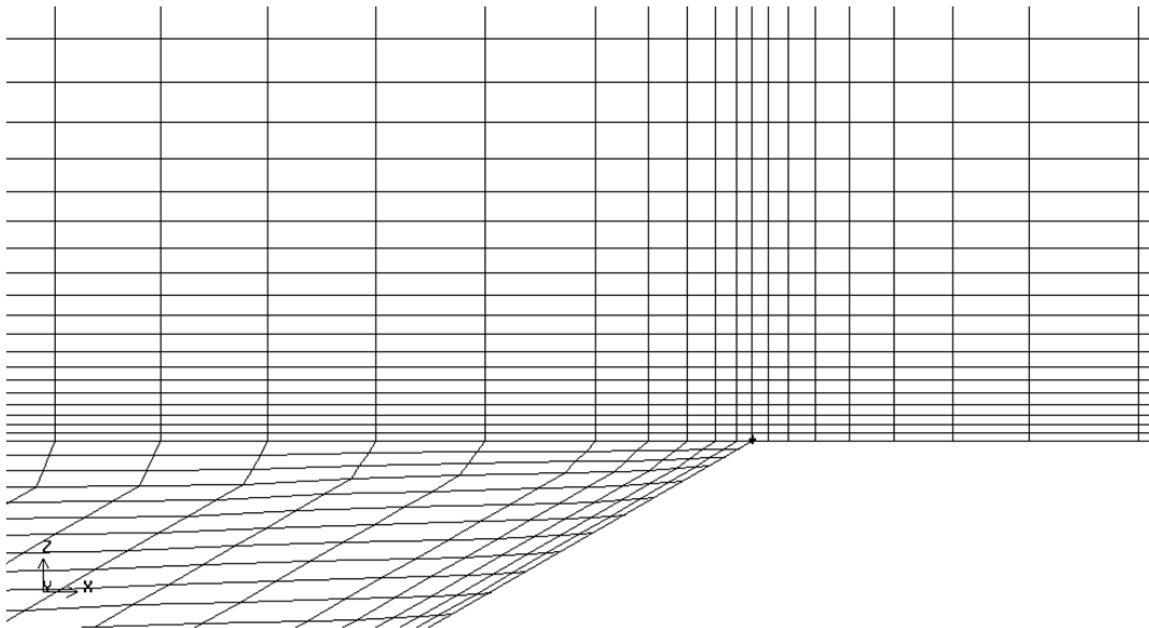

Figure 5.5: Zoomed in view of symmetry plane mesh, highlighting expansion ratios within hole and into mainstream boundary layer.

The left and right faces of the main section are specified with a symmetry boundary. This implies an infinite row of similar holes in both lateral directions. The top face of the main section is also specified as a symmetry plane. This approximation most closely approaches tunnel conditions while still keeping computing power low because the boundary layer on the wall opposite cooling does not need resolution in the boundary layer. The downstream face of the main section is specified with an outflow boundary condition with a weighting of one. This boundary condition states that all of the mass injected into the domain exits from this face. The upstream face of the main section is specified as a velocity inlet. This face is specified with a velocity normal to the surface with the magnitude being determined by a small profile. Outside a specified y distance from the wall which represents boundary layer thickness, in this case $\delta = 10mm$, the velocity is constant, $U_\infty = 26.5m/s$. For a y location less than the boundary layer thickness the velocity fits a $1/7th$ power into the wall. This poor approximation of the viscous sub-layer at the extent of the domain is quickly resolved to a typical turbulent boundary layer slightly downstream. Also applied to this face is a temperature of $T_c = 300K$, turbulence intensity of $TI = 0.7\%$ and integral length scale of $L_I = 3.1cm$. In cases solving downstream rows the boundary conditions are specified in a different manner discussed in the following section. The last remaining boundaries of the domain are the two faces at the film hole inlets. These faces are specified as velocity inlets which are vectored along the hole axis at $\alpha = 30°$. The velocity magnitude is dependent upon blowing ratio case, the temperature is $T_\infty = 350K$, the turbulence intensity is 1% and the hydraulic diameter is set as $2.5mm$.

Table 5.4: Boundary Conditions

Face	Description
Bottom Wall	No slip, adiabatic, impermeable wall
Hole Walls	No slip, adiabatic, impermeable wall
Lateral Walls	Symmetry (no velocity gradient, adiabatic) $\rightarrow$ infinite row
Top Wall	Symmetry (no velocity gradient, adiabatic)
Main Exit	Outflow, weighted 1
Main Inlet	Velocity inlet profile; $1/7^{th}$ profile δ=10mm $U_{\infty} = 26.5m/s, v = w = 0$ TI=0.7% (Constant) $L_I = 3.1cm$ (Constant) $T_{\infty} = 300K$
Hole Inlets	Velocity inlet, components (vectored along hole axis); x-velocity, $u = \frac{M}{DR}U_{\infty}\cos\alpha = Constant$ y-velocity, $v = \frac{M}{DR}U_{\infty}\sin\alpha = Constant$ TI=1% $D_H = 2.5mm \rightarrow L_I = 0.225mm$ $T_C = 350K$

5.2.7 Solution Process

To simplify the solution process and reduce computation/modeling time, an approach is used which only solved one stage, two rows, of the full-coverage array. To predict downstream rows, the solution at the exit of a stage is applied as the inlet boundary condition on stages downstream. In this way a single mesh, of two rows in the stream direction by a half pitch in the span direction, can be used to predict the cooling resulting from any desired number of rows. This is different than a streamwise periodic boundary condition which is not applicable to the current solution due to a mass source in the domain.

Spatial discretization is accomplished with a 2nd order central scheme for the diffusion terms and a 2nd order upstream method for the non-linear advection terms. The SIMPLE algorithm is used for pressure velocity coupling with the pressure-based formulation available in Fluent. Under-relaxation factors are controlled to ensure convergence of the iterative scheme. Convergence is specified at the satisfaction of three criteria: (1) scaled residuals below 10^{-6} for all equations, (2) normalized iterative convergence of three temperature monitors on the surface of interest below 10^{-5}, and (3) normalized global mass and energy flow errors below 10^{-3}.

5.3 Results

Predicted FC effectiveness
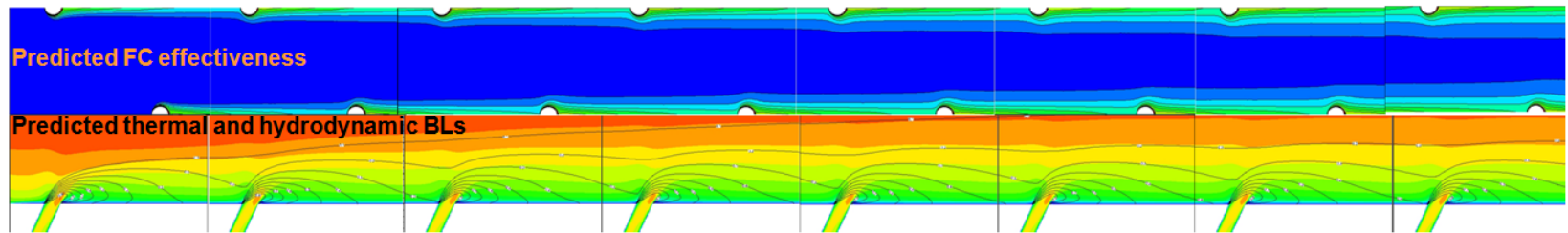
Predicted thermal and hydrodynamic BLs

Figure 5.6: RKE prediction of; Top — adiabatic film cooling effectiveness and Bottom — hydrodynamic BL (color contours) and thermal BL (line contours).
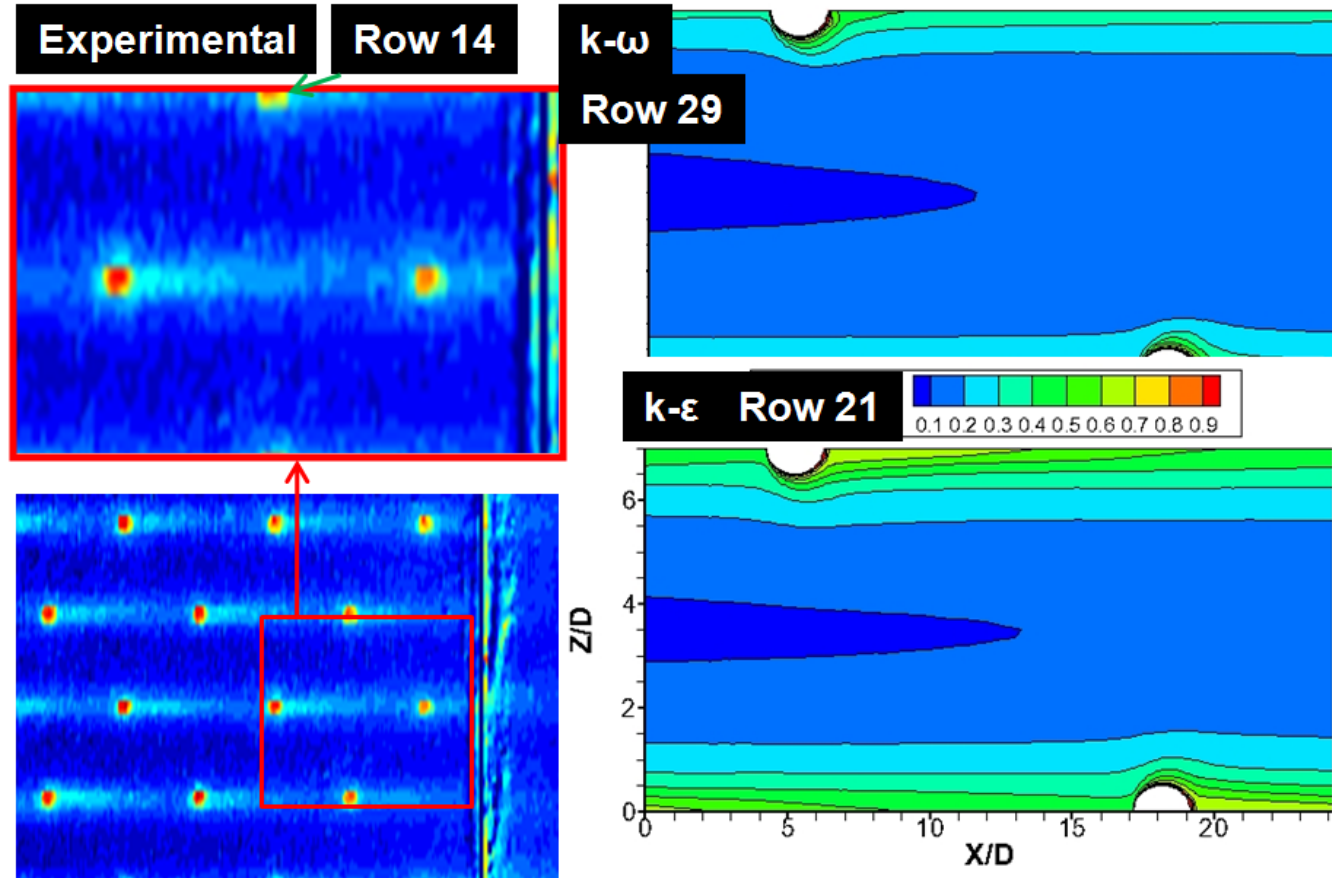
Figure 5.7: Local η contours. Comparison of jet spreading characteristics; experimental results with current predictions.

Laterally averaged film cooling effectiveness as it varies in the flow direction is shown in Figure 5.9 and Figure 5.10. The RKE prediction of FC2 at $M = 0.5$ matches the experimental results well throughout the array however effectiveness in the recovery region is over-predicted as seen in Figure 5.8. The $SSTKW$ models prediction of FC2 at $M = 0.5$ shows effectiveness levels matching experimental at the first two rows however quickly begins to under-predict cooling compared with experimental results seen in Figure 5.9. At high blowing both models under-predict cooling at the beginning of the array. A prediction of essentially zero cooling on the wall results from both models. This is similar to what was seen in [37]. At downstream rows however there is a large increase in effectiveness, predicted by the RKE and $SSTKW$ simulations, which is due to the film ejected into the outer regions of the boundary layer upstream reattaching downstream, shown in Figure 5.10. The RKE prediction shows a more gradual reattachment while the $SSTKW$ shows a sharper, more violent reattachment of the film. This effect is undoubtedly seen in the experimental data in the recovery region as the effectiveness continues to climb even though there is no more injection of coolant.

The effectiveness over the centerline of FC2 blowing at $M = 0.5$ is shown in Figure 5.11. The RKE prediction overshoots effectiveness, as compared to experimental measurements, at the centerline throughout the entire domain. The $SSTKW$ prediction overshoots for the first couple rows then quickly approaches experimental results.
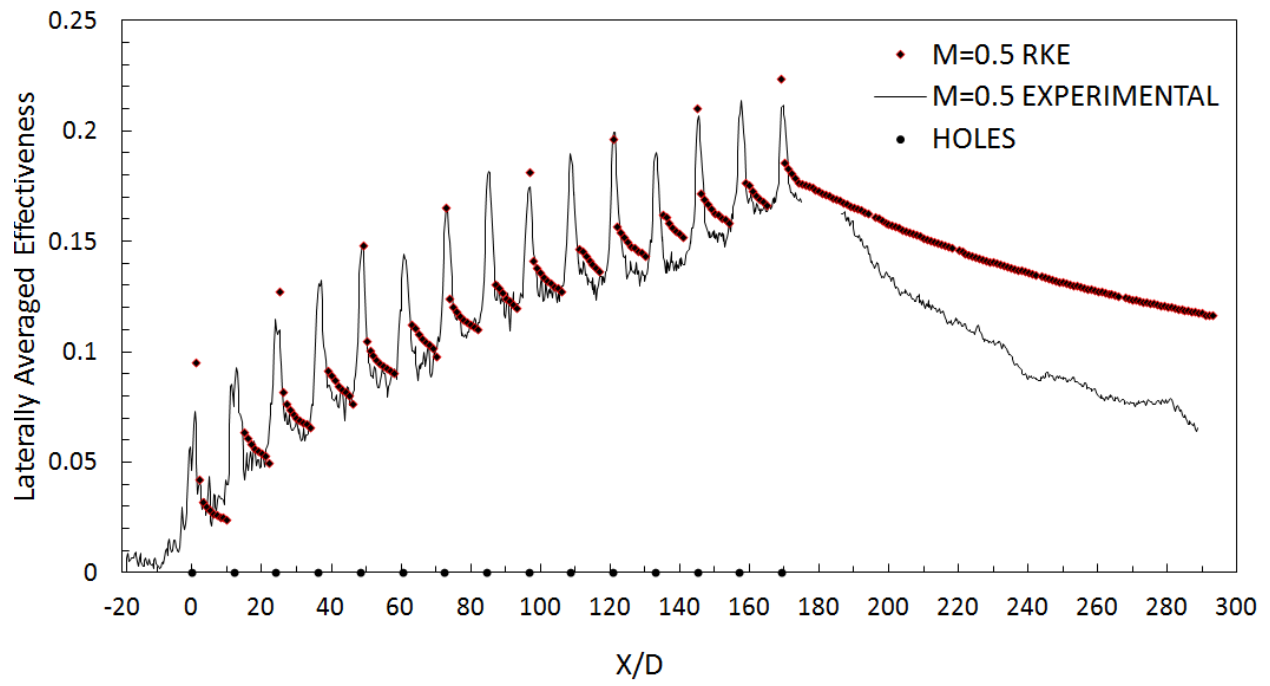
Figure 5.8: Prediction of effectiveness throughout an FC2 geometry compared with TSP measurements of the same scenario.
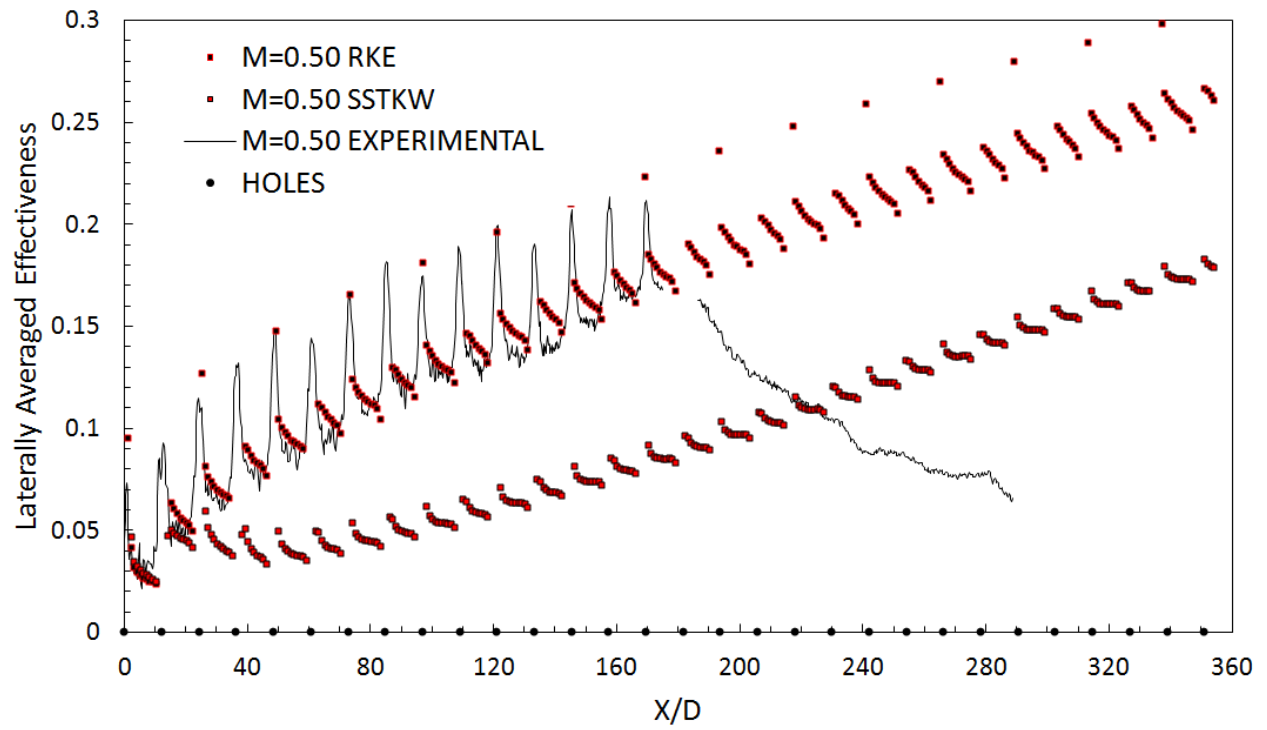
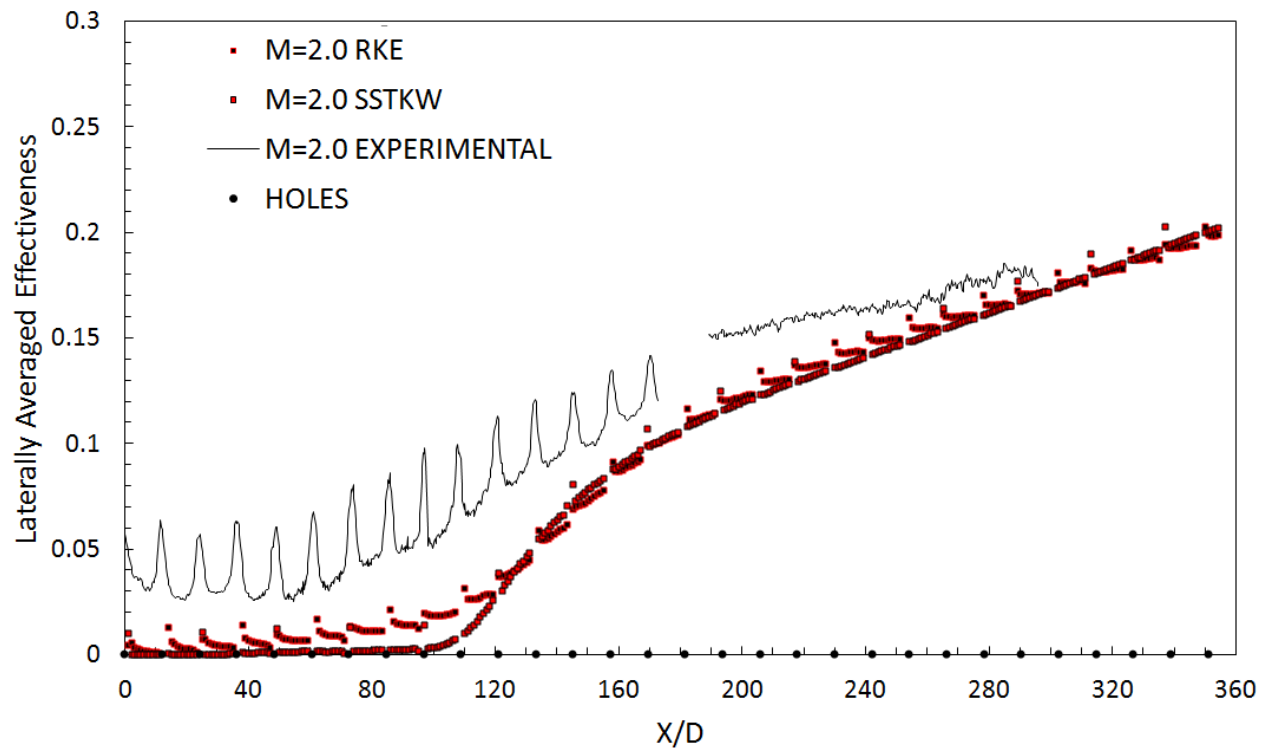Figure 5.9: FC2 M=0.5. 30 rows predicted by $SSTKW$ and RKE with experimental (TSP) 15 rows + RR.

Figure 5.10: FC2 M=2.0. 30 rows predicted by $SSTKW$ and RKE with experimental (TSP) 15 rows + RR.

5.4   Discussion

- At low blowing, the RKE model provides laterally averaged effectiveness profiles matching current experimental results. When scrutinized locally, the effectiveness is distributed non-physically; with effectiveness too high at hole center and too low mid-pitch.

- At high blowing, the RKE model does not capture the near-hole region properly; however, does predict the reattachment of the film in a realistic manner.

- At low bowing, the $SSTKW$ model provides poor prediction of effectiveness throughout the film array, heavily under-predicting effectiveness.

- At high blowing, the $SSTKW$ model predicts a violent, most likely non-physical, reattachment of the film. Also, the $SSTKW$ model used did not predict near-hole behaviour properly and under-predicts effectiveness near injection.

- recommended model from this study for predictions of full-coverage film cooling effectiveness is the $Realizable\ k-\varepsilon$ model as described earlier.

5.5   Suggestion for Future Predictions of Full-Coverage Film Cooling

For this study a strict streamwise period is modeled. It was mentioned during weekly communication with Siemens that this method would be more robust if a dummy section

downstream of the solution domain is modeled in order to properly account for the upstream flow seeing the downstream rows of injection as well as ensuring the outflow boundary condition with a weighting of 1 is not enforcing such a behaviour and prohibiting recirculation. This procedure is recommended for future predictions.
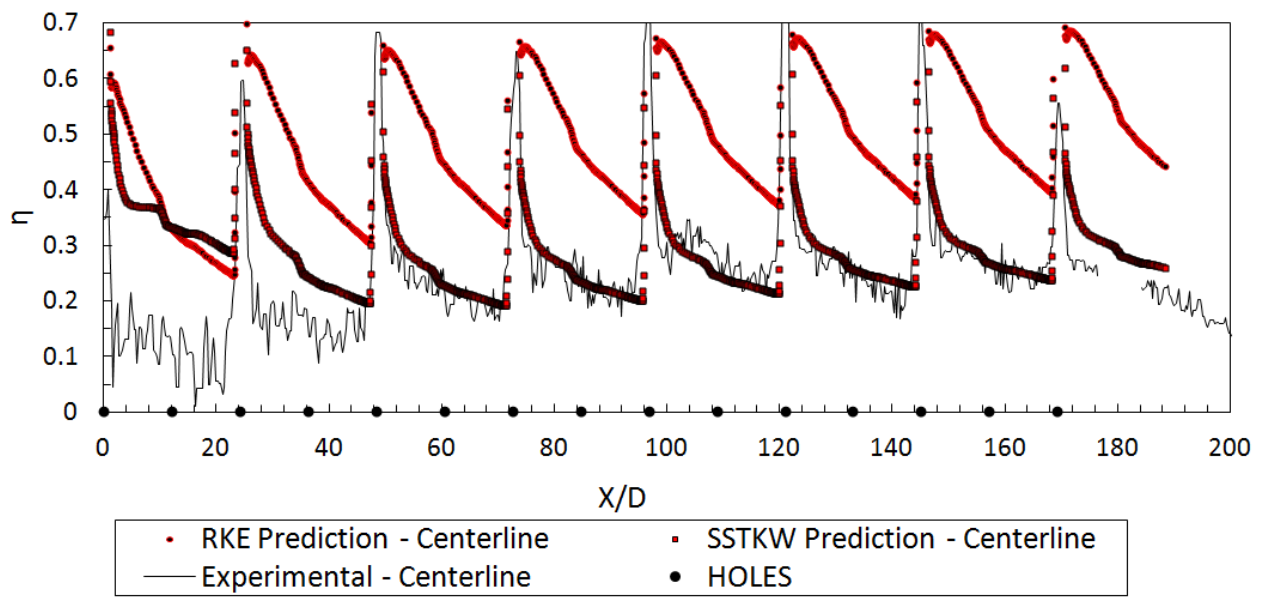
Figure 5.11: FC2, M=0.5, Centerline effectiveness; RKE, $SSTKW$ and TSP.

CHAPTER 6
CONCLUSIONS

6.1   Surface Measurements

6.1.1   Adiabatic Film Cooling Effectiveness

Local adiabatic film cooling effectiveness has been quantified throughout four compound angle, cylindrical hole, multi-row film cooling arrays. The effect of blowing ratio is investigated throughout the four arrays of different hole spacings and inclination angles. It is seen that blowing ratio and hole spacing are of first order effect on adiabatic film cooling effectiveness while the inclination angle is of second order impact.

The physics of the film is unaffected by a change in hole spacing at these, already large, hole-to-hole spacings; meaning coolant is not spent more or less efficiently due to a change in spacing. While the inclination angle has local effects, once laterally averaged over several rows, these effects wash out and are indistinguishable while considering experimental uncertainty.

The recovery region of the film behaves differently for different blowing ratios. In a fully attached film, the recovery region decays exponentially. In a lifted film, the decay has a concave down profile, indicating competing effects of dissipation and reattachment.

This is characteristic of the entire array, not just the recovery region. Overall, compound angle arrays are capable of providing significant levels of laterally averaged effectiveness after several rows, even at the large spacing of $P/D = X/D = 19.8$.

Contrary to previous reports, e.g Kasagi et al. [23] and Metzger et al. [16], the film cooling effectiveness is seen to increase with increasing blowing ratio and no optimum in the range studied is found. This is likely do to the extent (20-30 rows) of the array. In the first section of the array (comparable to the previous studies' entire array) the high blowing cases indeed provide less cooling than the lower blowing cases. However, by the end of the current studies array, these lifted jets return to the surface and provide greater cooling levels than the low blowing cases.

6.1.2   Heat Transfer Augmentation

Heat transfer augmentation has been quantified for four different full-coverage film cooling arrays. The effect of blowing ratio, M, on the arrays is seen to be a second-order effect on the enhancement factors, h/h_0. The hole spacing is also a second-order effect while at these large spacings. While the inclination angle has local effects, once laterally averaged over several rows, these effects wash out and are indistinguishable while considering experimental uncertainty.

All the arrays enhancement factors are seen to level off to within uncertainty after five or six rows implying the fact that once certain number of rows are used, additional rows

will not suffer from higher heat transfer augmentation values than previous ones. Overall, the higher spacing produced the lowest heat transfer augmentation factors while providing significant amount of coolant coverage throughout the surface. The effect of inclination angle is minimal at the large array spacing.

The experimental uncertainty must be driven down to resolve these small differences. If the range of hole spacings and hole orientations were larger, a difference would be clear.

6.1.3 Suggestion for Future Work

The surface data can only provide a small glimpse into the physics throughout this full-coverage array. To confirm the mechanism behind the surface data, flow measurements throughout these very large spaced geometries is of interest. Specifically in the recovery region to confirm the reason for the seemingly very different dynamics as blowing ratio is varied.

6.2 Predictions

- At low blowing, the RKE model provides laterally averaged effectiveness profiles matching current experimental results. When scrutinized locally, the effectiveness is distributed non-physically; with effectiveness too high at hole center and too low mid-pitch.

122

- At high blowing, the RKE model does not capture the near-hole region properly; however, does predict the reattachment of the film in a realistic manner.

- At low bowing, the $SSTKW$ model provides poor prediction of effectiveness throughout the film array, heavily under-predicting effectiveness.

- At high blowing, the $SSTKW$ model predicts a violent, most likely non-physical, reattachment of the film. Also, the $SSTKW$ model used did not predict near-hole behaviour properly and under-predicts effectiveness near injection.

- The recommended model from this study for predictions of full-coverage film cooling effectiveness is the $Realizable\ k - \varepsilon$ model as described earlier.

6.2.1 Suggestion for Future Predictions of Full-Coverage Film Cooling

For this study a strict streamwise period is modeled. This method would be more robust if a dummy section downstream of the solution domain is modeled in order to properly account for the upstream flow seeing the downstream rows of injection as well as ensuring the outflow boundary condition with a weighting of one is not enforcing such a behaviour and prohibiting recirculation. This procedure is recommended for future predictions.

LIST OF REFERENCES

[1] U. S. EIA, "International energy outlook," tech. rep., U. S. EIA, 2010.

[2] J. Polezhaev, "The transpiration cooling for blades of high temperature gas turbine," *Energy Convers. Mgmt.*, 1997.

[3] R. S. Bunker, "Cooling design analysis," in *DOE Gas Turbine Handbook*.

[4] R. J. Goldstein, "Film cooling," *Advances in Heat Transfer*, 1971.

[5] R. J. Goldstein, G. Shavit, and T. S. Chen, "Film-cooling effectiveness with injection through a porous section," *Journal of Heat Transfer*, 1965.

[6] J. Hartnett, R. Birkebak, and E. Eckert, "Velocity distributions, temperature distributions, effectiveness and heat transfer for air injected through a tangential slot into a turbulent boundary layer," *Journal of Heat Transfer*, 1961.

[7] D. R. Pedersen, E. R. G. Eckert, and R. J. Goldstein, "Film cooling with large density differences between the mainstream and the secondary fluid measured by the heat-mass transfer analogy," *Journal of Heat Transfer*, 1977.

[8] A. K. Sinha, D. G. Bogard, and M. E. Crawford, "Film-cooling effectiveness downstream of a single row of holes with variable density ratio," *Journal of Turbomachinery*, 1991.

[9] V. Aga, *Experimental Flow Sctructure Investigation of Compound Angled Film Cooling*. PhD thesis, ETH Zurich, 2009.

[10] R. J. Goldstein, E. R. G. Eckert, V. L. Eriksen, and J. W. Ramsey, "Film cooling following injection through inclined circular tubes," tech. rep., NASA, 1969.

[11] S. Baldauf, M. Scheurlen, A. Schulz, and S. Wittig, "Correlation of film-cooling effectiveness from thermographic measurements at enginelike conditions," *Journal of Turbomachinery*, 2002.

[12] S. Baldauf, M. Scheurlen, A. Schulz, and S. Wittig, "Heat flux reduction from film cooling and correlation of heat transfer coefficients from thermographic measurements at enginelike conditions," *Journal of Turbomachinery*, 2002.

[13] S. S. Papell, "Effect on gaseous film cooling of coolant injection through angled slots and normal holes," tech. rep., NASA, 1960.

[14] D. E. Metzger, D. I. Takeuchi, and P. A. Kuenstler, "Effectiveness and heat transfer with full-coverage film cooling," *Journal of Engineering for Power*, 1973.

[15] M. E. Mayle and F. J. Camarata, "Multihole cooling film effectiveness and heat transfer," *ASME Journal of Heat Transfer*, 1975.

[16] D. E. Metzger, P. A. Kuenstler, and D. I. Takeuchi, "Heat transfer with film cooling within and downstream of one to four rows of normal injection holes," in *ASME Turbo Expo*.

[17] E. Le Grives, J. J. Nicolas, and J. Genot, "Internal aerodynamics and heat transfer problems associated to film cooling of gas turbines," in *ASME Turbo Expo*.

[18] M. Sasaki, K. Takahara, T. Kumagai, and M. Hamano, "Film cooling effectiveness for injection from multirow holes," *Journal of Engineering for Power*, 1979.

[19] S. Yavuzkurt, R. J. Moffat, and W. M. Kays, "Full-coverage film cooling part 1. three-dimensional measurements of turbulence structure," *Journal of Fluid Mechanics*, 1980.

[20] S. Yavuzkurt, R. J. Moffat, and W. M. Kays, "Full-coverage film cooling part 2. prediction of the recovery-region hydrodynamics," *Journal of Fluid Mechanics*, 1980.

[21] M. E. Crawford, W. M. Kays, and R. J. Moffat, "Full-coverage film cooling part i: Comparison of heat transfer data for three injection angles," *Journal of Engineering for Power*, 1980.

[22] M. E. Crawford, W. M. Kays, and R. J. Moffat, "Full-coverage film cooling part ii: Heat transfer data and numerical simulation," *Journal of Engineering for Power*, 1980.

[23] N. Kasagi, M. Hirata, and M. Kumada, "Studies of full-coverage film cooling part1: Cooling effectiveness of thermally conductive wall," in *ASME Turbo Expo*.

[24] H. H. Cho and R. J. Goldstein, "Heat (mass) transfer and film cooling effectiveness with injection through discrete holes: Partii – on the eexposed surface," *Journal of Turbomachinery*, 1995.

[25] M. Martiny, A. Schulz, and S. Wittig, "Full-coverage film cooling investigation: Adiabatic wall temperatures and flow visualization," in *ASME*.

[26] H. H. Cho and R. J. Goldstein, "Total coverage discrete hole wall cooling," *Journal of Turbomachinery*, 1997.

[27] M. K. Harrington, M. A. McWaters, D. G. Bogard, C. A. Lemmon, and K. A. Thole, "Full-coverage film cooling with short normal injection holes," in *ASME Turbo Expo*.

[28] J. P. Ling, P. T. Ireland, and L. Turner, "Full coverage film cooling for combustor transition sections," in *ASME Turbo Expo*.

[29] G. B. Kelly and D. G. Bogard, "An investigation of the heat transfer for full coverage film cooling," in *ASME Turbo Expo*.

[30] B. Michel, P. Gajan, A. Strzlecki, B. Wagner, N. Savary, and A. e. a. Kourta, "Full coverage film cooling using compound angle," *C. R. Mecanique*, 2009.

[31] J. P. Sellers, "Gaseous film cooling with multiple injection stations," *AIAA Journal*, 1963.

[32] M. E. Crawford, W. M. Kays, and R. J. Moffat, "Heat transfer to a full-coverage film-cooled surface with 30degree slant-hole injection," tech. rep., NASA, 1976.

[33] J. Guo, P. Y. Julienn, and R. N. Meroney, "A modified log-wake law for zero-pressure-gradient turbulent boundary layers," *Journal of Hydraulic Research*, 2005.

[34] Q. Liu, *Study of Heat Transfer Characteristics of Impinging Air Jet Using Pressure and Temperature Sensitive Luminescent Pain.* PhD thesis, University of Central Florida, 2006.

[35] C. Y. Ho and T. K. Chu, "Electrical resistivity and thermal conductivity of nine selected aisi stainless steels," tech. rep., CINDAS, 1977.

[36] *ANSYS Fluent 12.0 Theory Guide.*

[37] L. El-Gabry, J. Heidmann, and A. Ameri, "Numerical analysis of film cooling at high blowing ratio," tech. rep., NASA, 2009.

[38] *Gambit User's Guide.*